

Syntheses and Characterization of Single Crystal Metal-Organic Frameworks for Optical Applications

Von der Naturwissenschaftlichen Fakultät der
Gottfried Wilhelm Leibniz Universität Hannover

zur Erlangung des Grades
Doktorin der Naturwissenschaften
(Dr. rer. nat.)

genehmigte Dissertation von
Anna-Lena Erika Renate Deutsch, M. Sc.

2023

Referent: Prof. Dr. rer. nat. Denis Gebauer

Korreferent: Prof. Dr. rer. nat. Dr. rer. nat. habil. Reinhard X. Fischer

Tag der Promotion: 22.11.2023

Abstract

This dissertation deals with the syntheses, optical characterization and optical application of metal-organic frameworks (MOFs).

In the first part of this thesis, different MOF single crystals were synthesized. Different structures were investigated in which either the metal cations or the organic linker molecules were varied. The organic linker molecules were also modified by post-synthetic variation. In order to obtain precise refractive indices of these MOF single crystals, the immersion method was used. To the best of our knowledge, this method has not yet been used in the characterization of MOFs. Consequently, besides the measurements itself, the investigation of the suitability of the method was also part of the work.

The second part of this thesis deals with the syntheses of $\text{Ce(IV)}bdc\text{-CsPbBr}_3\text{-SiO}_2$ materials for use in light-emitting devices (LEDs). For this purpose, different synthesis routes were investigated and the materials obtained were subsequently tested for their stability and performance. For stability testing, the materials were processed into films and exposed to high-intensity illumination as well as elevated temperature and humidity. The aim is to increase the stability of perovskite while still maintaining their highly luminescent performance by embedding them into a MOF-material.

Keywords: Metal-organic frameworks, anisotropy, refractive index, immersion method, single crystals, LED materials

Kurzzusammenfassung

In dieser Dissertation wird die Synthese, optische Charakterisierung und optische Anwendung von metal-organischen Gerüstverbindungen (engl.: metal-organic frameworks, MOFs) behandelt.

Im ersten Teil dieser Arbeit wurden verschiedene MOF Einkristalle synthetisiert. Hierbei wurden unterschiedliche Strukturen untersucht, bei deren Zusammensetzungen entweder die Metallkationen oder organischen Linkermoleküle variiert wurden. Die organischen Linkermoleküle wurden hierzu auch mittels post-synthetischer Variation verändert. Um exakte Brechungsindizes ebendieser MOF Einkristalle erhalten zu können, wurde die Immersionsmethode verwendet. Diese Methode fand unseres Wissens nach bisher keine Verwendung in der Charakterisierung von MOFs. Folglich war neben der reinen Messung auch die Untersuchung hinsichtlich der Eignung der Methode Bestandteil der Arbeit.

Der zweite Teil dieser Arbeit befasst sich mit der Synthese von Ce(IV)*bdc*-CsPbBr₃-SiO₂ Materialien für die Verwendung in LEDs (engl.: light-emitting devices). Dazu wurden verschiedene Synthesewege untersucht und die erhaltenen Materialien anschließend auf ihre Stabilität und Leistung getestet. Zur Stabilitätsuntersuchung wurden die Materialien zu Filmen verarbeitet und hoher Beleuchtungsintensität, sowie erhöhter Temperatur und Feuchtigkeit ausgesetzt. Ziel ist es, die Stabilität der Perowskite zu erhöhen und gleichzeitig ihre hohe Leuchtkraft zu erhalten, indem sie in ein MOF-Material eingebettet werden.

Stichwörter: Metall-Organische Gerüstverbindungen, anisotroper Brechungsindex, Immersionsmethode, Einkristalle, LED Materialien

Danksagung/Acknowledgement

Als erstes möchte ich mich ganz herzlich bei Herrn Prof. Dr. Behrens bedanken, dass ich die Möglichkeit bekommen habe, diese Arbeit in seinem Arbeitskreis anfertigen zu dürfen. Außerdem für die Ermöglichung eines mehrmonatigen Forschungsaufenthaltes in Südkorea. Sein Tod war ein schwerer Schlag und mein herzlichstes Beileid gilt seiner Familie und allen, die Ihm nahe standen.

Ebenfalls möchte ich mich bei Herrn Prof. Dr. Fischer von der Universität Bremen für die höchst interessante Kooperation bedanken und bei Herrn Prof. Dr. Denis Gebauer für die Übernahme des Erstprüfers.

Bedanken möchte ich mich auch bei meinen Mentoren und Betreuern Herrn Dr. Schaate und Herrn Dr. Birkenstock für die vielen produktiven, wissenschaftlichen Diskussionen.

Des Weiteren gilt mein Dank den gesamten Arbeitskreisen Behrens und Fischer für die freundliche Atmosphäre während meiner Zeit dort.

Ebenso möchte ich mich bei Karen Hindricks für die überaus nette Zeit im gemeinsamen Labor bedanken. Des Weiteren danke ich Monika Seegers und Inga Wille für die schöne Zeit der gemeinsamen Praktikumsbetreuung und die spannenden Thermitzündungen. Bedanken möchte ich mich auch bei meinen Bacheloranden, insbesondere bei Oliver Stölting.

Danken möchte ich auch der ACI Skat-Runde für die überaus lustigen Abende, sowie der Tennis-Runde für die schönen Tennisspiele!

Von ganzem Herzen möchte ich mich auch bei meiner Familie und ganz besonders bei meinen Eltern Horst und Dorit bedanken. Ohne euch hätte ich das nicht geschafft.

Ebenfalls möchte ich mich bei Mosaieb und Sophie für die netten Sushi-Abende nach Laborschluss bedanken. Danken möchte ich auch meinen Freundinnen Yvonne, Naddel und Britta, für die jahrelange Freundschaft und Unterstützung. Zudem bedanke ich mich bei Ariane für die vielen

aufmunternden Worte und Ratschläge, auch über Ländergrenzen hinweg.

Furthermore, I would like to thank Prof. Dr. Lee from the Seoul National University for providing the chance to research under his supervision.

Also, I am very grateful to my mentor Dr. Kim for his helpful and friendly supervision and everything he has taught me.

Thank you, to all PNEL members for the warm welcome and the nice atmosphere during my stay in South Korea. I also want to thank Dong Jie, I could not have wished for a kinder person sitting next to me in the office.

A special thanks also to Jiang Jixin and (again) Dong Jie for exploring the sights and food of South Korea together with me, as well as all for all the times we enjoyed delicious hotpot.

List of Abbreviations

0D	zero-dimensional
1D	one-dimensional
2D	two-dimensional
3D	three-dimensional
Å	Ångström, 10^{-10} m
α	refractive index
a. u.	arbitrary units
BET	Brunauer-Emmett-Teller
BNaph	1-bromonaphthalene
°C	centigrade
ca.	around (lat.: circa)
CAU	Christian-Albrecht University
CTAB	Cetyltrimethylammonium bromide
γ -CD	γ -cyclodextrin
d	day(s)
DEF	N,N-diethylformamide
DIM	diiodomethane
DMF	N,N-dimethylformamide
DMSO	dimethyl sulfoxide
<i>eq</i>	Equivalent(s)
<i>et al.</i>	and others (lat.: et alii)
EDXS	energy dispersive X-ray spectroscopy
etc.	and others (lat.: et cetera)
e.g.	for example (lat.: exempli gratia)
EtOH	ethanol
°	degree
g	gram(s)
h	hour(s)
H ₂ bdc	terephthalic acid
H ₂ bdc(OH) ₂	2,5-dihydroxyterephthalic acid
H ₂ bdc-NO ₂	2-nitroterephthalic acid
HbIm	benzimidazole

HnIm	2-nitroimidazole
H ₂ bzpdC	benzophenone-4,4'-dicarboxylic acid
H ₂ pydc	2,6-pyridinedicarboxylic acid
HOT	Hannover Centre for Optical Technologies
HKUST	Hong Kong University of Science and Technology
HydroT	hydrogenated terphenyl
<i>I</i>	Intensity
IBU	Inorganic building unit
IR	infrared
λ	wavelength
K	kelvin
<i>m</i> %	mass percent
mg	milligram(s)
min	minute(s)
mL	millilitre(s)
μ L	microliter(s), 10 ⁻⁶ L
μ m	micrometre(s), 10 ⁻⁶ m
mmol	millimole
MIL	materials of the Lavoisier institute (fr.: Matériaux de l'Institut Lavoisier)
MOF	metal-organic framework
mol	mole
MSE	mean squared error
<i>n</i>	refractive index
n/a	not available
nm	nanometre(s), 10 ⁻⁹ m
NMR	nuclear magnetic resonance
%	percent
<i>p</i>	pressure
PCP	porous coordination polymers
PLQY	photoluminescence quantum yield
PSM	post-synthetic modification
R _A	refraction (atomic)
RI	refractive index

rpm	rounds per minute
s	second(s)
SEM	Scanning electron microscopy
θ	angle of incidence/reflection
T	temperature, transmission
t	time
TEM	transmission electron microscopy
TMB	1,3,5-trimethyl benzene
TMOS	tetramethyl orthosilicate
UiO	university of Oslo (Universitetet i Oslo)
UTSA	university of Texas at San Antonio
V	volume
x	mass concentration
XRD	X-ray diffraction
ZIF	zeolitic imidazolate framework
ZJU	Zhejiang University

Table of Content

Abstract.....	I
Kurzzusammenfassung.....	II
Danksagung/Acknowledgment.....	III
List of Abbreviations.....	V
Table of Content.....	IX
1 Introduction	1
2 Current state of research	4
2.1 Metal-organic frameworks (MOFs)	4
2.2 MOFs and their refractive indices.....	6
2.2.1 The refractive index.....	6
2.2.2 Refractive index variation within MOFs.....	7
2.2.3 Refractive index increment systems.....	9
2.2.4 Immersion method.....	11
2.3 MOF single crystals: Syntheses and structures	13
2.3.1 Al- <i>pydc</i>	18
2.3.2 Cd- and Zn- <i>bzpd</i> c.....	18
2.3.3 Hf- and Zr- <i>bzpd</i> c.....	19
2.3.4 UiO-66 and UiO-66-NO ₂	20
2.3.5 UTSA-74.....	21
2.3.6 γ -CD MOFs (Cs, K, Li, Rb).....	21
2.3.7 Na- γ -CD MOF.....	22
2.3.8 ZIF-7.....	23
2.3.9 ZIF-8 and ZIF-90.....	23
2.3.10 ZIF-68 to ZIF-70, ZIF-78, ZIF-81 and ZIF-82	24
2.4 Perovskites.....	25
2.5 Perovskite-MOF materials.....	26
3 Objectives.....	30
4 Experimental Section.....	31
4.1 Analytical Methods.....	31
4.1.1 Powder X-Ray Diffraction.....	31
4.1.2 Light-Optical Microscopy.....	32
4.1.3 Physisorption.....	32
4.1.4 Nuclear Magnetic Resonance Spectroscopy.....	32
4.1.5 Immersion method.....	33
4.1.6 Ellipsometry.....	34

4.1.7	Scanning electron microscopy	34
4.1.8	Transmission electron microscopy.....	35
4.1.9	Photoluminescence spectroscopy	35
4.1.10	60-90 stability testing	35
4.1.11	High flux testing.....	35
4.2	MOF single crystals syntheses	36
4.2.1	Al- <i>pydc</i>	37
4.2.2	Cd- <i>bzpd</i>	37
4.2.3	Zn- <i>bzpd</i>	37
4.2.4	Hf- <i>bzpd</i>	37
4.2.5	Zr- <i>bzpd</i>	38
4.2.6	Zr- <i>bzpd</i> with post-synthetic modifications.....	38
4.2.7	UiO-66	39
4.2.8	UiO-66-NO ₂	39
4.2.9	UTSA-74.....	39
4.2.10	Cs- γ -CD MOF.....	40
4.2.11	K- γ -CD MOF	40
4.2.12	Li- γ -CD MOF	41
4.2.13	Rb- γ -CD MOF.....	41
4.2.14	Na- γ -CD MOF.....	41
4.2.15	ZIF-7.....	41
4.2.16	ZIF-8.....	42
4.2.17	ZIF-68.....	42
4.2.18	ZIF-69.....	42
4.2.19	ZIF-70.....	42
4.2.20	ZIF-78.....	43
4.2.21	ZIF-81.....	43
4.2.22	ZIF-82.....	43
4.2.23	ZIF-90.....	43
4.3	Perovskite-Ce-MOF materials	44
4.3.1	Ce-MOF syntheses	44
4.3.2	Perovskite confinement after Ren et al. ^[29]	44
4.3.3	Perovskite confinement after Wu et al. ^[181]	45
4.3.4	Perovskite-Ce-MOF with SiO ₂ -shell synthesis	45
4.3.5	Film fabrication	45
5	Results and Discussion	46
5.1	MOF single crystals.....	46

5.1.1	Successful single crystal syntheses based on literature.....	46
5.1.2	Unusual shaped single crystals.....	51
5.1.3	Modified literature syntheses routes.....	53
5.1.4	Zr- <i>bzpd</i> c with post-synthetic modifications.....	55
5.2	Refractive index measurements of MOF single crystals.....	56
5.2.1	<i>bzpd</i> c-MOF single crystals.....	56
5.2.2	γ -CD MOF.....	57
5.2.3	ZIF single crystals.....	58
5.2.4	Other single crystals.....	59
5.2.5	Zr- <i>bzpd</i> c-MOF PSM single crystals.....	59
5.3	NMR investigations of MOF single crystals.....	63
5.3.1	<i>bzpd</i> c-MOF single crystals.....	63
5.3.2	γ -CD MOF.....	64
5.3.3	ZIF single crystals.....	64
5.3.4	Other single crystals.....	65
5.4	Perovskite-MOF materials.....	66
5.4.1	Cerium MOFs.....	66
5.4.2	MOF-Perovskite-SiO ₂ synthesized after Ren et al.....	67
5.4.3	MOF-Perovskite-SiO ₂ syntheses after Wu et al.....	69
5.5	Characterization of Perovskite-MOF materials.....	70
5.5.1	High flux testing.....	70
5.5.2	60-90 testing.....	74
6	Conclusion and Outlook.....	77
7	References.....	81
8	Appendix.....	91
8.1	Powder X-ray diffraction spectra.....	92
8.2	Scanning electron microscopy images.....	92
8.3	¹ H-NMR measurements.....	93
8.4	Ellipsometry Measurements ^[185]	98
9	Curriculum Vitae.....	100
10	List of Publications.....	101

1 Introduction

Due to the increasing demand towards advanced and multifunctional optical technologies, materials that can fulfil these requirements are highly looked after. Apart from challenges regarding, e.g., industrial usage or environmental friendliness of the material, the way to identify and properly characterize potential structures is a challenge within itself.

A highly sought-after material to potentially fulfil this demand are metal-organic frameworks (short: MOFs). They are a special class within porous coordination polymers. MOFs consist of metal ions that are connected via linker molecules. MOFs offer a variety of one- to three-dimensional structures with high porosities and accordingly high inner surface areas. Their main advantage compared to other material classes lies within their wide customizability as well as in their amenability.^[1,2] Regarding the small pore size distribution accompanied by the nearly infinite amount of possible structures and compositions, MOFs have been studied for a variety of applications. Possible application fields are catalysis^[3,4], sensing^[5-8], gas storage and separation^[3,9-11], petrochemistry^[12,13], drug-delivery^[14,15] and more.^[16] There are already first commercial trials established.^[17] The new, optical application fields of MOFs include optical fibres for sensory applications,^[18,19] electrode materials^[20] and electrochemical sensor materials.^[21] In particular, the refractive index (short: RI) plays a key role in relation to modern technologies. In waveguides, for example, the change in the RI of the porous MOFs used is exploited by the adsorption of the substance to be detected.^[18] The RI is usually determined by ellipsometry on optical thin films.

The main challenge concerning ellipsometry is that the results of MOF optical thin films seem to be highly dependent on the film synthesis. As displayed in Figure 1 the RI of the same material varies depending on how the film was synthesized. An UiO-66 optical thin film synthesized by the layer-by-layer approach exhibits a RI that is around 0.4 higher, than an UiO-66 film synthesized via dip-coating. Therefore, huge deviations of the measured RIs for one and the same MOF are reported. This indicates a need to find a more

reliable measurement technique for RIs of MOFs. In this work the immersion method is investigated in order to determine precise, anisotropic RIs.^[22]

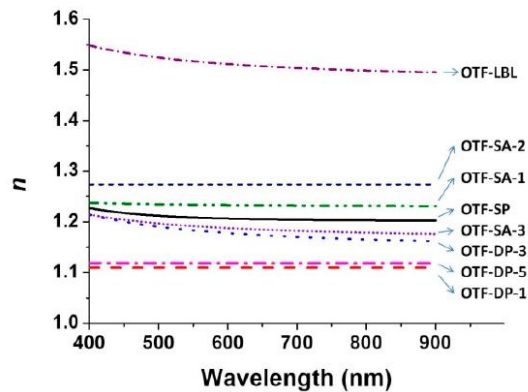


Figure 1: Efficient refractive index of MOF optical thin films (OTFs) (LBL = layer-by-layer; SA = self-assembly; SP = spin-coating; DP = dip-coating)^[22].

The immersion method enables the determination of precise and even more importantly anisotropic RIs. It is very well known within the field of mineralogy^[23] and has not been investigated as an applicable measurement technique for MOFs, yet. The immersion method allows the user to rotate any plane of the crystal into the microscope stage plane. This means, that each of the up to three, anisotropic RIs can be measured using only one single crystal.^[24] The aim of this work is to crystallise various MOFs in order to determine the RIs of these materials. As a result, single crystals that are as defect-free as possible and with a crystal size of at least 200 μm are required. Their syntheses are a challenge within itself since most synthetic strategies aim towards nano-sized MOFs. In contrast, the field of large single crystals (sizes above 30 μm) is rather unexplored.^[25]

As already mentioned, the role of optical applications for MOF materials drastically increased over the last decade. Thus, the optical application of MOFs is part of this work, too. In order to find new and suitable optical materials, for light-emitting devices, MOF-perovskite materials are investigated. Since perovskites are sensitive to light, oxygen and heat exposure, their stability still is one of the main challenges regarding their industrial application as light-emitting diodes.^[26,27]

To prolong the lifetime of perovskites, the porous framework structure of MOF materials offers great stabilizing properties. By the confinement of perovskite nanocrystals within a MOF structure, their ambient storage, thermal- and photostability increase.^[28,29] Until this day, the search for a sufficient way to stabilize perovskites while still maintaining good light emitting properties continues.

2 Current state of research

This chapter focusses on metal-organic frameworks. Especially their refractive indices and its precise determination using the immersion method, as well as their combination with perovskites for application in light-emitting devices are described more in detail.

2.1 Metal-organic frameworks (MOFs)

Metal-organic frameworks (MOFs) are crystalline and porous solids which form a subcategory within the class of porous coordination polymers (PCPs). In general, MOFs consists of metal ions that are connected via linker molecules (Figure 2). Metal ions or metal oxo clusters are, with regard to their coordination by oxygen or nitrogen atoms, also referred to as so-called inorganic building units (IBUs). MOFs were first discovered by Yaghi et al. in 1995 and can range from one-dimensional (1D) to three-dimensional (3D) structures.^[30] The latter generally provide high porosity, large inner surface areas and tuneable pore sizes. Additionally, this class of material offers the unique ability to specifically tailor a MOF structure for a certain desired application due to their enormous range of structure possibilities.^[1,2]

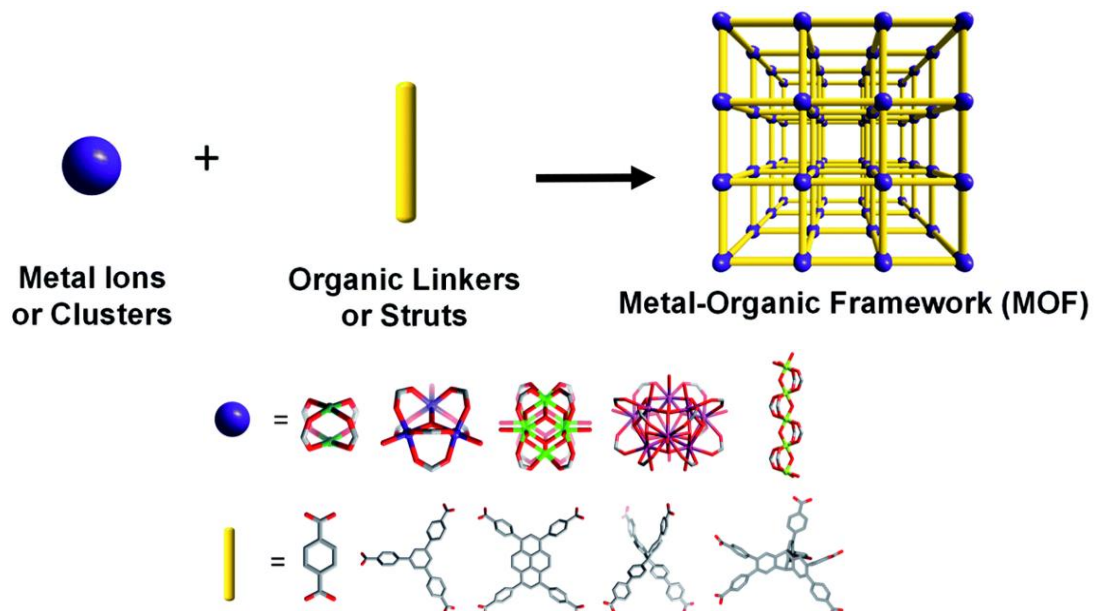


Figure 2: Schematic illustration of a three-dimensional (3D) MOF formation, consisting of metal ions or clusters and organic linker molecules including diverse possibilities shown at the bottom.^[17]

Organic linker molecules possess at least two functional groups in order to coordinate to the metal ions. These groups are mostly electron-rich connection groups, such as carboxylates, imides or nitriles. Different properties can be implemented into the MOF structure by the utilization of additional functional groups on the linker molecule. This can either be done prior to the synthesis, by choosing a modified linker molecule or by post-synthetic modifications (PSMs) via a second reaction step after the MOF structure is formed. The pore sizes of MOF structures often correlate with the length of the incorporated linker molecules. However, if the linker molecule exceeds a certain length, interpenetration takes place and the porosity decreases. Interpenetration describes the pore filling of a MOF with a second identical MOF structure.^[31] Zeolitic-imidazolate frameworks (ZIFs) form a sub-class within the group of MOF materials. These materials are formed by zinc or cobalt ions which are coordinated with imidazole or its derivatives. The naming of this subclass results from the similar bonding angle between metal-imidazole-metal and the one found in zeolites (silicon-oxygen-silicon). In addition, the overall structure and topology exhibited by different ZIFs is highly similar to the ones found within zeolites.^[32,33]

With regard to the nearly infinite amount of possible structures and compositions accompanied by a small pore size distribution, MOFs exhibit great potential for a variety of applications, such as gas storage and separation^[3,9-11], drug-delivery^[14,15], petrochemistry^[12,13], catalysis^[3,4], sensing^[5-8] and more.^[16]

Even though there are already first commercial trials^[17] towards the utilization of MOFs, their relatively low stability under thermal, mechanical and chemical stress is still one of the main drawbacks when it comes to industrial applications. The most prominent commercial attempt is water harvesting. Currently Xu et al. are working on the creation of MOF-based commercial water harvesting devices.^[34] Apart from that some MOFs can now simply be bought online. HKUST-1, MIL-53, UiO-66 and ZIF-8 are produced by BASF and sold via Merck in quantities of up to 500 g.^[35]

2.2 MOFs and their refractive indices

This subchapter focusses on the refractive index (short: RI or n) itself, different ways to influence the RI of MOFs and RI increments.

2.2.1 The refractive index

The RI can be described as the speed of light within a certain material in relation to the speed of light in vacuum. An increased RI corresponds to slower light propagation. Once two different media are involved, it can also be referred to as the change of direction of the light beam (Equation 1).^[36] When the beam of light crosses the interface of two different media, it is refracted away from or towards the interface-normal depending on the RIs of the two media. If the RI of the second medium is higher, than the one of the first medium, the light beam is refracted towards the normal (Figure 3), otherwise the beam of light is refracted outwards.^[36]

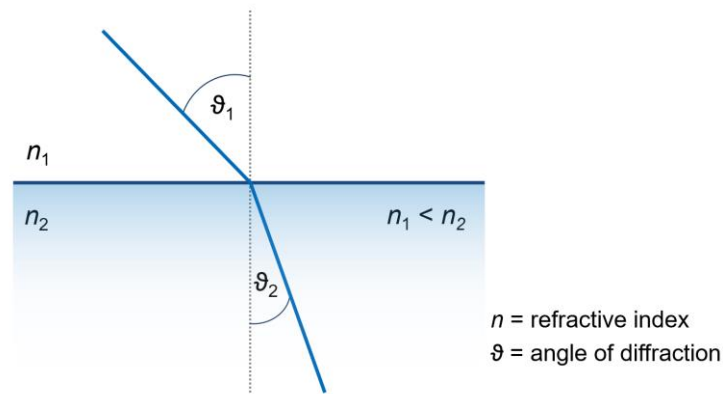


Figure 3: Schematic illustration of the light-beam refraction between two different media.

The angle of diffraction ϑ can be determined by using SNELL'S LAW (Equation 1).^[37]

$$\frac{\sin \vartheta_1}{\sin \vartheta_2} = \frac{n_2}{n_1} = \frac{v_1}{v_2} \quad (1)$$

By convention, the RI is measured at the sodium D-line ($\lambda = 589.3$ nm) and under standard conditions (25 °C, 1 bar).^[38] Additional information regarding RI measurements is given in section 2.2.4.

2.2.2 Refractive index variation within MOFs

The RI of MOFs is tuneable with regard to changing the composition of the structure. Table 1 shows different ellipsometry measurements of different MOFs. They are only comparable within their subgroup, since they were carried out under different initial settings and at different wavelength. However, the provided data is sufficient to provide an insight on the RI tuneability of MOF materials in general.

The most common approach reported in literature to tune the RI of MOFs is pore filling (Table 1a). By incorporating different liquids^[39-41], gases^[18,42] or solids^[43] into the MOF pores, the RI increases. This RI change has also been used for gas sensing applications, as reported by Kim et al.^[18] Since all literature investigations were carried out using ellipsometry, only one RI value was obtained for each sample.

Table 1: Different refractive indices of MOFs reported in literature.

	MOF	Refractive index	Wavelength / nm
a)	HKUST-1 ^[39]	1.39	750
	HKUST-1 (H ₂ O/EtOH) ^[39]	1.52	750
b)	MIL-89 ^[44]	1.65	700
	MIL-89 (H ₂ O) ^[44]	1.45	700
c)	MIL-101 (Cr) ^[45]	1.404	600
	MIL-OH-101 (Cr) ^[45]	1.430	600
	MIL-NH ₂ -101 (Cr) ^[45]	1.434	600
	MIL-NO ₂ -101 (Cr) ^[45]	1.519	600
	MIL-(NO ₂) ₂ -101 (Cr) ^[45]	1.536	600
d)	MIL-NH ₂ -53 (Al) ^[46]	1.292	750
	MIL-NH ₂ -53 (Al)	1.424	750
	PSM with pentanal ^[46]		
e)	MIL-100 (Cr) ^[41]	~ 1.17	n/a
	MIL-100 (Fe) ^[41]	~ 1.43	n/a
f)	[{Fe ₃ (ACTBA) ₂ X·6DEF] _n E ₁ ^[47]	1.84	590
	[{Fe ₃ (ACTBA) ₂ X·6DEF] _n E ₂ ^[47]	2.14	590

In special cases the pore filling is accompanied by the so-called breathing effect. One example is the MIL-89, where the adsorption of water causes the framework to open and enlarge. As a result, the RI unexpectedly decreases (Table 1b).^[44] Interpenetration and interweaving are further possible effects to consider, when investigating the RI of a MOF. Hereby the spaces within one MOF framework are filled with the same, identical network. As a result the initially large pores are divided into smaller ones and the overall density and stability of the framework increases.^[48]

The RI of a MOF structure can additionally be influenced by the choice of linker molecule. Yin et al.^[45,46] reported different mechanisms in order to modify the linker molecule. In 2017 they investigated the effects of post-synthetic modifications to the linker molecule (Table 1d). One year later they determined the RIs of one and the same MOF structure synthesized with different linker molecules (Table 1c). Both approaches showed that the choice of the linker molecule and its modification have a great influence on the measured RI. Lastly, as reported by Márquez et al.^[41], the RI of the same MOF structure can be modified by the exchange of the metal ion (Table 1e). The reported increase, by substituting Cr^{3+} with Fe^{3+} ions, is also consistent with thorough studies performed by Shannon and Fischer. Since Fe^{3+} ions reportedly exhibit a higher polarizability than Cr^{3+} ones, the RI increases.^[49]

In addition, Vinogradov et al. were able to investigate the RI change at different positions (E_1 and E_2) of a MOF single crystal (Figure 4). Upon rotating the single crystal by 90° , they were able to achieve a RI change of 0.3 (Table 1f).^[47]

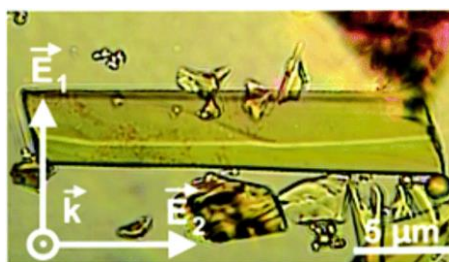


Figure 4: Positioning of the MOF single crystal synthesized by Vinogradov et al. during optical measurements.^[47]

Nevertheless, their positioning could be improved, since triclinic crystals exhibit three, distinguishable RIs (section 2.2.4) and not two.

2.2.3 Refractive index increment systems

The measurement of the RI used to be and still is an important field of mineralogy. It is possible to identify most minerals simply by measuring their RI. Shannon and Fischer investigated RIs and the polarizability of countless inorganic materials and were able to establish a list of 1933 minerals and additional 1000 synthesized compounds.^[49] An excerpt of relevant polarizabilities is given below.

Table 2: An excerpt of provided dynamic polarizabilities of cation by Shannon et al.^[49]

Cation	Coordination number	Dynamic polarizability
Al ³⁺	5	0.500
Cd ²⁺	6	2.700
Cs ⁺	8	3.500
Hf ⁴⁺	8	3.100
K ⁺	8	1.400
Li ⁺	8	0.15
Na ⁺	6	0.430
Rb ⁺	8	2.020
Zn ²⁺	4	1.700
Zr ⁴⁺	8	3.740

Whilst polarizabilities for cations are provided by Shannon and Fischer, values for organic molecules can be found in older publications by Eisenlohr^[50] (Table 3) and Vogel^{[51][52]} (Table 4).

Table 3: Atomic refractions (R_A) after Eisenlohr.^[50,53]

Atom	$R_{\text{Atomic},589\text{nm}}$	Atom	$R_{\text{Atomic},589\text{nm}}$
H	1.100	N primary amines	2.322
C	2.418	N secondary amines	2.502
O in hydroxyls	1.525	N tertiary amines	2.840
O in ethers	1.643	Imides	3.776
O in carbonyl compounds	2.211	Nitriles	3.118
Cl	5.967	per double bond	1.733
Br	8.865	per triple bond	2.398
I	13.900	cyano group CN	5.415

In contrast to the atomic refractions provided by Eisenlohr et al.^[50,53] the list published by Vogel et al.^[51] provides more values. However, not all atoms are represented by two systems, therefore both systems are needed to cover all occurring atoms of molecules included in this work.

Table 4: Atomic refractions (R_A) after Vogel.^[51]

Atom	$R_{Atomic,589nm}$	Atom	$R_{Atomic,589nm}$
H	1.028	S (sulphide)	7.921
C	2.591	SH (thiol)	8.757
O in ethers	1.764	SCN (thiocyanate)	13.400
O in acetals	1.607	NCS (isothiocyanate)	15.615
OH in alcohols	2.546	CN (nitrile)	5.459
F	0.81	CO ₃	7.696
Cl	5.844	NO ₃	9.030
Br	8.741	SO ₃	11.338
I	13.954	PO ₄	10.769
NH ₂ (aliphatic)	4.438	SO ₄	11.090
NH (aliphatic)	3.610	per 3-membered ring	0.614
NH (aromatic)	4.678	per 4-membered ring	0.317
N (aliphatic)	2.744	per 5-membered ring	-0.19
N (aromatic)	4.243	per 6-membered ring	-0.15
ONO (nitrito)	7.237	per double bond	1.575
NO ₂ (nitro)	6.713	per triple bond	1.977

In order to determine the total atomic refraction of a molecule, the individual atomic refractions of each occurring atom needs to be calculated with regard to their stoichiometric factors (m_i) (Equation 2).

$$RI_{atomic,total} = \sum m_i \cdot RI_{atomic}(atom) \quad (2)$$

Both, given polarizabilities of cations and atomic refractions are directly proportional to the RI.

2.2.4 Immersion method

In order to determine anisotropic and even more importantly precise RIs, the immersion method was chosen. The spindle stage setup (see section 4.1.5) enables the user to rotate any plane of the crystal into the microscope stage plane. This means, that each of the up to three RIs can be measured using only one single crystal (Figure 5).^[24]

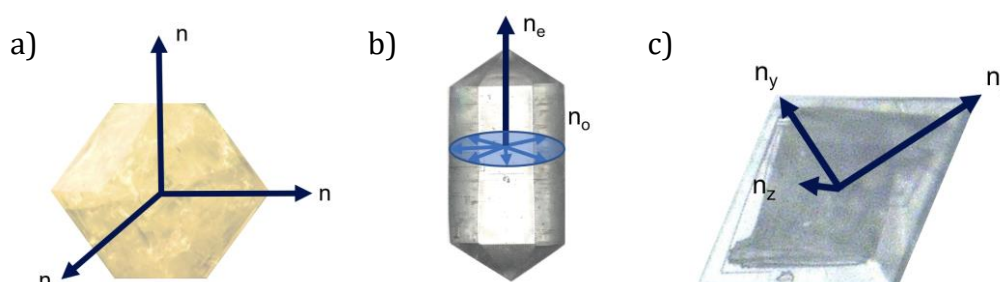


Figure 5: Indicatrix: a) cubic (e.g. ZIF-90), b) hexagonal (e.g. ZIF-68) and c) orthorhombic (e.g. Zr-bzpd) crystal system (n = refractive index, e = epsilon, ω = omega).

Hereby, the number of RIs depends on the crystal system. All cubic crystals are isotropic, also in terms of the RI which stays the same for any given orientation of the crystal (Figure 5a). Tetragonal, trigonal and hexagonal crystals however possess two RIs (epsilon and omega) that are perpendicular to each other. Epsilon has a specific orientation within the crystal that needs to be determined. n_{ω} (n_o) has a perpendicular orientation to n_{ϵ} (n_e). Within the perpendicular plane to epsilon, omega does not change its RI value (Figure 5b). Orthorhombic, monoclinic and triclinic crystals exhibit three RIs (Figure 5c) n_x , n_y and n_z . These three RIs represent the infinite number of refractive indices present in the anisotropic crystal system. The orientation of them can occasionally match with the crystal habitus, but it does not have to. In all cases, the RI of the n_z is perpendicular to the area spread by the RIs of n_x and n_y .^[54] To determine the exact positions of both the different RIs and the matching orientation of the mounted single crystal, extinction data is required in order to measure them successfully. By the use of a polarization filter, the points of extinction along the spindle stage are measured (Appendix Figure 1). The data is then recorded with the program *excalibrw* and the positions are calculated (Appendix Figure 2).^[55] Afterwards, the single crystals is oriented according to the obtained angles and the RI is measured.^[24]

The key aspect of this measurement technique is the immersion effect. When the mounted single crystal is surrounded by a liquid that matches its RI, it becomes invisible to the eye (Figure 6).

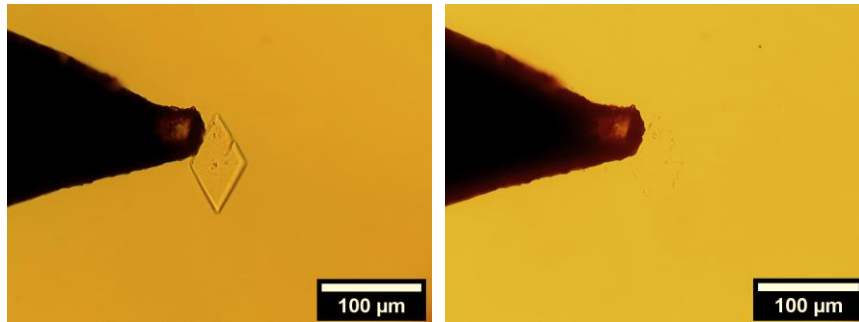


Figure 6: Pictures taken during an immersion measurement (left: RIs of the liquids and crystal do not match; right: point of immersion – RIs match).

In order to find the point of immersion Becke lines can be used as an indicator. If the microscopic stage is lowered, the enlightened outline moves towards the medium with the higher RI (Figure 7).

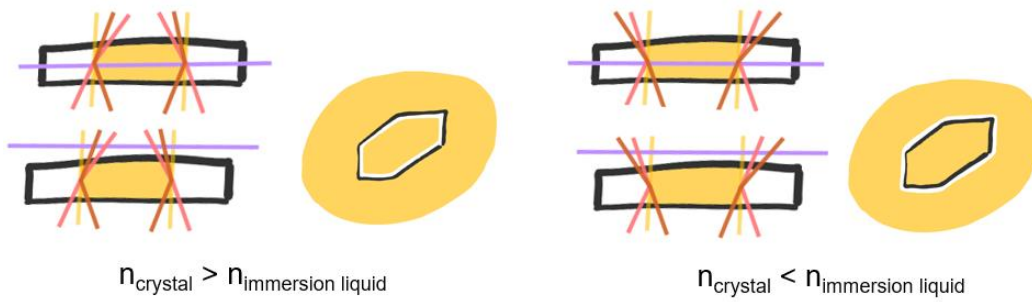


Figure 7: Illustration of the Becke lines (the microscope stage is displayed by the purple line).

2.3 MOF single crystals: Syntheses and structures

Synthesizing single crystals of MOFs is essential in order to precisely determine their structure. The first MOF single crystals of MOF-5^[2] and HKUST-1^[56] were synthesized in 1999. These single crystals were large enough to obtain structural information from single crystal x-ray diffraction measurements. Larger, millimetre-sized MOF-5 single crystals were later acquired by Han et al. in 2010.^[57]

MOF single crystals can be obtained using different synthesis methods. The most commonly used one is the modulated synthesis. Kitagawa et al.^[58], Schaate et al.^[59], Carmona et al.^[60] and many more were able to use this approach successfully to obtain MOF single crystals. In general, modulators are molecules equipped with only one functional group that can connect to the metal ion. E.g., if the MOF structure contains dicarboxylic acids as linker molecules, the chosen modulators are usually monocarboxylic acids. The competition between modulator and linker molecules slows down the nucleation and thus favours the growth process (Figure 8). Besides, modulators can temporarily block coordination sites at the metal ion. As a result, it is much easier to control and tune the crystal growth.^[58]

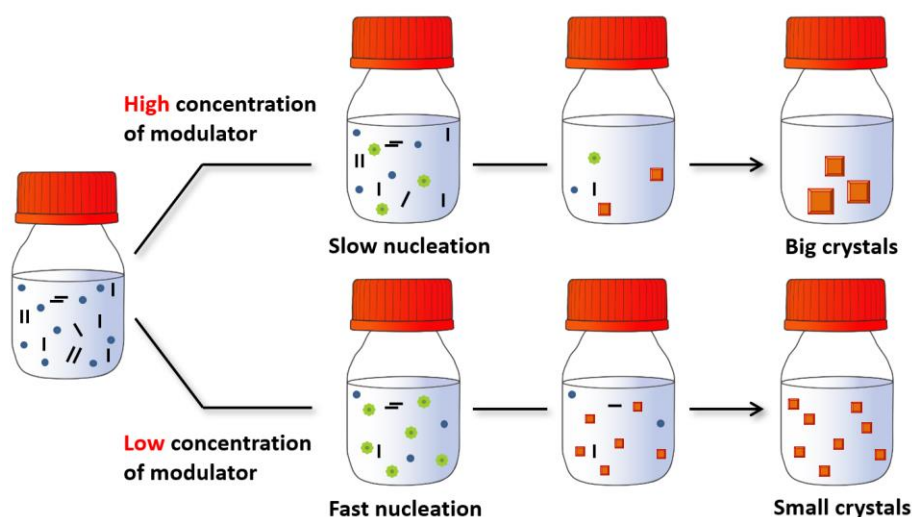


Figure 8: Illustration of the modulation approach (linker molecules are represented by black lines, metal ions by green spheres, crystal nuclei by blue spheres and (single) crystals by red squares).^[58]

Apart from the nucleation rate and crystal size, the crystal morphology is tuneable by the modulation approach as well.^[58-61] However, when the modulation approach is used for single crystal synthesis, defect formation also needs to be considered. Since the linker molecule competes with the modulator for coordination sites on the metal ions, increasing the amount of modulator used also increases the number of missing linker defects.^[62] In the case of single crystal synthesis this effect is often unwanted. Nevertheless, these defects are desirable in application fields like catalysis or particle confinement.^[63]

Another approach for single crystal synthesis is diffusion-controlled nucleation and crystal growth. Since this synthesis method relies on diffusion it is very slow. Reaction times can easily be several months. The advantages of the diffusion-controlled syntheses are an uniform oversaturation combined with an diffusion induced, constant layer-by-layer growth. Also, due to the long reaction times and constant growth, the sufficient super-saturation for nucleation to occur usually is not reached. This method can not only be carried out at room temperature^[64], but also at high temperatures and under solvothermal conditions^[65]. Details for a diffusion-controlled single crystal synthesis are given in section 4.2.10, where Figure 23 also displays the used reaction setup. Moreover, single crystals can be grown at a solvent interface. Typically two solutions, one containing the metal source and one containing the linker molecule, can be layered by using different solvents with different densities.^[66] Seeding is also reported in the literature to further induce single crystal growth. Smaller, pre-synthesized particles are added into the reaction mixture to induce heterogeneous nucleation. Over the course of the reaction process, single crystals grow from these seeds.^[64,67]

In addition, most MOF syntheses exhibit a very narrow synthesis window for single crystal formation. The ideal single crystal reaction conditions and parameters need to be determined through accurate screening. The parameters include the ideal metal-linker ratio, as well as the selected solvent, reaction temperature, reaction time and more. Thus, there are a variety of factors that need to be considered, which is why these parameters are often researched by using high-throughput screening.^[33]

The following subchapters will describe each MOF structure of which we were able to successfully synthesize single crystals later on. Unsuccessful MOF syntheses and their structures were left out for clarity. A list of performed syntheses and their outcome ^[34] can be found in Table 5.

Table 5: Performed MOF single crystal syntheses with regard to the reported literature and their outcome. Successful syntheses are discussed in subchapter 4.2.

MOF	Reference	Yield of single crystals
<i>Al-pydc</i>	Wharmby et al. ^[68]	Successful
<i>Cd-bzpd</i>	Qin et al. ^[69]	Successful
<i>Hf-bzpd</i>	adapted from ^{[70][71]}	Successful
<i>Sn(IV)-bzpd</i>	adapted from ^[71]	Unsuccessful
<i>Zn-bzpd</i>	Qin et al. ^[69]	Successful
<i>Zr-bzpd</i>	Mohmeyer et al. ^{[70][71]}	Successful
<i>Zr-bzpd</i> with various PSM reagents	Mohmeyer et al. ^[72]	Loss of single crystallinity
$Ce_2(NDC)_3(DMF)_2$	Atorzi et al. ^[73]	Crystals – unsuitable for RI measurement
UTSA-25	Chen et al. ^[74]	Unsuccessful
UTSA-36	Das et al. ^[75]	Unsuccessful
UTSA-38	Das et al. ^[76]	Unsuccessful
UTSA-74	Bueken et al. ^[77]	Successful
<i>In-bdc-NH₂</i>	Krüger et al. ^[78]	Unsuccessful
<i>In-bdc-H/NH₂</i>	Krüger et al. ^[78]	Unsuccessful
<i>In-bdc-NH₂/NO₂</i> cubic	Krüger et al. ^[78]	Unsuccessful
<i>In-bdc-NH₂/NO₂</i> octahedral	Krüger et al. ^[78]	Unsuccessful
K- α -CD MOF	Sha et al. ^[79]	Single crystals – not stable
Na- α -CD MOF	Sha et al. ^[79]	Single crystals – not stable
Rb- α -CD MOF	Sha et al. ^[79]	Single crystals – not stable
Ge,Li- β -CD MOF	Brenner et al. ^[80]	Unsuccessful
K- β -CD MOF	Lu et al. ^[81]	Single crystals – not stable
Mn,Li- β -CD MOF	Brenner et al. ^[80]	Unsuccessful

MOF	Reference	Yield of single crystals
Na- β -CD MOF	Lu et al. ^[81]	Single crystals – not stable
Cs- γ -CD MOF	Kim et al. ^[64]	Successful
K- γ -CD MOF	Kim et al. ^[64]	Successful
Li- γ -CD MOF	adapted from ^[64]	Successful
Na- γ -CD MOF	Forgan et al. ^[82]	Successful
Rb- γ -CD MOF	Kim et al. ^[64]	Successful
SrB ₂ - γ -CD MOF	Forgan et al. ^[82]	Unsuccessful
ImNaAl	Ptak et al. ^[83]	Unsuccessful
UiO-66	adapted from ^{[62][71]}	Successful once
UiO-66-NO ₂	adapted from ^{[62][70]}	Successful once
Zr-cal	Schulz et al. ^[5]	Unsuccessful
Zr-FA	Liang et al. ^[84]	Unsuccessful
Zr-fum	Furukawa et al. ^[85]	Unsuccessful
Zn(3-ptz) ₂	Garfido et al. ^[86]	Unsuccessful
SOD-ZMOF	Liu et al. ^[87]	Unsuccessful
ZIF-2	Banerjee et al. ^[88]	Unsuccessful
ZIF-4	Banerjee et al. ^[88]	Unsuccessful
ZIF-7	Park et al. ^[33]	Successful
ZIF-8	Lee et al. ^[89]	Successful
ZIF-10	Banerjee et al. ^[88]	Unsuccessful
ZIF-11	Banerjee et al. ^[88]	Unsuccessful
ZIF-14	Banerjee et al. ^[88]	Unsuccessful
ZIF-60	Banerjee et al. ^[88]	Unsuccessful
ZIF-61	Banerjee et al. ^[88]	Unsuccessful
ZIF-62	Banerjee et al. ^[88]	Unsuccessful
ZIF-64	Banerjee et al. ^[88]	Unsuccessful
ZIF-68	Banerjee et al. ^[90]	Successful
ZIF-69	Banerjee et al. ^{[70][90]}	Successful
ZIF-70	Banerjee et al. ^[90]	Successful
ZIF-71	Banerjee et al. ^[88]	Unsuccessful
ZIF-72	Banerjee et al. ^[88]	Unsuccessful
ZIF-78	Banerjee et al. ^[90]	Successful

MOF	Reference	Yield of single crystals
ZIF-79	Banerjee et al. ^[90]	Unsuccessful
ZIF-80	Banerjee et al. ^[90]	Unsuccessful
ZIF-81	Banerjee et al. ^[90]	Successful
ZIF-82	Banerjee et al. ^[90]	Successful
ZIF-90	adapted from ^[91]	Successful
ZIF-91	Morris et al. ^[91]	Unsuccessful
ZIF-92	Morris et al. ^[91]	Unsuccessful
ZTIF-1	Wang et al. ^[92]	Unsuccessful

2.3.1 Al-*pydc*

The Al-*pydc* MOF consists of Al³⁺ metal ions and 2,6-pyridinedicarboxylic acid (H₂*pydc*) as linker molecule. This MOF consists of dimeric, edge-sharing [Al(μ-OH)(H₂O)(2,6*pydc*)]₂ units (Figure 9 a). These dimeric units are then connected via hydrogen bonds to form the MOF structure itself (Figure 9 b,c). Each Al³⁺ ion is coordinated by five oxygen atoms. Its structure is very densely packed (Figure 9 c) and thus shows a low porosity. The Al-*pydc* MOF exhibits a thermal stability of up to 325 °C.^[68]

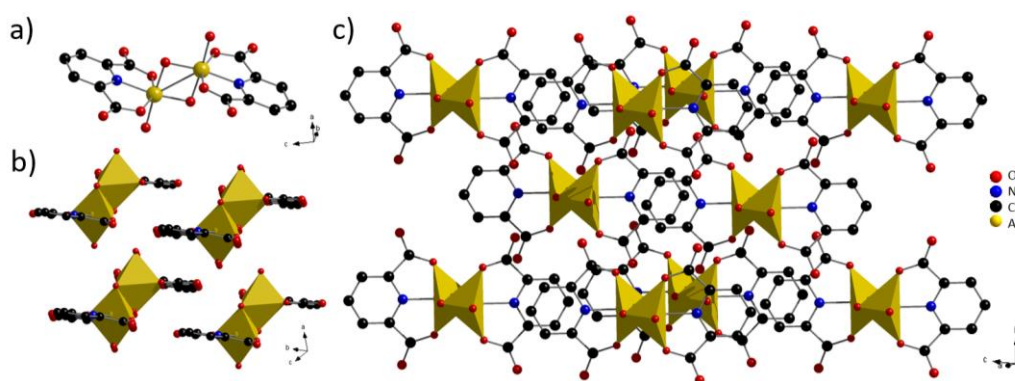


Figure 9: The crystal structure of the Al-*pydc* MOF a) one dimeric unit, b) structure along the 010 plane (in perspective), c) overall structure density. Hydrogen atoms were left out. The structure was illustrated with Diamond 3.1 software using the cif file provided by Wharmby et al.^[68]

2.3.2 Cd- and Zn-*bzpd*

The Cd-*bzpd* and the Zn-*bzpd* MOF both show the same crystal structure.^[69]

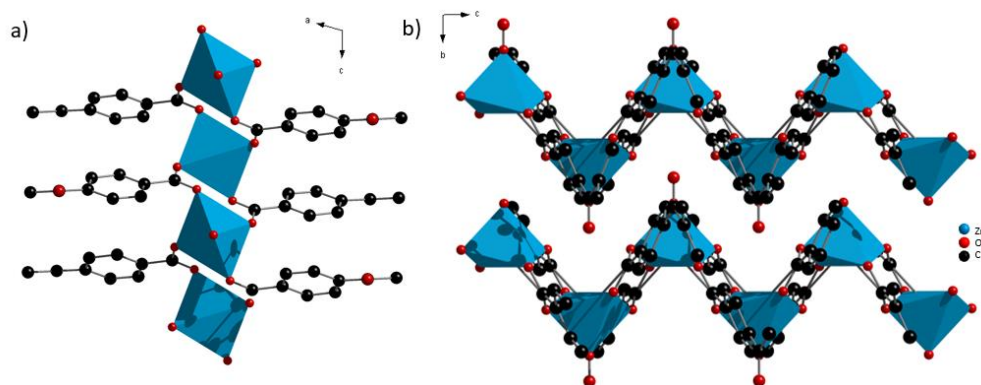


Figure 10: Crystal structure of Zn-*bzpd* with a) 1D metal ion-carboxylate chains, b) 3D packing of the wavelike 2D layers. Hydrogens atoms are not displayed to achieve higher clarity. The structure was illustrated with Diamond 3.1 software using the cif file provided by Qin et al.^[69]

One-dimensional chains of metal oxo clusters are connected by benzophenone-4,4'-dicarboxylic acids (*H₂bzpd*c) to wavelike 2D structures (Figure 10). Each metal ion is coordinated by five oxygen atoms. Via hydrogen bonds these 2D layers are then connected to a three-dimensional framework (Figure 10 b). Both MOFs possess a thermal stability up to 370 °C.^[69]

2.3.3 Hf- and Zr-*bzpd*c

In 2018, a novel zirconium-based MOF was discovered by our work group.^[71] Since both *Hf-bzpd*c and *Zr-bzpd*c, exhibit the same XRD pattern and crystal morphology and Zr^{4+} and Hf^{4+} metal ions possess highly similar properties, their overall crystal structure is assumed to be the same. Figure 11 a shows the Zr-IBU. Here, six zirconium ions are coordinated by four linker molecules. The remaining coordination sites are filled with hydroxy groups and one modulator molecule. Each Zr^{4+} ion is therefore coordinated by eight oxygen atoms. The IBUs are connected by the linker molecules to 2D layers (Figure 11 b) which then build a 3D framework via hydrogen bonds (Figure 11 c). The 1D-channel pore size is about 8 Å.^[71]

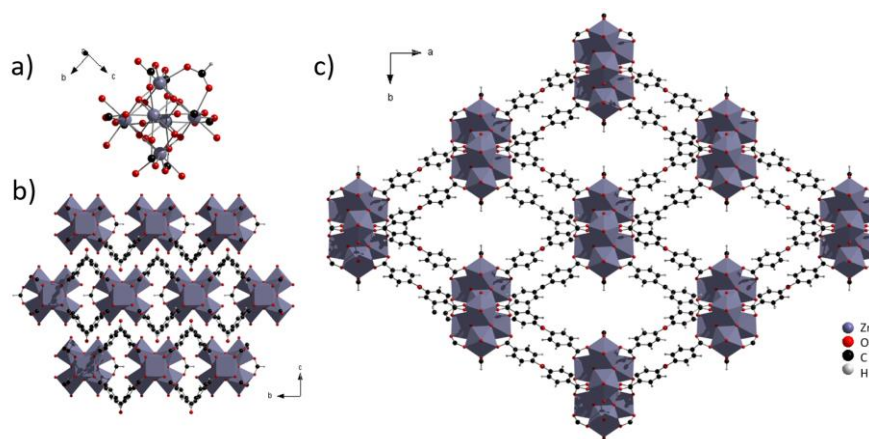


Figure 11: Illustrations of the crystal structure of *Zr-bzpd* a) Zr-IBU, b) 2D layer structure viewed along the a-axis, c) display of the 3D structure along the c-axis. The structure was illustrated with Diamond 3.1 software using the cif file provided by Mohmeyer et al.^[71]

The MOF exhibits a great thermal stability of up to 400 °C and offers a rare possibility to connect any molecule with a C-H-bond directly to the linker molecule under UV-irradiation (Figure 12).^[71,72,93,94]

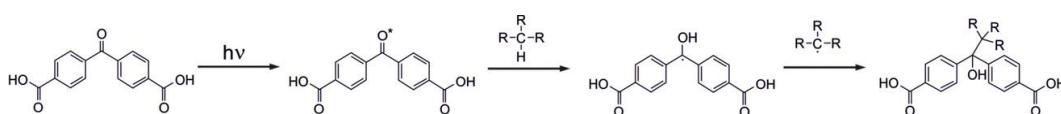


Figure 12: Schematic reaction mechanism for the PSM of the Hf- or Zr-*bzpdC* MOFs. The reaction scheme is directly taken from literature.^[71]

2.3.4 UiO-66 and UiO-66-NO₂

UiO-66 (Universitetet i Oslo-66) refers to a MOF build from Zr⁴⁺ ions and terephthalic acid (*H₂bdc*).^[95] UiO-66-NO₂ exhibits the same overall structure, but instead of *H₂bdc* it is built with its 2-nitroterephthalic acid derivative (*H₂bdc*-NO₂). Figure 13 a displays the Zr-IBU [Zr₆O₄(OH)₄(CO₂)₁₂] which contains six Zr⁴⁺ ions. Each one is square-antiprismatically coordinated by eight oxygen atoms.^[95] If the structure is broken down to IBUs, it can also be seen as a cubic closest packing (Figure 13 b,c).^[96] UiO-66 possesses a thermal stability of up to 375 °C.^[97] Its pore diameters are 11 Å for the octahedral pore and 8 Å for the tetrahedral one.^[98]

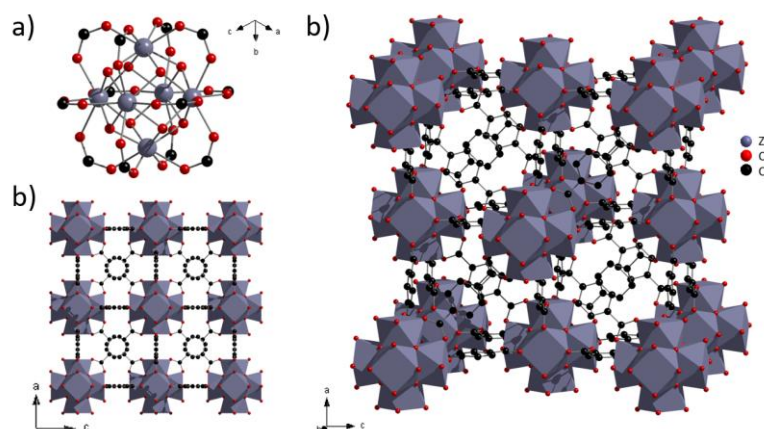


Figure 13: UiO-66 crystal structure: a) Zr-IBU, b) view along the b-axis, c) overall view of the unit cell. Hydrogens atoms are not shown for clarity. The structure was illustrated with Diamond 3.1 software using the cif file provided by Trickett et al.^[62]

2.3.5 UTSA-74

The UTSA-74 (University of Texas at San Antonio-74) is built from Zn^{2+} metal ions and benzene-1,2,4,5-tetracarboxylic acid ($\text{H}_2\text{bdc}(\text{OH})_2$).

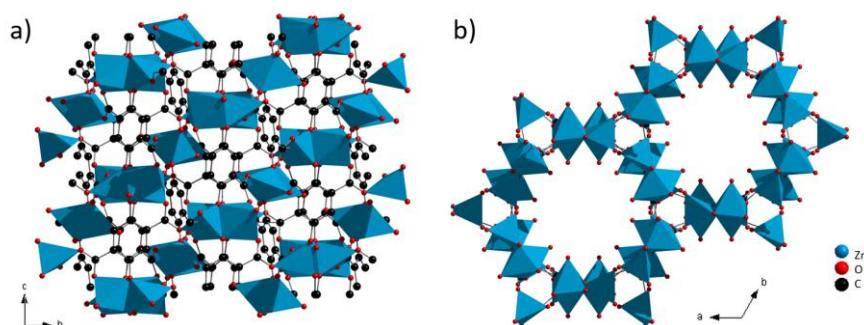


Figure 14: Crystal structure of the UTSA-74 a) view along the a-axis, b) view along the c-axis. Hydrogen atoms are not shown to increase the clarity. The structure was illustrated with Diamond 3.1 software using the cif file provided by Bueken et al.^[77]

Within the UTSA-74 structure, two coordination states for the zinc cation are present (Zn_1^{2+} and Zn_2^{2+}). Zn_1^{2+} is tetrahedrally coordinated by four oxygen atoms and Zn_2^{2+} is octahedrally coordinated by eight oxygen atoms. Both zinc ions form a binuclear IBU. Upon incorporation of the linker molecules, the IBUs are connected to form a 3D framework (Figure 14). Its 1D channels along the c-axis (Figure 14 b) have a diameter of about 8 Å.^[99]

2.3.6 γ -CD MOFs (Cs, K, Li, Rb)

The γ -cyclodextrin (γ -CD) MOFs use γ -CD as the linker molecule which is connected by different cations (Figure 15). For monovalent caesium, potassium, lithium and rubidium cations, the formed structures are almost identical, with only very slight variations in their lattice parameters (less than 10 %). The pore size of these structures is determined by the diameter of γ -CD, which is about 7.8 Å. Every cation is coordinated by 8 oxygen atoms. In general γ -CD MOFs exhibit an overall rather weak temperature and chemical stability.^[64]

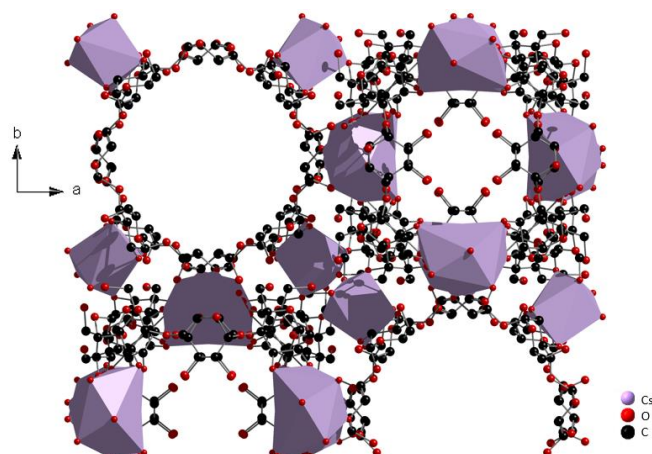


Figure 15: Crystal structure of the γ -CD MOFs viewed along c-axis. Hydrogen atoms are not displayed. The structure was illustrated with Diamond 3.1 software using the cif file provided by Kim et al.^[64]

2.3.7 Na- γ -CD MOF

In contrast to the γ -CD MOFs described in section 2.3.6, the Na- γ -CD MOF does not exhibit a cubic symmetry. Instead it features a triclinic crystal system. However, the pore size is still restricted by the size of the linker γ -CD (Figure 16 b) and therefore cannot exceed 7.8 Å. γ -CD molecules are connected via monovalent sodium cations to a 3D network (Figure 16a). Each sodium cation is coordinated by six oxygen atoms. ^[82]

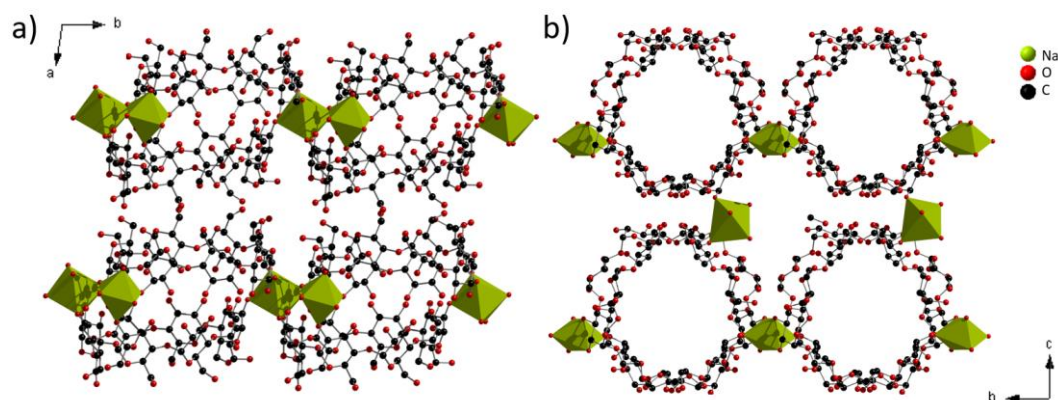


Figure 16: Crystal structure of the Na-MOF γ -CD viewed a) along c-axis and b) along a-axis. Hydrogen atoms are not included. The structure was illustrated with Diamond 3.1 software using the cif file provided by Forgan et al.^[82]

2.3.8 ZIF-7

Zeolitic imidazolate frameworks (ZIFs) are a sub-category of MOFs. In contrast to regular MOFs, ZIFs can only contain imidazoles as linker molecules.^[32,100] Their name corresponds to their similarities with zeolites. Both exhibit tetrahedrally coordinated metal ions, as well as a similar binding angle of about 145° (subchapter 2.1).^[33,88,101] The MOF structure of ZIF-7 is a distorted form of the sodalite topology found in zeolites and in ZIF-8. Benzimidazole linker molecules are connected by Zn^{2+} cations to form a 3D framework. Its pores (Figure 17 a) are bridged by 4.3 \AA sized windows (Figure 17 b). Each zinc ion is tetrahedrally coordinated by four nitrogen atoms.^[33]

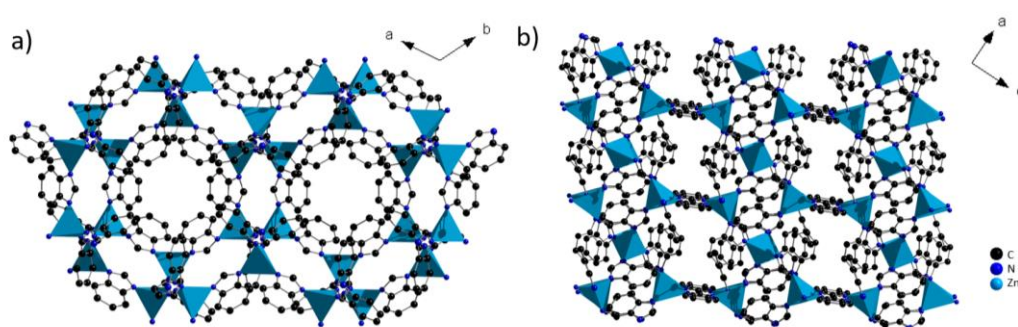


Figure 17: The crystal structure of ZIF-7 a) view along the c-axis and b) along the b-axis. Hydrogen atoms are not displayed. The structure was illustrated with Diamond 3.1 software using the cif file provided by Park et al.^[33]

2.3.9 ZIF-8 and ZIF-90

As mentioned, ZIF-8 crystallizes in the zeolite topology sodalite (Figure 18). ZIF-8 and ZIF-90 both exhibit the same structure with the exception that ZIF-8 uses 2-methylimidazole as linker molecule and ZIF-90 2-imidazole-carboxaldehyde. ZIF-8 pores demonstrate a 11.6 \AA diameter and are connected by 3.4 \AA windows (Figure 18).^[33] The pores of ZIF-90 are connected via 3.5 \AA windows and show a diameter of 11.2 \AA .^[91]

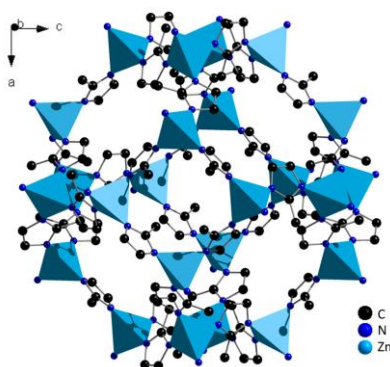


Figure 18: The crystal structure of ZIF-8. No hydrogen atoms were displayed for clarity. The structure was illustrated with Diamond 3.1 software using the cif file provided by Morris et al.^[102]

2.3.10 ZIF-68 to ZIF-70, ZIF-78, ZIF-81 and ZIF-82

In contrast to ZIF-7, -8 and -90, these ZIFs consists of two linker molecules.

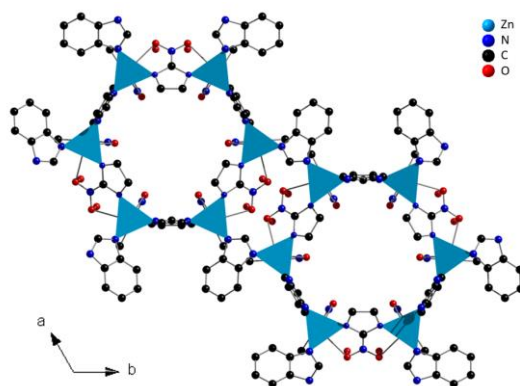


Figure 19: ZIF-68 crystal structure (gmelinite topology) viewed along the *c*-axis. Hydrogen atoms are not displayed to increase clarity. The structure was illustrated with Diamond 3.1 software using the cif file provided by Morris et al.^[88]

All of them contain 2-nitroimidazole, whereas the second linker molecule varies (ZIF-68: benzimidazole, ZIF-69: 5-chlorobenzimidazole, ZIF-70: imidazole, ZIF-78: 5-nitrobenzimidazole, ZIF-81: 5-bromobenzimidazole, ZIF-82: 4-cyanoimidazole). Their structure exhibits larger pores along the *c*-axis with a diameter of about 7.8 Å (Figure 19). In addition, along the *a*- and *b*-axis, smaller pores can be found.^[103]

2.4 Perovskites

Perovskite materials possess an ABX_3 structure, where A and B represent cations and X represents anions. B cations are octahedrally coordinated by six X anions each. The so-formed octahedras are corner-shared and form a three-dimensional framework. Within the cavities of the built framework, A-site cations are located (Figure 20). The first perovskite to be discovered was $CaTiO_3$, which was named in honor of Lev Perovski. Depending on the perovskite composition, properties like ferroelectricity^[104,105], magnetoresistance^[106,107] and superconductivity^[108,109] can be exhibited. Besides 3D^[110] perovskite structures also 2D^[111], 1D^[112] and 0D^[113,114] structures of perovskites were researched.^[115-117] Besides the ABX_3 structure, also zero-dimensional A_4BX_6 structures (Figure 20) are known and also exhibit e.g. luminous properties.^[118]

Perovskites can also be formed by using monovalent A-site cations, such as Cs^+ , $CH_3NH_3^+$ (MA) or $HC(NH_2)_2^+$ (FA). B-site cations can moreover be replaced by a variety of divalent cations (e.g., Pb^{2+} , Ge^{2+} , Mg^{2+} , Sn^{2+} , Sr^{2+} , Ca^{2+} , Ni^{2+} or Cu^{2+}). For X-site cations usually halides or pseudohalides are chosen. The so-formed perovskites can exhibit excellent optical properties and are especially applicable for the fields of light-emitting devices^[119-121] and solar cells^[122,123]. Perovskites containing MA, FA, etc. cations are referred to as organic-inorganic perovskites, whereas perovskites with A-site metal-cations are known as all inorganic.^[115]

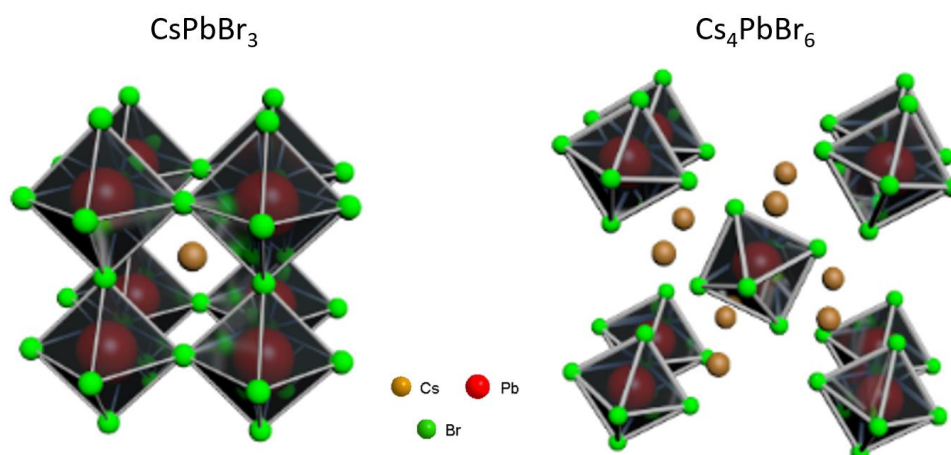


Figure 20: Illustration of the perovskite crystal structure of $CsPbBr_3$ (left) and Cs_4PbBr_6 (right).^[118]

With regard to light-emitting devices, perovskites (especially halide perovskites) are considered to be the next-generation of emitting materials.^[124-127] Their narrow half-width maximum combined with the high colour purity and tunable emission wavelength makes them excellent candidates for lighting devices and displays. In addition, perovskites exhibit a high photoluminescence quantum yield (PLQY) close to unity (100 %) and their fabrication comes at a relatively low cost compared to other established lighting devices (such as cadmium-based quantum dots).^[128]

2.5 Perovskite-MOF materials

One of the main challenges regarding perovskites is their sensitivity to light, oxygen and heat exposure.^[26,27] In order to prolong the lifetime of perovskites, the porous framework structure of MOF materials offers great protection properties. By the confinement of perovskite quantum dots and nanocrystals within a MOF structure, the storage abilities under ambient conditions increase significantly. Furthermore, the thermal- and photo-stability could be increased, too. Another problem for mixed halide perovskite is anion exchange or anion migration. Upon the incorporation of differently composed perovskites in MOF materials, no anion migration took place within the investigated timeframe as reported by Ren et al.^[28,29] The stability increase will be described more in detail later on.

Apart from metal-organic frameworks, other materials, such as mesoporous silica, polymers, zeolite and metal oxides were tested for perovskite confinement. ^[129-135] Due to their diversity and tunability, MOFs are considered to be a great choice when it comes to the selection of the protecting structure of perovskite confinement.^[136-142] Due to the combination of the diverse properties of the perovskite materials and the tunable assets of the MOF host matrix, the created hybrid materials can also find applications in other fields, such as information security^[143-145], photocatalysis^[146,147,148], detection and sensing^[124,149-156]. However, Perovskite-MOF materials are a very young research field and further progress needs to be made.^[157]

In general, the synthesis strategies for perovskite-MOF composite materials can be subdivided into the so-called ship-in-bottle approach and bottle-around-ship approach (Figure 21).^[136,137]

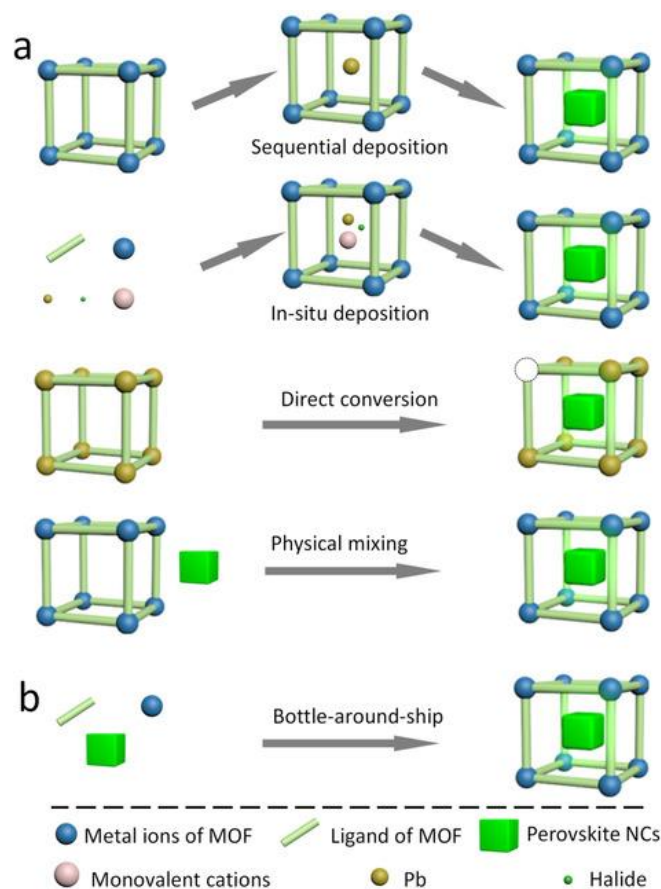


Figure 21: Strategies for the syntheses of perovskite-MOF materials: (a) ship-in-bottle approach, (b) bottle-around-ship approach.^[157]

When using the ship-in-bottle strategy, perovskite precursors or pre-formed nanocrystals are directly inserted into the already built MOF structure. The formation of perovskites within the MOF structure can either be obtained by sequential deposition or in-situ deposition. For the sequential deposition, the MOF is already pre-synthesized and the perovskite is formed in a post-synthetic procedure. In-situ deposition considers the formation of both MOF and perovskites from a mixture of their components simultaneously.

The most common-used ship-in-bottle method is the sequential deposition. So far, it has been performed for a series of MOFs, such as HKUST-1, UiO-66, UiO-67, ZJU-28, etc.^[28,143,146,149,158-163] The sequential deposition method will also be used for the studies in this work. Apart from the deposition techniques, physical mixing and direct conversion approaches were also used for perovskite confinement. In the direct conversion method, the MOF structure

itself is used as a partially sacrificial porous template. Zhang et al. synthesized a Pb-MOF structure where the lead ions were removed from the framework structure by the MAPbBr_3 perovskite formation in the second synthesis step. Whilst decreasing the stability of the MOF host matrix through the partial destruction, the direct conversion method offers an effective and fast way to incorporate a large amount of perovskite nanocrystals into the MOF. This approach therefore results in a high loading capacity. [144,164] Physical mixing can be applied, when the chosen MOF structure already exhibits mesopores. In order to create mesopores within a microporous MOF structure, templating syntheses can be used. [158] However, there still are some limitations to be considered, when choosing the ship-in-bottle approach. On the one hand, the diffusion resistance lowers the overall diffusion rate and increases the probability for heterogeneous nucleation. So, the formation of perovskite nanocrystals on the MOF surface instead of the MOF interior is favoured. On the other hand, it is still very difficult to control the size, shape and location of the formed perovskite nanocrystals inside the MOF structure. [157]

For the bottle-around-ship approach, the pre-synthesized perovskite nanocrystals are coated with the MOF matrix. Nevertheless, only a few MOF synthesis routes exhibit the necessary properties for this method. Since stabilized perovskite nanocrystal still exhibit a relatively low temperature stability and are sensitive to polar solvents, most MOF synthesis routes are too harsh and would destroy the pre-synthesized perovskite nanocrystals. Only MOFs, which can be synthesized under mild conditions are suitable for the bottle-around-ship method. So far, perovskite nanocrystals were coated with ZIF-8, ZIF-67 and Eu-*btc*. [147,150]

In order to achieve satisfactory PLQY values, a perovskite size between 10 and 20 nm is ideal. Therefore, mesopore-sized defects need to be introduced into the MOF structure. Defect-engineering can be performed by the addition of formic acid. Linker vacancies are created, due to the competition between the linker molecule and formic acid, which both possess a carboxylic group to connect to the zirconium cation. If these linker vacancies increase, they also lead to missing cluster defects and thus create mesopores. [165][28,158] Larger pores also include the advantage of an increased loading capacity, which also

corresponds to a higher photoluminescence intensity. Furthermore, the large diffusion resistance of the microporous MOF structures can be decreased by the creation of defects and thus larger pores. The purification of the as-synthesized MOF structure also plays an important role, since remaining solvent, modulator or precursor molecules not only take up valuable space, but perovskites are also very sensitive to these polar substances.^[166-168]

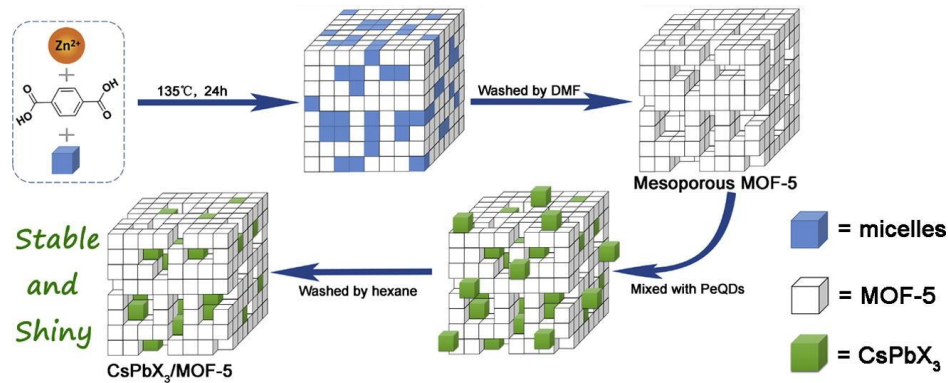


Figure 22: Schematic illustration of the synthesis strategy for mesoporous MOF-5 crystals, including perovskite confinement.^[158]

Additional purification should be carried out after the perovskite confinement procedure, since a high percentage of perovskites are formed on the MOF surface and therefore are not protected by the framework. These perovskite nanocrystals should be removed by e.g. additional washing for better optical properties and a more precise characterization of the overall material.^[157]

Apart from various defect-engineering approaches, different methods for the as described sequential deposition techniques were investigated, too. Ren et al. crystallized perovskites at high temperatures (160 °C) into the MOF pores.^[28] In contrast to the high temperature perovskite confinement, Cha et al. introduced a procedure at room temperature and under ambient conditions for perovskite confinement.^[161]

Apart from the creation of MOF-perovskite materials, MOFs can also be implemented into perovskites as a sacrificial, defect-healing agent as published by Oh et al.^[169] Upon the decomposition of ZIF-8, zinc ions can passivate uncoordinated defect sites. Hou et al. furthermore used liquid phase sintering of MOFs and perovskites to improve the perovskite phase stability. The MOF glass interface passivates the perovskites surface defects and enables a high stability even when immersed into water for several hours.^[170]

3 Objectives

The main objective for this work was to measure reliable, precise and anisotropic refractive indices (short: RIs) of MOFs.

With the start of the cluster of excellence PhoenixD (Photonics, Optics, Engineering Innovation across Disciplines) at the Leibniz University of Hanover, the need for optic materials with a broad range of RIs was desired. The huge variety among MOF structures and their components leads to enormous possibilities with regard to the above-mentioned requirement. The main method to measure the RI of MOFs so far is the ellipsometry method. However, results of this method do not seem to be consistent, as reported in literature.^[22] Therefore, the above-mentioned need for a reliable measurement method was established. Herein, the immersion method was investigated as a possible, new method to obtain precise and in addition to ellipsometry also anisotropic RIs.

Apart from the main objective of optical characterization of MOF materials, their optical application was also of interest within PhoenixD. The second part of the thesis therefore investigates the optical application of MOF materials within light-emitting devices. MOF-perovskite materials were investigated with regard to their stability and structural composition.

Summarizing the main objectives of this work are:

- Syntheses of a broad range of large MOF single crystals
- Anisotropic RIs measurements of MOF single crystals using the immersion method
- Verification of the usability of the immersion method towards RI measurements of MOF single crystals
- Investigation if immersion liquids enter the MOF framework, influencing the intrinsic RI
- Optical application of MOF-perovskite materials as LEDs

4 Experimental Section

This chapter is split into three subchapters. The first one describes each analytical method used in this work. The second and the third one focus on the synthesis of the used materials.

4.1 Analytical Methods

In the following subchapter, the chosen analytical methods for the characterization of the synthesized materials are described. For commonly used characterization methods in this research field only the measurement parameters are given.

4.1.1 Powder X-Ray Diffraction

By using the powder X-ray diffraction (p-XRD) measurement, the crystallinity, crystal structure and the phase purity of different compounds can be investigated.^[178]

P-XRD measurements of MOF single crystals: As for the preparation, the sample was placed between two X-ray amorphous films. If only a small amount of the product was obtained, vacuum grease was used to prevent the material from moving out of the X-ray beam focus region. All measurements were performed with a STADI P diffractometer of STOE in transmission geometry. The diffractometer used Ge(111)-monochromatised Cu-K α_1 -rays ($\lambda = 1.5406 \text{ \AA}$). For the measuring range $2 - 50^\circ 2\theta$ was chosen, as well as a step size of $0.1^\circ 2\theta$ -steps. The measuring time per step was 10 s. The backscattering was detected with a positional sensitive detector. For evaluation of the measured diffractograms the program WinXPow 1.08 by STOE was used.

P-XRD measurements of materials for LED application:

All measurements were carried out and evaluated by employees of the Material Analysis Centre of Seoul National University using the D8 ADVANCE diffractometer by Bruker with Cu-K α_1 -rays ($\lambda = 1.5406 \text{ \AA}$). For the measuring range $2 - 50^\circ 2\theta$ was chosen with a step size of $0.02^\circ 2\theta$ -steps. The measuring time per step was 4 s. All diffractograms were displayed with the help of the OriginPro 2019 software by OriginLab.

4.1.2 Light-Optical Microscopy

With the use of light-optical microscopy, magnified images of the synthesized MOF single crystals could be obtained.

The single crystals were positioned on a glass microscopic slide on top of the black background of the microscopic stage. Optical images were collected at the Hanover Center of Optical Technologies (HOT) with a VHX-7100 digital microscope by KEYENCE. All images were further modified with the software ImageJ.

4.1.3 Physisorption

Physisorption measurements were carried out for the determination of porosity. With DFT-calculations, further information about the pore sizes and pore size distribution could be gained.

All samples were activated at 120 °C for 24 h under vacuum prior to measurements, to eliminate possible guest molecules. As measuring gas, nitrogen was used. Measurements were performed by employees of the Behrens group using the Autosorb-3 by QUANTACHROME INSTRUMENTS and 3Flex instrument from micromeritics. The Autosorb.3 data was further analysed with the model of BRUNAUER, EMMETT and TELLER (BET-Model). The software ASiQwin 2.0 by QUANTACHROME INSTRUMENTS was used. The 3Flex data was analysed with the associated software from micromeritics (Version 5.02). All physisorption isotherms were displayed with the help of the OriginPro 2019 software by OriginLab.

4.1.4 Nuclear Magnetic Resonance Spectroscopy

Nuclear magnetic resonance spectroscopy (short: NMR spectroscopy) is one of the most important analysis methods used in organic chemistry. It can be used to obtain the structure of organic molecules or to be more specific, used to determine the closest chemical environment of certain atoms, as well as their molecular constitution.^[179]

All NMR-investigations were carried out at the Institute of Organic Chemistry of the Leibniz University of Hanover with a BioSpin spectrometer by BRUKER.

The measurements were performed at room temperature at 400 MHz. 10 mg of the sample substance were dissolved in 700 μL DMSO- d_6 and 50 μL D₂SO₄- d_6 and filled into an NMR-tube. The obtained spectra were analysed with the software MestReNova by Mestrelab Research and displayed with OriginPro 2019 software by OriginLab.

4.1.5 Immersion method

As described in section 2.2.4, the immersion method is used to obtain the anisotropic refractive indices (short: RIs) of single crystals. This measuring technique is well established in the field of mineralogy and crystallography.

Immersion measurements were performed at the University of Bremen with a modified Leica DM RXP microscope. The single crystals were mounted onto a glass fiber using red nail polish, which then was attached to the goniometer head. The immersion liquids were purchased from Cargille with RI steps of 0.002 and an accuracy of ± 0.0002 from 1.4-1.7 and with 0.005 steps and ± 0.0005 accuracy from 1.3-1.4 and 1.7-1.8. The known main substances of the immersion liquids are listed down below (Table 6). However, some components are not revealed due to the business secret.

Table 6: Listed main components of the immersion liquids and their RI range.

RI range	Main components
1.300 – 1.395	Perfluorocarbons, Chlorofluorocarbons
1.400 – 1.458	Silicone, Aliphatic and Alicyclic Hydrocarbons
1.460 – 1.570	Aliphatic and Alicyclic Hydrocarbons, Hydrogenated Terphenyl
1.572 – 1.656	Hydrogenated Terphenyl, 1-Bromonaphthalene
1.658 – 1.698	1-Bromo- and 1-Iodonaphthalene
1.700	1-Iodonaphthalene, Sulphur
1.705 – 1.735	Hydrogenated Terphenyl, Diiodomethane
1.740 – 1.780	Diiodomethane, Sulphur
1.785 – 1.800	Diiodomethane, Sulphur, Tin Iodide

All measurements were performed at the University of Bremen in cooperation with Professor Reinhard X. Fischer. For non-cubic single crystals extinction curves were determined prior to the measurement to obtain the crystal positions for RI measurements by using the *excalibrw* software. Pictures were taken with a camera and the software *IC Measure*.

4.1.6 Ellipsometry

Apart from measuring the RI of single crystals, also optical thin films can be measured. However, the precise determination of anisotropic refractive indices is not possible with this method.

Ellipsometry measurements were carried out at the Hanover Center of Optical Technologies (HOT) with a Sentech SE850 from SENTECH by Dr. Emil Agocs. The measuring range was set from 280 nm to 850 nm with 1 mm aperture. The measured data were obtained at incidence angles of 70, 60, 55 and 50 degree. The data was analyzed with the software *CompleteEASE* from Woollam.

4.1.7 Scanning electron microscopy

In order to receive information about the topology of a sample, scanning electron microscopy (SEM) is commonly used for micrometer- to nanometer-sized structures.^[180] Furthermore, energy dispersive X-Ray spectroscopy (EDX) can deliver information on the sample composition, regarding its chemical elements. Samples were prepared using conductive carbon adhesive tape to secure the sample onto the SEM sample holder.

SEM measurements were performed using the field-emission SEM SU-70 from Hitachi by Dr. Jae-Il Kim. Images were modified with the software *ImageJ*. All measurements were performed with 5 kV acceleration voltage and a working distance of 8 mm. Magnifications ranging from 600 to 10.000 were chosen.

4.1.8 Transmission electron microscopy

Structures with sizes in the lower nanometer range or less are difficult to resolve with SEM analysis. Therefore, transmission electron microscopy (TEM) was carried out to receive more detailed information about these structures. All TEM images were performed with a FEI Tecnai F20 by Dr. Jae-Il Kim. Images were modified with the software ImageJ.

4.1.9 Photoluminescence spectroscopy

Photoluminescence measurements were performed by Dr. Jae-Il Kim using a FP-8500 fluorescence spectrometer by JASCO. For a measuring range of 400 to 800 nm an excitation wavelength of 410 nm was selected. Measurements ranging from 350 – 650 nm used an excitation at 365 nm. Photoluminescence quantum yields (PLQYs) were calculated using the software SpectraManager.

4.1.10 60-90 stability testing

In order to test the stability of the perovskite-containing films against higher temperature and high humidity, the as-prepared films were placed into a temperature and humidity chamber TH3-ME by Jeiotech, which was set to 60 °C and 90 % humidity. PLQY measurements were carried out after different exposure times.

4.1.11 High flux testing

To test the stability of different perovskite-containing films, high flux testing was carried out. Therefore, the freshly prepared films were placed into a hönle UV technology LED cube 100 IC and irradiated with high intensity light (460 nm, 240 mW/cm²). PLQY measurements were carried out after different exposure times.

4.2 MOF single crystals syntheses

In order to obtain refractive index (short: RI) data by the immersion method, different MOF single crystals were synthesized. Their syntheses are listed in the following subchapters.

If not further described, all solvothermal reactions were carried out in a 100 mL screw cap borosilicate glass bottle. For weighing, a laboratory scale with an accuracy of ± 1 mg was used. Liquids were measured with standard Eppendorf pipettes. Deionized water with a conductivity less than $0.055 \mu\text{S}/\text{cm}$ was obtained by using the water purification system MicroPure by Thermo Electron GmbH. All chemicals were used without further purifications. All single crystals were immersed in methanol for five days. Each day, the methanol was exchanged against fresh one. Afterwards the single crystals were dried at room temperature for at least three days.

For the ^1H -NMR investigations, 10 mg of the purified MOF single crystals were incubated with the chosen immersion liquid component for three hours. Afterwards the samples were quickly washed twice with ethanol to remove excess components from the MOF surface. Afterwards the samples were dried at room temperature.

Only successful MOF single crystal syntheses are reported in this subchapter, unsuccessful syntheses were left out in order to increase the clarity of this section. Also see Table 5 in subchapter 2.3.

4.2.1 Al-*pydc*

Al-*pydc* MOF single crystals were synthesized according to Wharmby et al.^[68] In brief, 0.375 g of aluminium nitrate nonahydrate were dissolved in 4.5 mL of deionized water and 0.5 mL dimethylformamide (DMF). 0.167 g of 2,6-pyridinedicarboxylic acid (*H₂pydc*) were added and the mixture was placed in a convection oven at 120 °C for 15 h.

4.2.2 Cd-*bzpd*

Cd-*bzpd* MOF single crystals were obtained according to Qin et al.^[69] In brief, 62 mg of cadmium nitrate tetrahydrate were dissolved in 6 mL deionized water. 28 mg of benzophenone-4,4'-dicarboxylic acid (*H₂bzpd*) were added while stirring. Afterwards the mixture was transferred to a 30 mL Teflon-lined steel autoclave and heated in a convection oven to 170 °C for 3 days. The product could only be synthesized successfully once. All other syntheses yielded mixtures of different micro-crystalline phases, that could not further be identified

4.2.3 Zn-*bzpd*

Zn-*bzpd* single crystals were obtained using a synthesis route similar to the above-mentioned Cd-*bzpd* MOF single crystals.^[69] In brief, 60 mg of zinc nitrate hexahydrate and 27 mg of *H₂bzpd* were dissolved under stirring in 6 mL deionized water. The mixture was then transferred to a 30 mL teflon-lined steel autoclave and heated in a convection oven to 170 °C for 3 days.

4.2.4 Hf-*bzpd*

Single crystals of the Hf-*bzpd* MOF were discovered by screening of different synthesis conditions (here: amount of added formic acid).^[70] The ideal, found parameters are given in brief. 0.166 g of hafnium(IV)chloride were dissolved in 20 mL DMF and 2.925 mL formic acid. 0.279 g of *H₂bzpd* were added and the mixture was heated to 120 °C using a convection oven. The solution was kept at 120 °C for 3 days.

4.2.5 Zr-*bzpd*c

As reported by Mohmeyer et al.^[71] 0.167 g of zirconium oxychloride octahydrate were dissolved in 20 mL DMF and 1.95 mL formic acid. 0.279 g of H₂*bzpd*c were added and the reaction mixture was kept for 3 days at 120 °C in a convection oven.

4.2.6 Zr-*bzpd*c with post-synthetic modifications

Zr-*bzpd*c single crystals were obtained by the synthesis procedure described in section 4.2.5. The MOF was purified, as mentioned in subchapter 4.2. The post-synthetic modifications (PSMs) were carried out, as previously reported by Mohmeyer et al.^[72] In this study water, methanol, ethanol, 1-propanol and 1-butanol were used as reactants, already introduced by the author. In addition, benzyl alcohol, 2-propanol, 3-chloro-1-propanol and 3-nitro-1-propanol were newly introduced as well-functioning modification reagents. Unfortunately, 2,2,3,3-tetrafluoropropan-1-ol did not show a full and consistent modification and 3-amino-1-propanol lead to crystal dissolving resulting in a gel-like residue.

50 mg of Zr-*bzpd*c single crystals were incubated in 5 mL of the selected PSM reactant in a quartz glass tube for 16 hours. After the incubation the mixture was purged with argon for 1 hours. The quartz glass tube was sealed and irradiated for 24 hours with UV light using a LED spot lamp by LUMIMAX ($\lambda = 365 \text{ nm}$, 207 W/m^2) within a distance of 4-5 cm. To ensure the homogeneous irradiation of all single crystals and their exposure to the reactant, the quartz glass tubes were placed in the multi-vortexer Multi Reax by Heidolph at 800 rpm. The post-synthetically modified Zr-*bzpd*c single crystals were again purified, as mentioned in subchapter 4.2.

4.2.7 UiO-66

The UiO-66 single crystal synthesis is a modification of the procedure published by Trickett et al.^[62] 54 mg of zirconium tetrachloride ($ZrCl_4$) and 31 mg of terephthalic acid (H_2bdc) were dissolved separately in 6.25 mL of diethylformamide (DEF) each. After mixing both solution, 12.5 mL formic acid were added, as well as 100 μ L of a pre-synthesized UiO-66 seed solution (30 mg of UiO-66 in 6 mL DEF). The dispersion was placed in a convection oven at 135 °C for 7 days. The UiO-66 seeds were synthesized by mixing 48 mg $ZrCl_4$, 12.5 mL DMF, 36 mg H_2bdc and 410 μ L of formic acid. The solvothermal synthesis was then carried out at 120 °C for 24 hours.^[70]

4.2.8 UiO-66-NO₂

UiO-66-NO₂ single crystals were synthesized according to Trickett et al.^[62] with modifications. For this synthesis 54 mg $ZrCl_4$ and 40 mg of 2-nitroterephthalic acid ($H_2bdc-NO_2$) were dissolved separately in each 6.25 mL of DEF. Both solutions were mixed together and 12.5 mL of formic acid and 150 μ L of a pre-synthesized UiO-66-NO₂ seed solution (30 mg of UiO-66-NO₂ in 6 mL DEF) were added. The dispersion was then placed in a convection oven at 135 °C for 7 days. UiO-66-NO₂ seeds were obtained by mixing 48 mg $ZrCl_4$, 12.5 mL DMF, 46 mg $H_2bdc-NO_2$ and 1.01 mL of formic acid. The resulting solution was then was placed in a convection oven at 120 °C for 24 hours.^[70]

4.2.9 UTSA-74

1 g of zinc acetate dihydrate and 0.5 g of benzene-1,2,4,5-tetracarboxylic acid were dissolved in 50 mL of dimethyl sulfoxide (DMSO). The mixture was placed in a 110 °C convection oven and heated for 3 days.

4.2.10 Cs- γ -CD MOF

For the diffusion-controlled crystallization of the γ -CD MOFs the setup, shown in Figure 23, is used. In contrast to the reported literature, the agarose and parafilm sealing of the inner container was substituted by a plastic snap-cap vial lid with punctured holes.

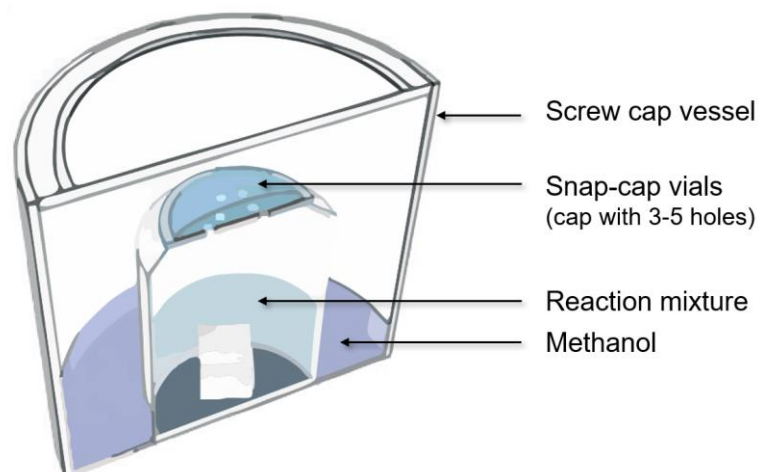


Figure 23: Illustration for the modified diffusion-induced crystallization setup of the γ -CD-MOFs.^[64]

All diffusion-induced crystallizations were carried out at room temperature and took about one to two months until crystals of millimetre size were formed. Cs- γ -CD MOF single crystals were synthesized according to Kim et al.^[64] In brief, 0.269 g of caesium hydroxide and 0.259 g of γ -cyclodextrin (γ -CD) were dissolved in 4 mL of deionized water. The reaction mixture was then transferred into a 10 mL snap-cap glass vial. Three to five holes were put into the cap using a cannula. The vial was then placed into a 1 L screw-cap glass vessel, which was previously filled with 10 mL of fresh methanol. The screw-cap of the vessel was tightened and the crystallization setup was left undisturbed.

4.2.11 K- γ -CD MOF

For the synthesis of the K- γ -CD MOF the setup and procedure from section 4.2.10 was used.^[64] As for the reaction mixture 90 mg of potassium hydroxide and 0.259 g of γ -CD were dissolved in 4 mL deionized water. The rest was carried out as described earlier in section 4.2.10.

4.2.12 Li- γ -CD MOF

The reaction setup and the procedure for the Li- γ -CD MOF synthesis is shown in section 4.2.10. The synthesis was newly investigated and the resulting, ideal parameters are given. 76 mg of lithium hydroxide monohydrate and 0.259 g γ -CD were mixed with 4 mL of deionized water. Apart from lithium hydroxide monohydrate, the unhydrated form (lithium hydroxide) was also tested. Both reactants yielded single crystals, however, the crystals obtained with lithium hydroxide monohydrate were of an overall larger size. Afterwards, the reaction mixture was transferred into a 10 mL snap-cap glass vial. One to two holes were put into the cap using a cannula. The vial was then placed into a large screw-cap glass vessel, which was filled with 10 mL of methanol. The screw-cap of the vessel was tightened and the crystallization setup was left undisturbed.

4.2.13 Rb- γ -CD MOF

The Rb- γ -CD MOF was synthesized using the same setup described in section 4.2.10.^[64] By mixing 0.164 g of rubidium hydroxide and 0.259 g of γ -CD with 4 mL of deionized water, the reaction mixture was created. Further reaction steps were identical to the ones reported in section 4.2.10.

4.2.14 Na- γ -CD MOF

The synthesis of the Na- γ -CD MOF was reported by Forgan et al.^[82] and used an identical setup to the one described in section 4.2.10. In brief, the reaction mixture was prepared by dissolving 64 mg of sodium hydroxide and 0.259 g of γ -CD in 4 mL of deionized water. The rest of the procedure is identical to section 4.2.10.

4.2.15 ZIF-7

ZIF-7 single crystals were synthesized according to Park et al.^[33] In brief, 0.34 g zinc nitrate hexahydrate and 0.1 g benzimidazole (HbIm) were dissolved in 3 mL of DMF. For this synthesis a programmable oven was used. The oven was heated with a rate of 5 °C/min to 130 °C. The temperature was held for 48 h and finally cold down to room temperature with a rate of 0.4 °C/min. The product could only be obtained successfully once.

4.2.16 ZIF-8

Single crystals of ZIF-8 were synthesized according to Lee et al.^[89] In brief, 0.67 g zinc nitrate hexahydrate, 0.167 g of 2-methylimidazole were mixed with 50 mL of DMF. The resulting solution was heated to 140 °C for 24 hours.

4.2.17 ZIF-68

ZIF-68 single crystals were obtained according to Banerjee et al.^[88] 0.268 g zinc nitrate hexahydrate were dissolved in 5 mL DMF (solution A) and separately dissolving 0.204 g 2-nitroimidazole (HnIm) and 0.213 g of HbIm in 10 mL DMF (solution B). Solution A was then added dropwise into solution B under stirring. After stirring for an additional 20 min the reaction mixture was heated to 85 °C for 52 hours.

4.2.18 ZIF-69

ZIF-69 single crystals were synthesized according to Banerjee et al.^[88] In brief, 0.178 g of zinc nitrate hexahydrate, 0.136 g of HnIm and 0.183 g of 5-chlorobenzimidazole were dissolved in 12 mL of DMF. The solution was then heated for 3 days at 100 °C in a convection oven.

4.2.19 ZIF-70

Single crystals of ZIF-70 were synthesized according to Banerjee et al.^[88] In brief, three separate solutions were created. Solution A contains 0.4 g of zinc nitrate hexahydrate in 2 mL of DMF, solution B contains 92 mg of imidazole, 0.144 g of HnIm in 2 mL DMF and solution C consists of simply 6.8 mL of pure DMF. Solution B and A were dissolved using an ultrasonic bath. Then solution B was added to solution A and afterwards solution C was added. The resulting mixture was placed in an ultrasonic bath for two to three minutes and then transferred into a 110 °C vacuum oven and kept there for 4 days.

4.2.20 ZIF-78

ZIF-78 single crystals were synthesized according to Banerjee et al.^[88] In brief, 0.238 g zinc nitrate hexahydrate were dissolved in 4 mL DMF (solution A). Separately, 0.113 g HnIm (solution B) and 0.163 g 5-nitrobenzimidazole (solution C) were dissolved in each 5 mL of DMF. Then solution B and C were mixed and added to solution A. The obtained mixture was then heated to 100 °C and kept for 4 days at that temperature.

4.2.21 ZIF-81

Single crystals of ZIF-81 were synthesized according to Banerjee et al.^[88] In brief, three separate solutions need to be prepared. Solution A contains 0.238 g of zinc nitrate hexahydrate dissolved in 4 mL of DMF. Solution B contains 0.113 g of HnIm and 5 mL DMF and solution C was created by mixing 0.197 g of 5-bromobenzimidazole with 5 mL of DMF. Solution B and C were mixed and then solution A was added. The solvothermal reaction time were 4 days at 100 °C.

4.2.22 ZIF-82

The synthesis of ZIF-82 single crystals was carried according to Banerjee et al.^[88] In brief, three different solutions were created and then mixing them and heating them to 100 °C for 4 days. Solution A was obtained by mixing 0.238 g zinc nitrate hexahydrate with 4 mL DMF. 0.133 g HnIm (solution B) and 93 mg of 5-cyanoimidazole (solution C) were each dissolved separately in 5 mL DMF. Then the solutions B and C were mixed and solution A was added. The resulting mixture was heated as mentioned earlier.

4.2.23 ZIF-90

Single crystals of ZIF-90 could be obtained using a modified procedure of the one reported by Morris et al.^[91]. The initially reported method did not yield single crystals, therefore the optimal synthesis parameters were determined as follows. 57 mg of zinc nitrate hexahydrate and 83 mg of Imidazole-2-carboxyaldehyde were dissolved in 3 mL of DMF. The solution was then heated to 80 °C for 36 hours.

4.3 Perovskite-Ce-MOF materials

This subchapter contains the reproduction and modification of the Ce(IV)*bdc* MOF-perovskite-SiO₂ material introduced by Ren et al. in 2022.^[29]

4.3.1 Ce-MOF syntheses

For the Ce(IV)-MOF 1 g of Pluronic F-127, 4.494 g of sodium perchlorate monohydrate and 2.4 mL of acetic acid were dissolved in 48 mL of deionized water at 50 °C. Afterwards, 4.388 g of cerium(IV) ammonium nitrate and 1.33 g of terephthalic acid were added and the mixture was stirred at 70 °C for 20 min. Then the product was collected by centrifugation (3 min at 8000 rpm) and washed three times with water, twice with dimethylformamide, and once with ethanol. After each washing step the powder was collected by centrifugation (3 min at 8000 rpm) and the solvent was exchanged. The Ce-MOF was soaked in ethanol over night at 50 °C in a convection oven and dried overnight at 50 °C in the vacuum oven.

4.3.2 Perovskite confinement after Ren et al.^[29]

9.175 g of lead(II)bromide were dissolved in 0.25 mL of oleic acid, 0.25 mL of oleylamine and 50 mL of DMF at 80 °C. Then, 1 g of Ce-*bdc* MOF were added and stirred for 6 h at room temperature under vacuum. The powder was afterwards collected via centrifugation (3 min at 5000 rpm) and redispersed in 50 mL of toluene. Separately, 1.06 g of caesium bromide were dissolved in 50 mL of methanol at 60 °C. The so-formed solution was added to the Ce-MOF toluene dispersion under stirring for two minutes. After that the MOF-perovskite material was collected by centrifugation (3 min at 5000 rpm) and redispersed in 50 mL of toluene. After carrying out the silica shell synthesis described in section 4.3.4, this sample will be referred to as sample S1.

4.3.3 Perovskite confinement after Wu et al.^[181]

12.23 g of lead(II)bromide were dissolved in 667 mL of DMF at 60 °C. Then, 1 g of Ce-*bdc* MOF were added and immersed for 1 h at 60 °C. The powder was afterwards collected via centrifugation (3 min at 8000 rpm) and washed with DMF and ethanol. The powder was air dried afterwards. Separately, 7.09 g of caesium bromide were dissolved in 333 mL of methanol. The so-formed solution was added to the treated Ce-MOF. After 24 h the MOF-perovskite material was collected by centrifugation (3 min at 8000 rpm) washed with ethanol and air dried afterwards. After carrying out the silica shell synthesis described in section 4.3.4, this sample will be referred to as sample S3.

4.3.4 Perovskite-Ce-MOF with SiO₂-shell synthesis

2.5 mL of TMOS (Tetramethyl orthosilicate) were added to the obtained dispersion from section 4.3.2. The mixture was stirred at room temperature and under air for 4 h, to allow the hydrolysis of TMOS. The product was collected and dried in a vacuum oven at 50 °C over night.

4.3.5 Film fabrication

Different amounts of the MOF (0.4 g and 0.2 g) were each mixed with 3.8 g of a special, premanufactured SNU-polymer especially designed for film fabrication. For mixing a blade homogenizer by LK Lab Korea was used. Afterwards a film of the homogenized mixture with approximately 75 µm thickness was created between two barrier films (TBF1004, i-components). The resin was then cured for 6 min using a 36 W UV Lamp (nail hardening device). Each film was cut into several pieces for high-flux (section 4.1.9) and 60-90 (60 °C, 90 % humidity, section 4.1.10) testing.

5 Results and Discussion

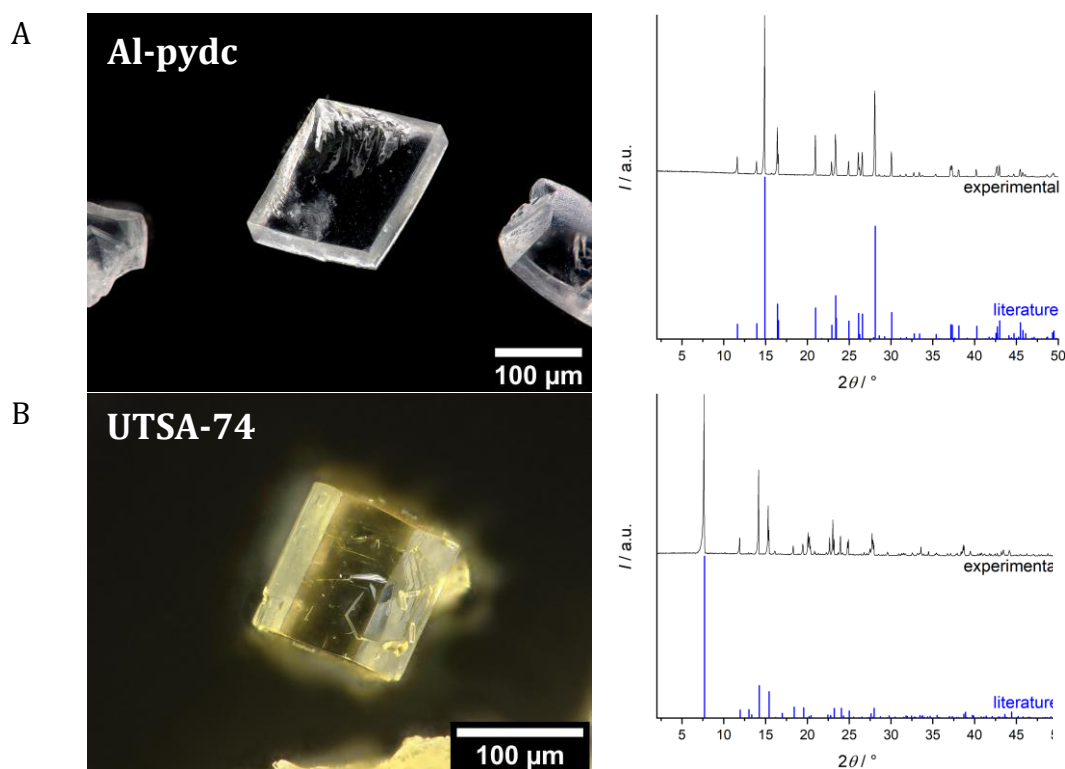
Within this thesis the results are presented in five main subchapters. The first subchapters, including 5.1 to 5.3, will discuss the results regarding different MOF single crystal synthesis and their refractive index (short: RI) measurements. The following subchapters, including 5.4 and 5.5 focus on the creation of MOF-perovskite materials, their characterization and stability testing.

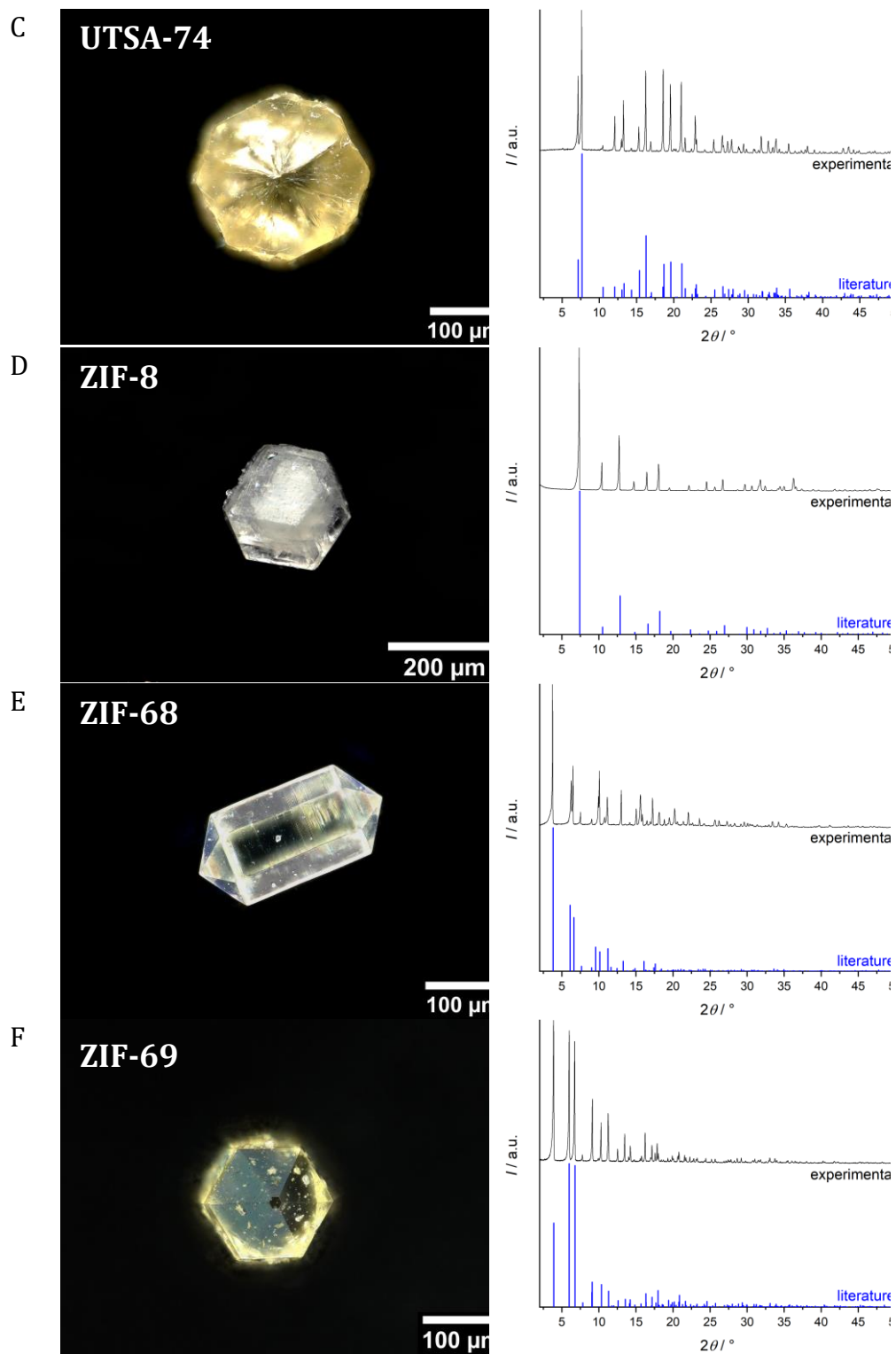
5.1 MOF single crystals

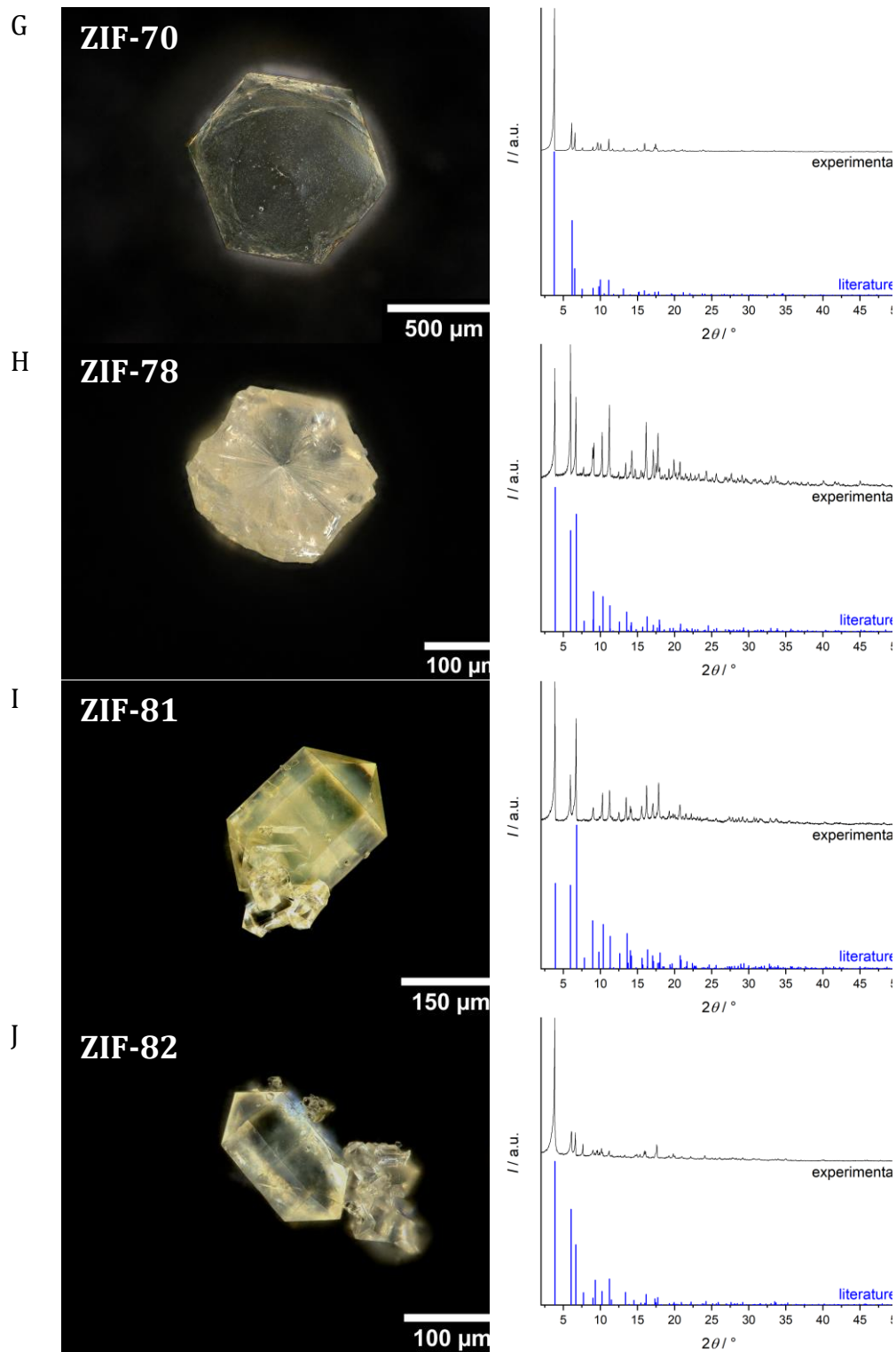
This subchapter contains information regarding the outcomes of different MOF single crystal syntheses. In order to secure a successful reproduction, XRD and digital optical microscopy measurements were performed and evaluated. Only successful MOF crystal syntheses are described here.

5.1.1 Successful single crystal syntheses based on literature

The following Figure 24 provides an overview of single crystal syntheses directly adapted literature without any further modification. The obtained results match the literature ones, so that no detailed, further discussion is needed.







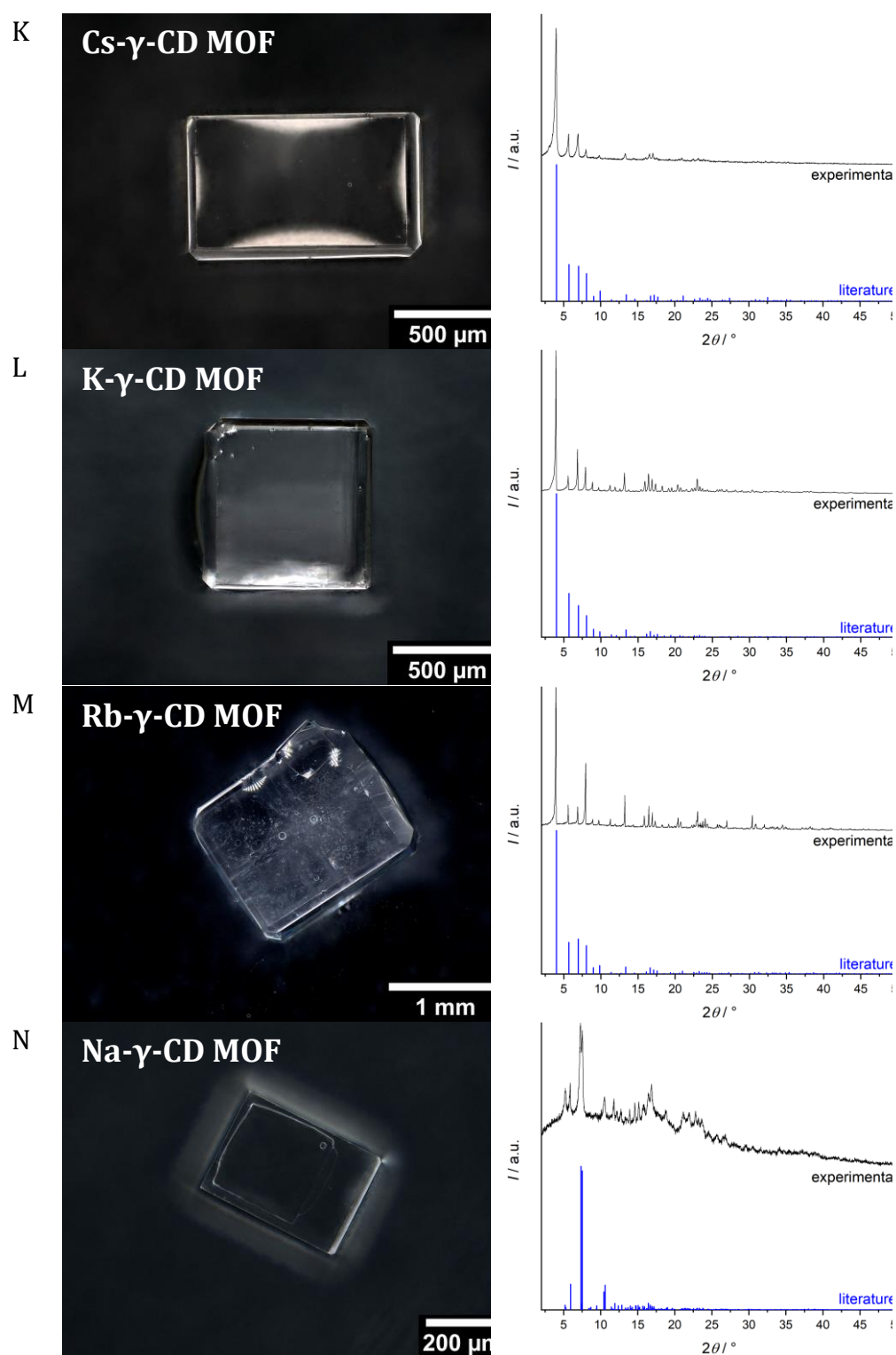


Figure 24: Obtained digital optical microscope images and XRD patterns of MOF single crystals compared to literature. A: Al-*pydc*, XRD literature^[68]; B: UTSA-74, XRD literature^[77]; C: ZIF-7, XRD literature^[33]; D: ZIF-8, XRD literature^[89]; E: ZIF-68, XRD literature^[88]; F: for ZIF-69, XRD literature^[88]; G: ZIF-70, XRD literature^[88]; H: ZIF-78, XRD literature^[88]; I: ZIF-81, XRD literature^[88]; J: ZIF-82, XRD literature^[88]; K: Cs- γ -CD MOF, XRD literature^[64]; L: K- γ -CD MOF, XRD literature^[64]; M: Rb- γ -CD MOF, XRD literature^[64]; N: Na- γ -CD MOF, XRD literature^[82].

Al-pydc MOF single crystals were successfully synthesized according to Wharmby et al.^[68] Figure 24 A shows matching XRD data and an image of the obtained single crystals. The displayed single crystal topology is an oblique rectangular prism. The collected XRD data of the UTSA-74 MOF matches the literature well (Figure 24 B). Moreover, single crystals with sizes between 100 and 200 μm , showing a hexagonal prismatic shape, could be synthesized. The ZIF-7 single crystals show an octagonal prismatic shape (Figure 24 C) and their obtained diffraction pattern matches the one reported in literature. Thereby, the reproduction of the ZIF-7 single crystals can be considered a success. The ZIF-8 single crystals exhibit the typical cuboctahedron-shape. In addition, both literature data and measured data contain identical reflex positions and similar intensities (Figure 24 D). The single crystals of ZIF-68 exhibit a hexagonal bipyramidal prismatic shape, which is typical for these gmelinite type ZIF frameworks (Figure 24 E). In addition, the well matched XRD data of the experiment with the literature indicates a successful reproduction of the single crystals. Single crystals of ZIF-69 possess a hexagonal bipyramidal prismatic shape (Figure 24 F). Apart from the matching crystal shape, the obtained diffraction pattern also matches the literature. The obtained diffraction pattern of ZIF-70 agrees well with the literature (Figure 24 G). In addition, the synthesized single crystals exhibit the typical hexagonal bipyramidal prismatic shape (Figure 24 G). Like the previous single crystals, ZIF-78 single crystals exhibit hexagonal bipyramidal prismatic shapes, as well (Figure 24 H). Literature and experimental XRD patterns also match quite well. ZIF-81 single crystals possess the typical hexagonal bipyramidal prismatic topology of these gmelinite type ZIFs (Figure 24 I). In addition, the reflex positions of the experimental data match the literature very well. The gained diffraction pattern of the ZIF-82 fits the literature (Figure 24 J). In addition, the synthesized single crystals exhibit the hexagonal prismatic shape. The measured diffraction pattern of the Cs- γ -CD MOF is highly similar to literature one (Figure 24 K). The millimetre-sized single crystals show a cubic shape. Crystals this large cannot always fit the measurement cell therefore these single crystals were forcefully cracked, so that a smaller crystal fragment could be measured. Similar to the Cs- γ -

CD MOF, the K- γ -CD MOF also yields cubic shaped single crystals in the millimetre range (Figure 24 L). The obtained XRD pattern further proves that the synthesis of the K- γ -CD MOF was successful, as it matches well with the literature. The single crystals of the Rb- γ -CD MOF exhibit a cubic shape. The measured XRD pattern corresponds well with the literature data. The crystal shape of the Na- γ -CD MOF is similar to the previous discussed γ -CD MOFs (Figure 24 N). Also, the obtained XRD data matches with the literature. The high background noise is caused by the aging process of the crystals. Under ambient conditions the crystal turns into an amorphous solid over time.

5.1.2 Unusual shaped single crystals

The following Figure 25 provides an overview of single crystal syntheses directly taken from literature without any further modification. The obtained results mostly match the literature ones. Nevertheless, the synthesized single crystals can still be used for the immersion method and can be considered a successful reproduction.

Schistose-like Cd-*bzpd*c MOF single crystals (Figure 25 A) were obtained with the same crystal morphology, as described in the literature.^[69] Their single crystallinity was further checked with polarization microscopy and confirmed to be sufficient. The XRD pattern furthermore matched the one observed by Qin et al.^[69] Cd-*bzpd*c was successfully reproduced. Due to the crystal morphology the intensities of the (100) and (200) reflections are diminished. Zn-*bzpd*c single crystals were obtained in a similar manner to the Cd-*bzpd*c MOF single crystals. As well as for Cd-*bzpd*c single crystals, their morphology is schistous (Figure 25 B). Their single crystallinity was also confirmed with polarization microscopy. The collected XRD pattern also matched the literature.^[69] The intensities of the (100) and (200) reflections are diminished for the Zn-*bzpd*c due to the crystal morphology.

The Zr-*bzpd*c single crystals exhibit the rhombus shape. In addition, the matching XRD patterns indicate that the synthesized MOF is indeed the Zr-*bzpd*c MOF (Figure 25 C). However, the small-angled corners are rounded and not as sharp as observed by Mohmeyer et al. Nevertheless, the XRD pattern and the shape only exhibits slight deviations, the synthesis can be considered a success.

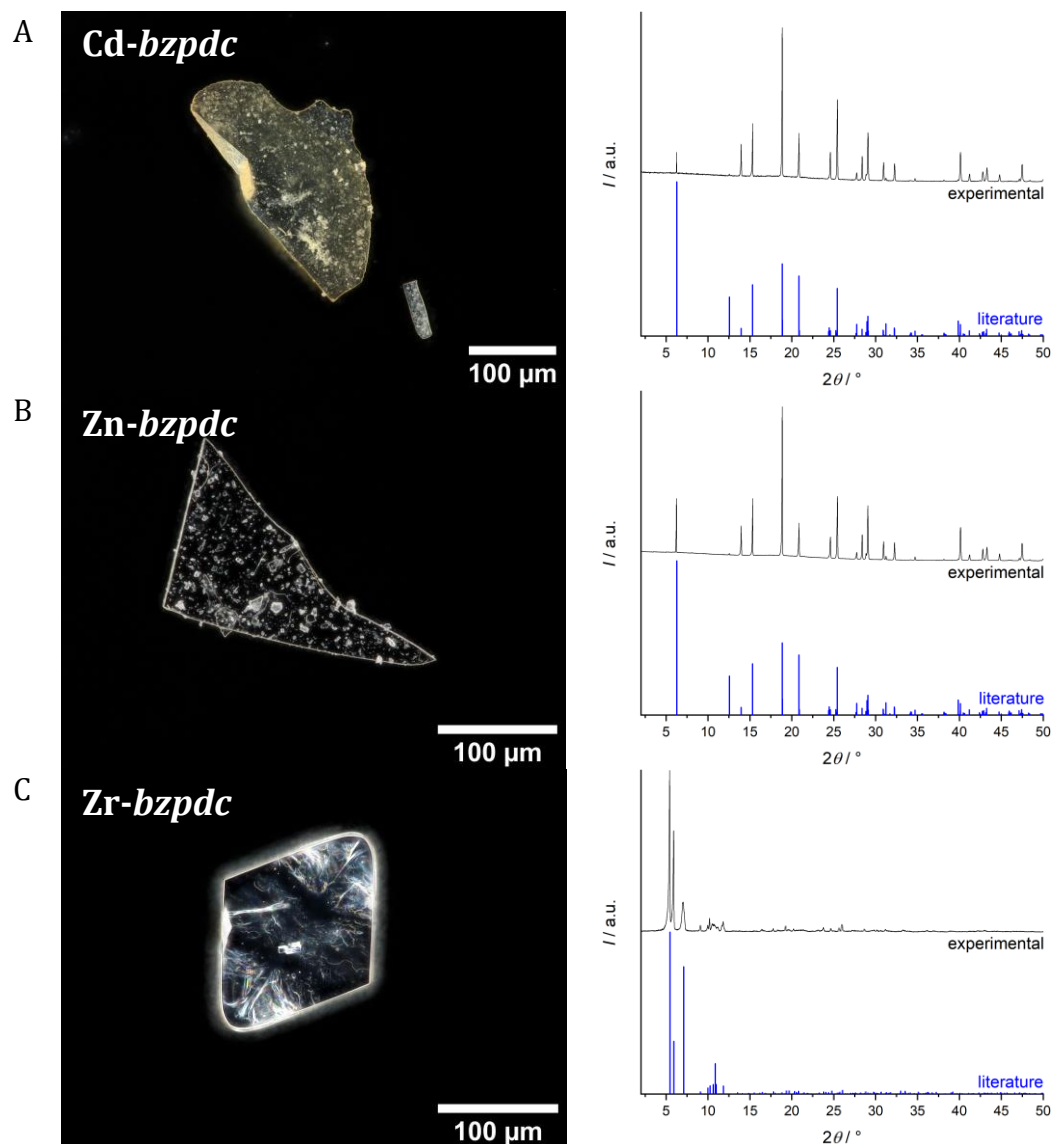
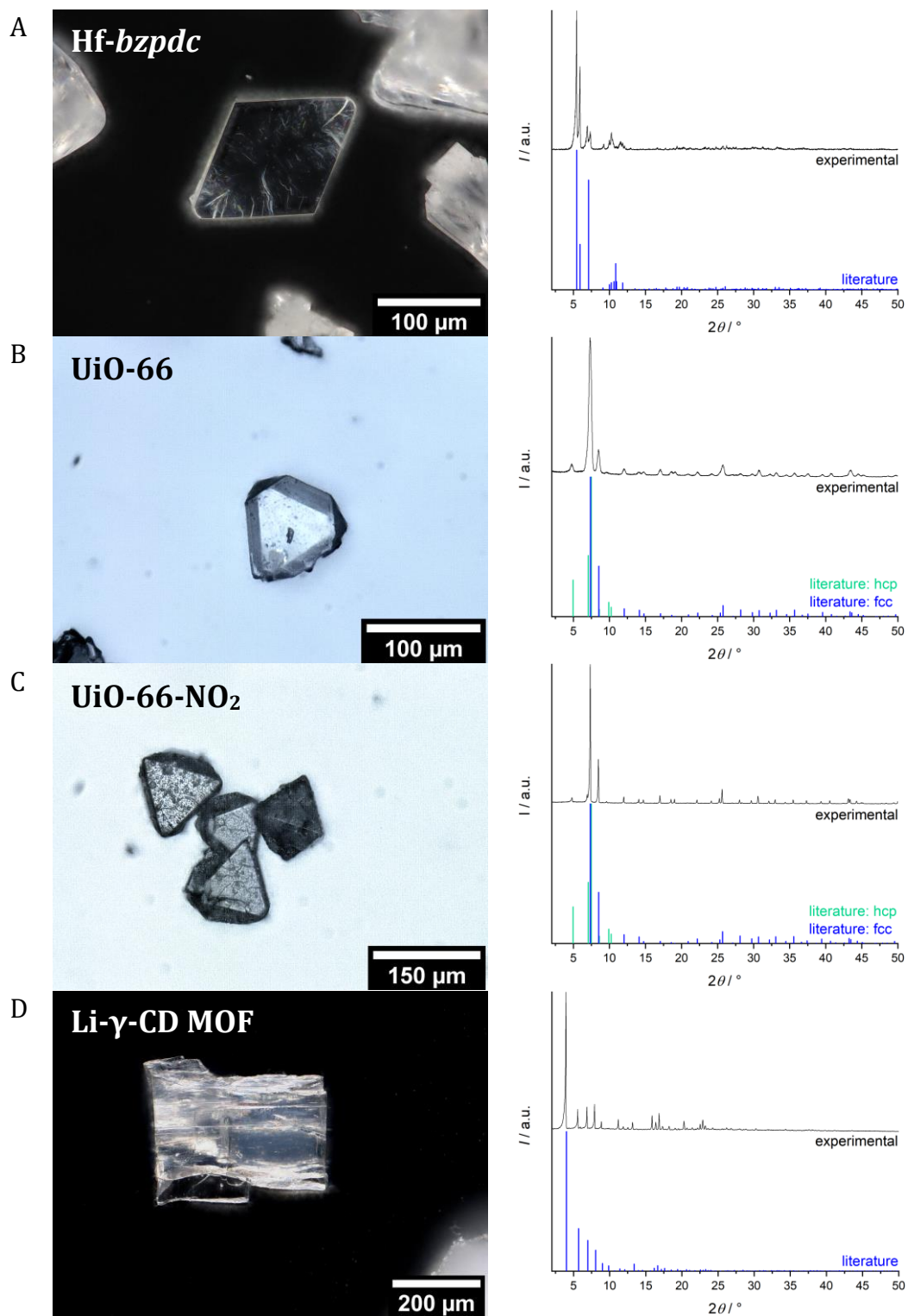


Figure 25: Obtained digital optical microscope images and XRD patterns of MOF single crystals compared to literature. A: Cd-*bzpd*, XRD literature^[69]; B: Zn-*bzpd*, XRD literature^[69]; C: Zr-*bzpd*, XRD literature^[71].

5.1.3 Modified literature syntheses routes

The following Figure 26 shows single crystals synthesized via modified syntheses routes. All synthesized single crystals were later used for immersion measurements.



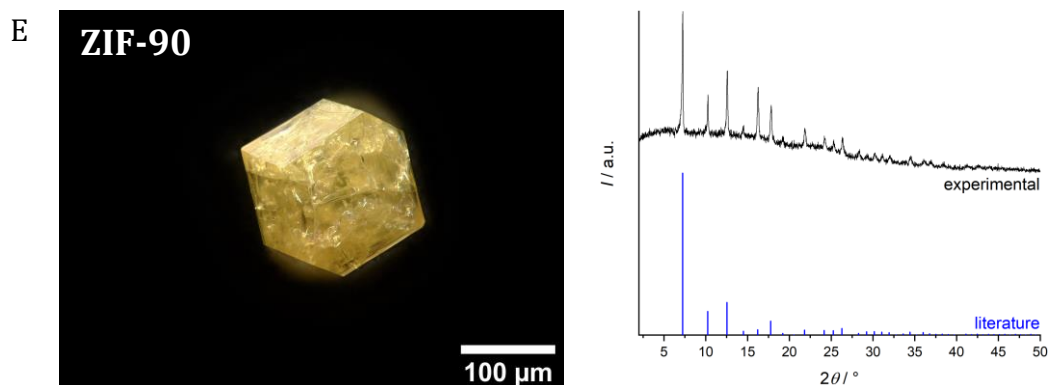


Figure 26: Obtained digital optical microscope images and XRD patterns of MOF single crystals compared to literature. A: Hf-*bzpd*c, XRD literature^[71]; B: UiO-66, XRD literature^[62,70,182]; C: UiO-66-NO₂, XRD literature^[62,70,182]; D: Li- γ -CD MOF, XRD literature^[64]; E: ZIF-90, XRD literature^[91].

Hf-*bzpd*c single crystals exhibit the typical rhombus shape (Figure 26 A). The measured XRD pattern corresponds to the literature. Therefore, the Hf-*bzpd*c MOF could be obtained.^[70] Apart from cubic UiO-66, hexagonal UiO-66 was found to be a side product (Figure 26 B). However, the hexagonal phase did not interfere with the cubic one and could be clearly distinguished by optical microscopy according to their shape (octahedral crystals for cubic UiO-66 see Figure 26 B).^[62,70] As already observed for the UiO-66, the hexagonal phase could be identified for UiO-66-NO₂ as well (Figure 26 C). However, the amount of the formed side product is much smaller here. UiO-66-NO₂ single crystals also possess an octahedral crystal shape. The Li- γ -CD MOF exhibiting the cubic crystal shape, as well. However, in general the obtained crystals were slightly smaller than other γ -CD MOFs. Apart from the deviating size, the XRD pattern matches well with the literature data (Figure 26 D). Like the sodalite type ZIF-8 single crystals, ZIF-90 single crystals exhibit the typical cuboctahedron shape, as well (Figure 26 E). Literature and experimental XRD patterns also match very well.

5.1.4 Zr-*bzpd*c with post-synthetic modifications

As already investigated by Mohmeyer et al.^[71,72,94] Zr-*bzpd*c single crystals were modified with different reagents. In this study water, methanol, ethanol, 1-propanol and 1-butanol were used as reactants, already introduced by these authors. In addition, benzyl alcohol, 2-propanol and 3-chloro-1-propanol were chosen in this work. The physisorption measurements show the drastic decrease of the pore volume (Figure 27) which proves the successful addition of the reactant to the linker molecules.

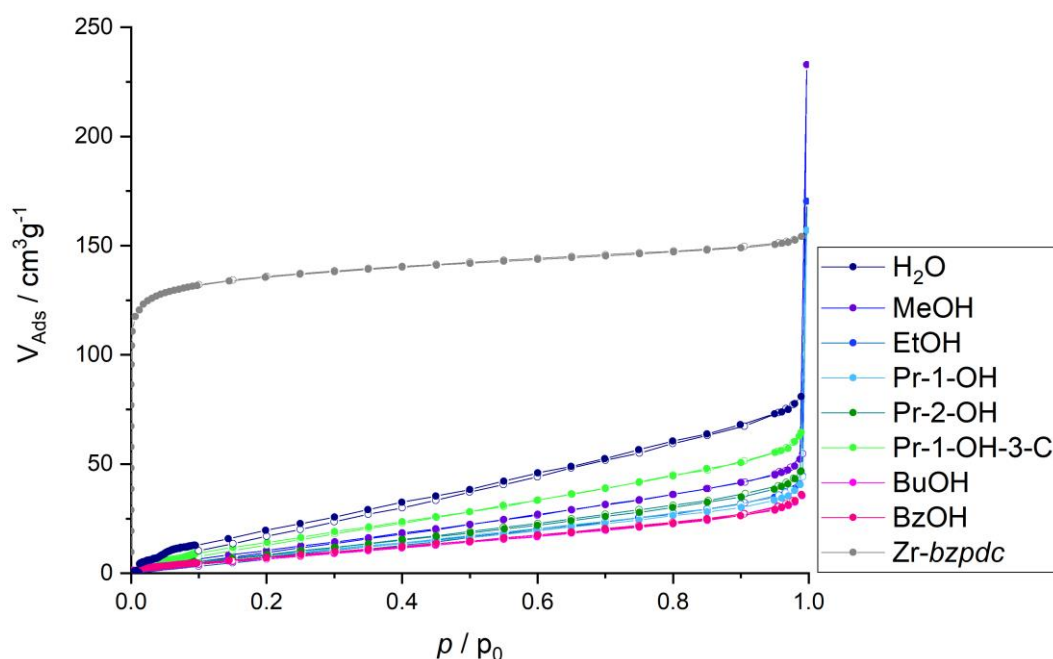


Figure 27: Physisorption data from post-synthetically modified Zr-*bzpd*c single crystals (next to the graph the modification reagents are listed).

XRD measurements (Appendix Figure 3) furthermore confirm the successful reproduction, which according to Mohmeyer et al. can be seen by the shift of the main reflex towards larger angles.

5.2 Refractive index measurements of MOF single crystals

All RI immersion measurements were performed at 589 nm with an error of ± 0.0032 . Above 1.7 and below 1.4 the error increased to ± 0.008 . Follow-up investigations regarding the entering of immersion liquids into the MOF frameworks and thereby the reliability of the obtained results are displayed in subchapter 5.3. All immersion measurements were obtained in cooperation with Professor Reinhard X. Fischer's group at the University of Bremen.

5.2.1 *bzpd*-MOF single crystals

In Table 7 the obtained immersion measurement results are listed. Table 7 a) compares the RIs of the Cd- and the Zn-*bzpd* MOF. Both MOFs possess the same framework structure and show a fivefold coordination of the metal ion.^[183] The values for a sixfold coordination were compared, since there was no dynamic polarizability data provided for fivefold coordinated Cd²⁺. Cd-*bzpd* (Cd²⁺: 2.70 Å³) should thereby possess an overall higher RI than Zn-*bzpd* (Zn²⁺: 1.70 Å³), due to the dynamic polarizability being directly proportional to the RI.^[49] This is also in agreement with the immersion measurement results (Table 7). Zn-*bzpd*'s mean RI of 1.667 is lower than the one of Cd-*bzpd* (>1.694).^[49]

Table 7: RI immersion measurements of different *bzpd*-MOFs.

	MOF	RI _{measured}		
a)	Cd- <i>bzpd</i>	$n_x = 1.524$	$n_y > 1.8$	$n_z = 1.7575$
	Zn- <i>bzpd</i>	$n_x = 1.760$	$n_y = 1.640$	$n_z = 1.602$
b)	Hf- <i>bzpd</i>	$n_x = 1.658$	$n_y = 1.578$	$n_z = 1.590$
	Zr- <i>bzpd</i>	$n_x = 1.680$	$n_y = 1.580$	$n_z = 1.604$

Zr-*bzpd* and Hf-*bzpd* each exhibit eightfold coordination.^[71,184] Once comparing the dynamic polarizability of octahedrally coordinated Zr⁴⁺ (3.74 Å³) and Hf⁴⁺ (3.10 Å³) Zr-*bzpd* should possess an overall higher RI than Hf-*bzpd*. This matches with the results of the immersion measurements (Table 7 b)), where Zr-*bzpd* exhibits an overall higher mean RI of 1.621 in comparison to Hf-*bzpd* (1.609).

5.2.2 γ -CD MOF

Table 8 a) lists the RIs of the γ -CD MOFs with the cubic crystal system. the dynamic polarizability increases from Li^+ (0.15 \AA^3) to K^+ (1.4 \AA^3) to Rb^+ (2.02 \AA^3) to Cs^+ (3.5 \AA^3), which also correlates with the measured RI values.^[49] Considering the different crystal systems between the Na- γ -CD MOF (Table 8 b)) and the other γ -CD MOFs, the values cannot be directly compared.

Table 8: Refractive index immersion measurements of different γ -CD MOFs.

MOF		RI _{measured}		
a)	Li- γ -CD MOF	1.515		
	K- γ -CD MOF	1.518		
	Rb- γ -CD MOF	1.520		
	Cs- γ -CD MOF	1.525		
b)	Na- γ -CD MOF	$n_x = 1.510$	$n_y = 1.515$	$n_z = 1.514$

Due to the large size of these single crystals it was possible to confirm the immersion measured RIs by ellipsometry measurements (Table 9). However, the quality of the ellipsometry results was poor (MSEs around 24; subchapter 8.4). Therefore the obtained results can only be used for a brief confirmation of the overall RI-range of these single crystals. Indeed, they were able to prove that the γ -CD MOFs exhibit RIs around 1.5. In addition, they also affirm the RI increase from the Rb- γ -CD to the Cs- γ -CD MOF (Table 9 a)).

Table 9: Comparison of different refractive index measurements for γ -CD MOFs.^[185]

MOF		<RI _{immersion} >	RI _{ellipsometry}
a)	Li- γ -CD MOF	1.515	-
	K- γ -CD MOF	1.518	-
	Rb- γ -CD MOF	1.520	1.49
	Cs- γ -CD MOF	1.525	1.51
b)	Na- γ -CD MOF	1.513	1.48

5.2.3 ZIF single crystals

Table 10 contains the measured RI data of the synthesized ZIF single crystals, sorted by their crystal system and topology. Organic compound atomic refraction values were investigated by Vogel et al.^[186]. When comparing the values of a methyl group (5.68 cm³) and a carbaldehyde group (5.74 cm³) a small RI increase is observed, once a methyl group is substituted with a carbaldehyde group. This tendency can also be observed by the RI data in Table 10 b). However, for the gmelinite type ZIFs the observed trend (RI: ZIF-70 > ZIF-78 > ZIF-81 > ZIF-68 > ZIF-82 > ZIF-69; Table 10 c)) does not match with the theoretical trend that should be observed (RI: ZIF-81 > ZIF-78 > ZIF-69 > ZIF-68 > ZIF-82 > ZIF-70) according to literature.^[50,51,53]

Table 10: Refractive index immersion measurements of different *bzpd*c-MOFs.

MOF		RI _{measured}		
a)	ZIF-7	$n_x = 1.628$	$n_y = 1.639$	$n_z = 1.654$
b)	ZIF-8	1.533		
	ZIF-90	1.588		
c)	ZIF-68	$n_e = 1.544$	$n_o = 1.551$	
	ZIF-69	$n_e = 1.547$	$n_o = 1.524$	
	ZIF-70	$n_e = 1.624$	$n_o = 1.598$	
	ZIF-78	$n_e = 1.587$	$n_o = 1.616$	
	ZIF-81	$n_e = 1.603$	$n_o = 1.569$	
	ZIF-82	$n_e = 1.536$	$n_o = 1.546$	

Because the RI values of the ZIF single crystals are very high compared to previous reported values^[40,187] and the overall tendency for gmelinite type ZIFs is not confirmed, ¹H-NMR investigations were carried out to investigate whether the immersion liquid is able to enter the microporous MOF structure or not.

5.2.4 Other single crystals

Apart from the above-mentioned MOFs, also single crystals of UiO-66, UiO-66-NO₂, Al-*pydc* and UTSA-74 were measured (Table 11). The Al-*pydc* possesses the highest RI change within the measured MOF single crystals. Simply by changing the orientation of an Al-*pydc* single crystal an RI change of up to 0.2565 can be observed (Table 11 a)). When comparing the atomic refraction values of a nitro group (6.713 cm³) and a hydrogen atom (1.03 cm³) a RI increase is indicated, once a hydrogen atom is substituted by an additional nitro-group.^[186] This has already been observed by Yin et al.^[45] and can also be observed by the increase of the RI values from UiO-66 to UiO-66-NO₂ (Table 11 c)).

Table 11: Refractive index immersion measurements of different MOF single crystals.

	MOF	RI _{measured}		
a)	Al- <i>pydc</i>	$n_x = 1.7025$	$n_y = 1.446$	$n_z = 1.684$
b)	UTSA-74	$n_e = 1.651$	$n_o = 1.542$	
c)	UiO-66	1.574		
	UiO-66-NO ₂	1.594		

5.2.5 Zr-*bzpd*c-MOF PSM single crystals

In order to determine the exact measurement positions for the immersion method, an extinction curve needs to be measured first. For the PSM modified Zr-*bzpd*c single crystals the determination of each maximal extinction point became difficult since the degree of single crystallinity was reduced most likely due to the PSM treatment. Figure 28 shows a comparison between the point of maximal extinction observed for an unmodified Zr-*bzpd*c single crystals (Figure 28 Left) that clearly shows single crystallinity to a PSM modified one (Figure 28 Right) where no full extinction could be obtained. This further indicated, that during the PSM treatment the single crystallinity of Zr-*bzpd*c single crystals is diminished. Since total extinction (Appendix Figure 1, right) could not be achieved the point of maximum partial extinction was selected instead. Some examples of these maximum partial extinctions are given in Figure 28.

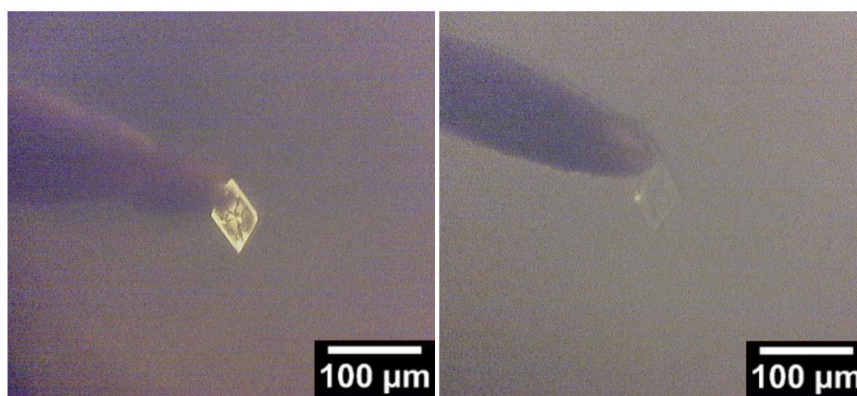


Figure 28: Pictures of two *Zr-bzpdC* single crystals during the extinction curve measurement at the point of their maximum extinction; Left: PSM with Propane-2-ol, Right: unmodified *Zr-bzpdC*.

In addition, due to the reduced degree of single crystallinity, the determined measurement positions were not consistent, even though the crystals came from the same batch. This was most likely caused by the loss of single crystallinity, too. Therefore, all measurements in this subchapter were carried out with regard to the measurement positions of the unmodified *Zr-bzpdC* single crystal and thus will be referred to as geometric RI immersion measurements. As a result, the overall accuracy decreases and the measurement error was set to ± 0.0052 . Furthermore, the PSM reaction mechanism is not yet proven. Apart from the proposed mechanism by Mohmeyer et al. (Figure 12) other reaction paths (Figure 29) are possible and most likely are responsible for the reduced single crystallinity.

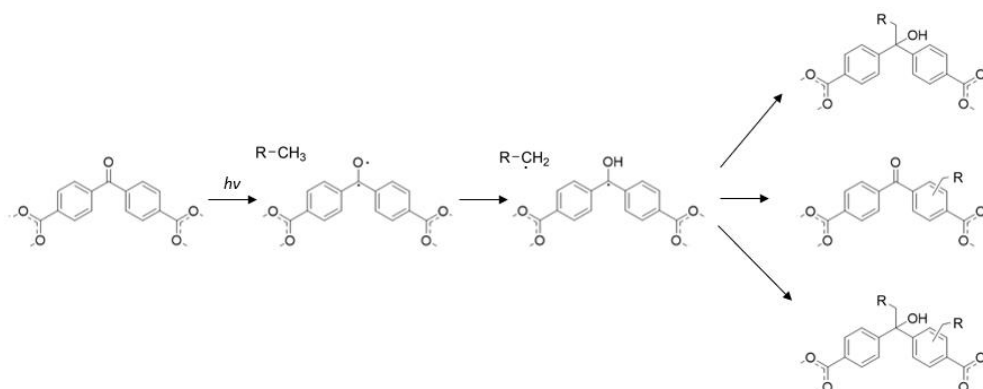


Figure 29: Suggested mechanisms for the occurring PSM reaction taking place at the *bzpdC* linker molecule. The mechanisms were taken from literature^[71,72,94] and displayed using Chemdraw software.

Table 12 lists all the measurement results from the PSM *Zr-bzpd*c single crystals. On the one hand different chain length of alcohols were investigated (Table 12 a)). On the other hand, different functional groups were added to propane and different positions for the hydroxy group were studied (Table 12 b)). If the chain length of the PSM reagent increases, the mean RI should gradually increase as well. However, a gradual increase is only observed for water, since the RI of samples modified with methanol and ethanol increasingly decreases to a minimum of 1.612. Afterwards the RI almost gradually increases with the exception of butan-1-ol. The largest RI increase could be obtained by choosing water or benzyl alcohol as PSM reagent. The lowest mean RI could be measured for the ethanol modified *Zr-bzpd*c single crystals. Nevertheless, the mean RIs are all very close and stay within deviations of ± 0.009 or less. With the exception of water, n_x notably decreased for all modified samples. The ethanol modified *Zr-bzpd*c possesses the lowest n_x of all measured *Zr-bzpd*c PSM single crystals. This decrease is accompanied by an increase of n_y (Table 12). Here, the benzyl alcohol modified sample shows the largest increase. For n_z no particular trend is visible apart from the modifications with water showing the highest decrease and with benzyl alcohol showing the highest increase.

Table 12: RI 'geometric' immersion measurements of different *bzpd*c-MOFs (the value for propan-1-ol was listed twice to improve the clarity of section b)).

PSM reagent		RI _{measured}		
	None (as syn.)	$n_x = 1.680$	$n_y = 1.580$	$n_z = 1.604$
a)	Water	$n_x = 1.682$	$n_y = 1.612$	$n_z = 1.588$
	Methanol	$n_x = 1.643$	$n_y = 1.620$	$n_z = 1.607$
	Ethanol	$n_x = 1.634$	$n_y = 1.606$	$n_z = 1.596$
	Propan-1-ol	$n_x = 1.644$	$n_y = 1.610$	$n_z = 1.598$
	Butan-1-ol	$n_x = 1.645$	$n_y = 1.609$	$n_z = 1.596$
	Benzyl alcohol	$n_x = 1.649$	$n_y = 1.622$	$n_z = 1.612$
b)	Propan-1-ol	$n_x = 1.644$	$n_y = 1.610$	$n_z = 1.598$
	Propan-2-ol	$n_x = 1.664$	$n_y = 1.614$	$n_z = 1.600$
	Propan-1-ol-3-chloride	$n_x = 1.650$	$n_y = 1.602$	$n_z = 1.598$

Looking into the different functional groups attached to propane, the mean RI of the Zr-*bzpd*c single crystals with propan-1-ol and propan-1-ol-3-chloride modification are the same, though the propan-2-ol treatment shows an increased mean RI value. However, the results for propan-1-ol and propane-2-ol modification should be the same due to their identical composition, followed by an increase when modified with propan-1-ol-3-chloride. Further trends observed are a gradual increase of the n_x values from propan-1-ol over propan-1-ol-3-chloride to propan-2-ol treatment. At the same time a decrease in the n_y value can also be observed. The measured RI decreases from propan-2-ol over propan-1-ol to propan-1-ol-3-chloride modification. The n_z values are similar (Table 12 b)).

Since the single crystallinity is diminished by the PSM treatment, the measurement results are only intended for the readers interest.

5.3 NMR investigations of MOF single crystals

In order to simplify the experiments, NMR investigations for 1-Iodonaphthalene were carried out with 1-Bromonaphthalene instead. All molar ratios were calculated using Equation 3.

$$\frac{M_x}{M_y} = \frac{I_x}{I_y} \cdot \frac{N_y}{N_x} \quad (3)$$

$\frac{M_x}{M_y}$ determines the molar ratio of the compounds x and y . I related to the integral of the NMR peak and N describes the number of nuclei that contributes to the signal. Finally, the mass percentages were calculated based on the molar ratios.^[188]

5.3.1 *bzpd*c-MOF single crystals

Since only small amount of Cd-*bzpd*c single crystals could be obtained, the sample amount was insufficient for ^1H -NMR investigations. Therefore, the results of the identical structured Zn-*bzpd*c investigations were used as representative results. In addition, it was assumed, that if the immersion liquid is able to enter the framework it will stay in a liquid state and thereby is detectable by liquid-state NMR investigations.

Table 13: Calculated relative concentrations of immersion liquids for *bzpd*c-single crystals by ^1H -NMR investigations (BNaph = 1-Bromonaphthalene, HydroT = hydrogenated terphenyl, DIM = diiodomethane).

MOF	Relative m% of		
	BNaph	HydroT	DIM
a) Zn- <i>bzpd</i> c	0.6	1.3	0.4
b) Hf- <i>bzpd</i> c	0.9	0.4	-
Zr- <i>bzpd</i> c	1.0	0.7	-

Within all tested *bzpd*c-MOFs no significant amount of immersion liquid could be detected, which indicates that none of the known and tested immersion liquid substances were able to enter the frameworks (results: Table 13, spectra: Appendix Figure 5 - Appendix Figure 7). The measured RIs were therefore considered as valuable.

These results thus confirm the studies by Mohmeyer et al. who showed that only fairly small molecules up to the size of 1-butanol can enter the framework. Larger benzene units are unable to fully enter the pore system.^[72]

5.3.2 γ -CD MOF

For the γ -CD-MOFs no significant amount of immersion liquid could be detected (results: Table 14, spectra: Appendix Figure 8). A possible explanation for these results might be found in the highly hydrophilic properties of the γ -CD pore system that does not favour the hydrophobic hydrogenated terphenyl.

Table 14: Calculated relative concentrations of immersion liquids for γ -CD single crystals by ¹H-NMR investigations.

MOF	Relative m% of hydrogenated terphenyl
Na- γ -CD	0.2
Li- γ -CD	0.3
K- γ -CD	0.5
Rb- γ -CD	0.1
Cs- γ -CD	0.2

5.3.3 ZIF single crystals

Table 15: Calculated relative concentrations of immersion liquids for ZIF single crystals by ¹H-NMR investigations (BNaph = 1-Bromonaphthalene, HydroT = hydrogenated terphenyl).

MOF	Relative m% of	
	BNaph	HydroT
ZIF-7	14.9	8.7
ZIF-8	16.2	7.7
ZIF-68	14.2	5.5
ZIF-69	19.0	9.4
ZIF-70	20.4	8.7
ZIF-78	20.5	6.7
ZIF-81	20.2	8.2
ZIF-82	26.7	8.0
ZIF-90	22.2	5.8

All ZIF single crystals show a visible uptake in both 1-bromonaphthalene and hydrogenated terphenyl (results: Table 15, spectra: Appendix Figure 9, Appendix Figure 10). This is probably due to the large pore sizes compared to the other investigated MOFs.

All obtained RIs were most likely measured with immersion liquids inside of the MOF framework. The results are therefore misleading and require the use of a different measurement method.

5.3.4 Other single crystals

Only a small amount of UiO-66-NO₂ single crystals could be synthesized and the synthesis was not reproducible. Since both UiO-66 and UiO-66-NO₂ possess the same overall framework structure, the results for UiO-66 were discussed as representative results.

Table 16: Calculated relative concentrations of immersion liquids for different MOF single crystals by ¹H-NMR investigations (BNaph = 1-Bromonaphthalene, HydroT = hydrogenated terphenyl, DIM = diiodomethane).

	MOF	Relative m% of		
		BNaph	HydroT	DIM
a)	<i>Al-pydc</i>	0.9	1.0	0.8
b)	UTSA-74	21.4	0.6	-
c)	UiO-66	14.4	0.9	-

The ¹H-NMR investigations (results: Table 16, spectra: Appendix Figure 11 - Appendix Figure 13) confirm that the immersion liquid can enter the UTSA-74 and UiO-66 framework structures. For *Al-pydc* no significant amount of immersion liquid could be detected. These results are consistent with the framework of these MOFs. *Al-pdc* possesses a very dense and closely packed structure,^[68] whereas the structures of UiO-66 and UTSA-74 show pores of up to 11 Å.^[98]

5.4 Perovskite-MOF materials

This subchapter provides further information on the prepared MOF and MOF-perovskite materials and their syntheses results. All data was obtained in cooperation with the group of Professor Tae-Woo Lee at the Seoul National University in South Korea.

5.4.1 Cerium MOFs

The Ce(IV)*bdc*-MOF was synthesized based on an adaption of the synthesis reported by Ren et al.^[29] However, by simply following the given synthesis route large amounts of unreacted terephthalic acid were obtained besides the product. In order to prevent the residual reactant, additional washing steps were added at the end of the synthesis route (section 4.3.1). The measured XRD pattern obtained from the synthesis with additional washing steps now matches well with the literature. In addition, both SEM (Appendix Figure 4) and TEM images (Figure 30) now only show the characteristic octahedral shape of the *bdc*-MOF.

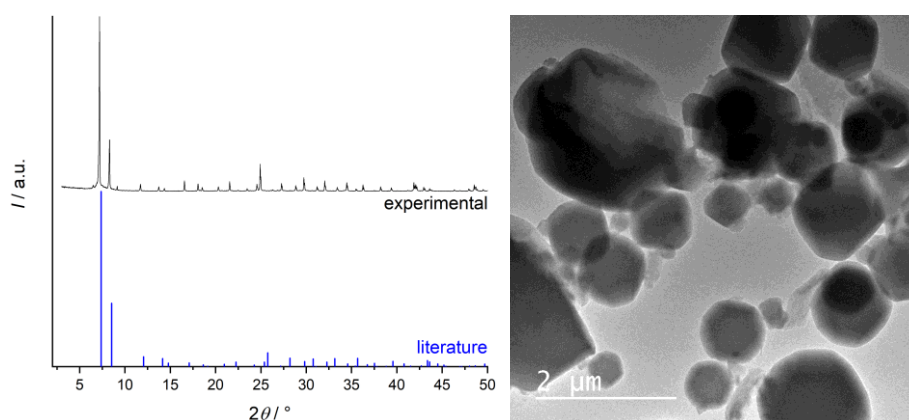


Figure 30: Left: XRD pattern, Right: TEM image of the obtained Ce(IV)*bdc*-MOF.

The mesoporous system within the Ce(IV)*bdc*-MOF was confirmed by physisorption data (Figure 31). The Type IV curve clearly shows a hysteresis which is caused by the mesoporous system and matches well with the literature.^[29] Regarding all these factors the reproduction can be considered a success when additional washing steps are implemented.

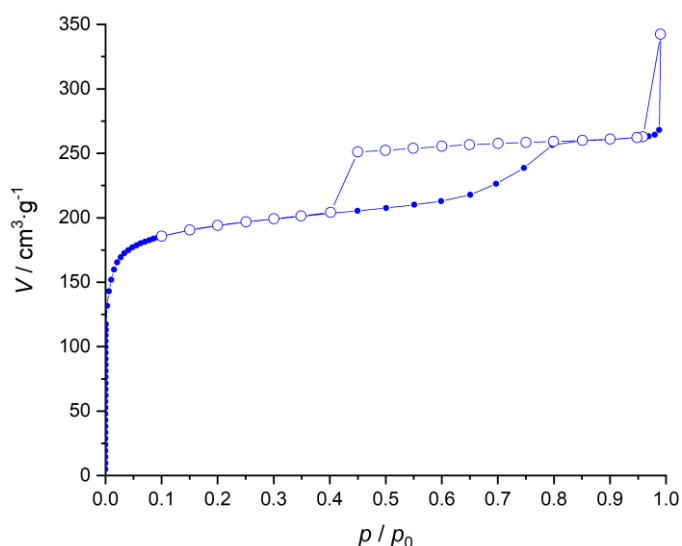


Figure 31: Obtained physisorption data from the synthesized Ce(IV)*bdc*-MOF.

5.4.2 MOF-Perovskite-SiO₂ synthesized after Ren et al.

The synthesis of CsPbBr₃ nanoparticles into the MOF structure, yielded a different outcome compared to the one reported in literature.^[29] Instead of synthesizing pure-phase CsPbBr₃ nanoparticles, a mixture of CsPbBr₃ and Cs₄PbBr₆ nanoparticles was obtained (Figure 32). The majority of the perovskite components, was unreacted caesium bromide (CsBr).

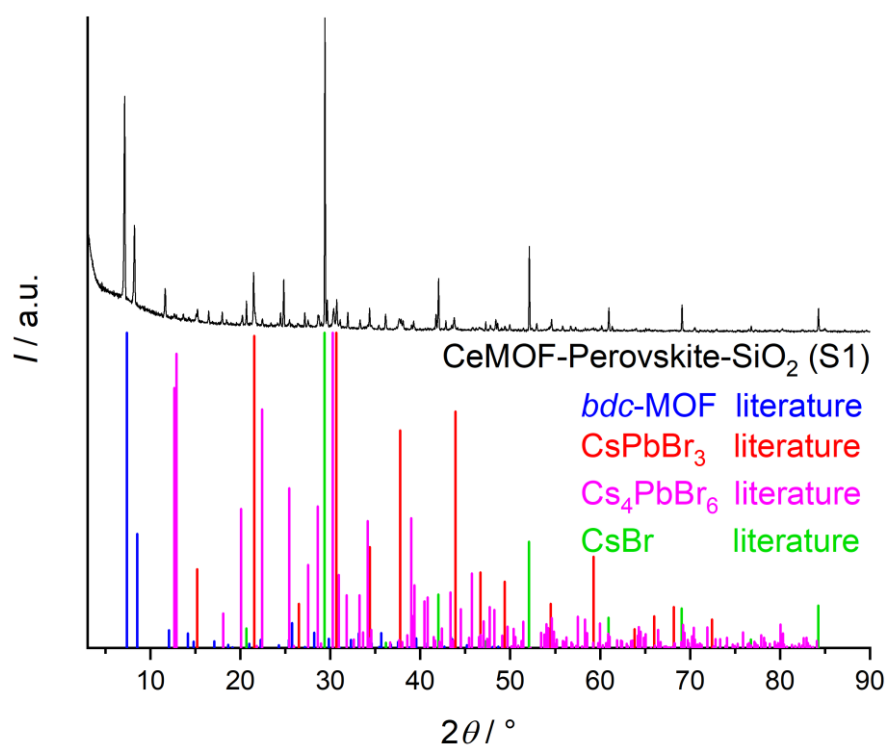


Figure 32: Diffractogram of the obtained hybrid material - synthesis after Ren et al^[29].

Large amounts of unreacted CsBr crystals can be recognized within SEM images, which matches well with the results obtained from XRD measurements. In comparison to the octahedral MOF-perovskite particles, CsBr particles are easily identified since they crystallize in a cubic shape (Figure 33b).

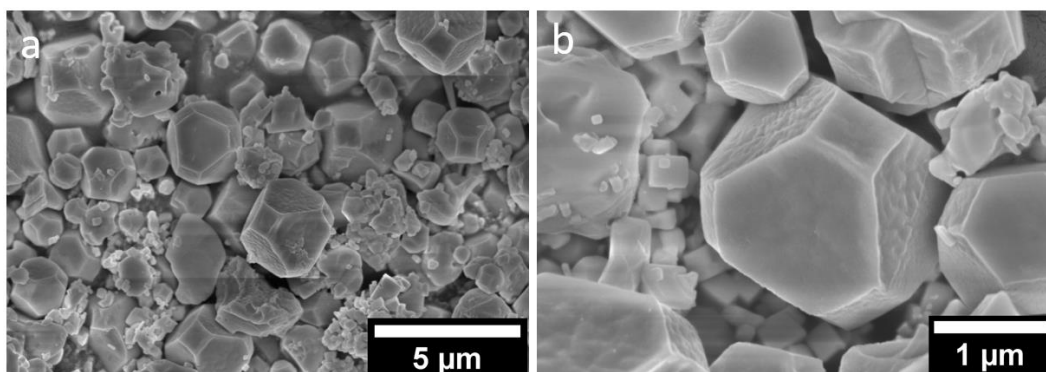


Figure 33: SEM-images of the modified Ce-MOF according to Ren et al. ^[29] with different magnifications.

The formation of perovskites within the MOF structure was carried out at ambient conditions as reported by Ren et al.^[29] However, the synthesis of perovskites is highly sensitive to water and humidity. At the day of the experiment the humidity was around 80 %, which can be the cause to the formation of the Cs_4PbBr_6 phase. Furthermore, upon cooling the CsBr solution to perform the perovskite formation at room temperature, a large part of the previously dissolved CsBr recrystallizes. This also results in the rather low ratio of formed perovskites. Therefore, this synthesis route is not ideal for future LED materials. Nevertheless, it was still further investigated to study the impact of large amounts of CsBr impurities on the stability and the materials stability and performance. As labelled in Figure 32, this sample will be referred to as sample S1.

Since this synthesis route contains little to no washing after the perovskite formation, another route that included washing steps was carried out. The results are reported within section 5.4.3.

5.4.3 MOF-Perovskite-SiO₂ syntheses after Wu et al.

In order to create a material with less residual CsBr, the perovskite confinement step provided by Ren et al.^[29] was substituted by the one reported by Wu et al.^[181] As intended, the outcome of this synthesis route yielded a material with smaller residue of CsBr (Figure 34) compared to results reported in section 5.4.2 (Figure 32). In contrast to section 5.4.2, only the CsPbBr₃ perovskite phase could be identified.

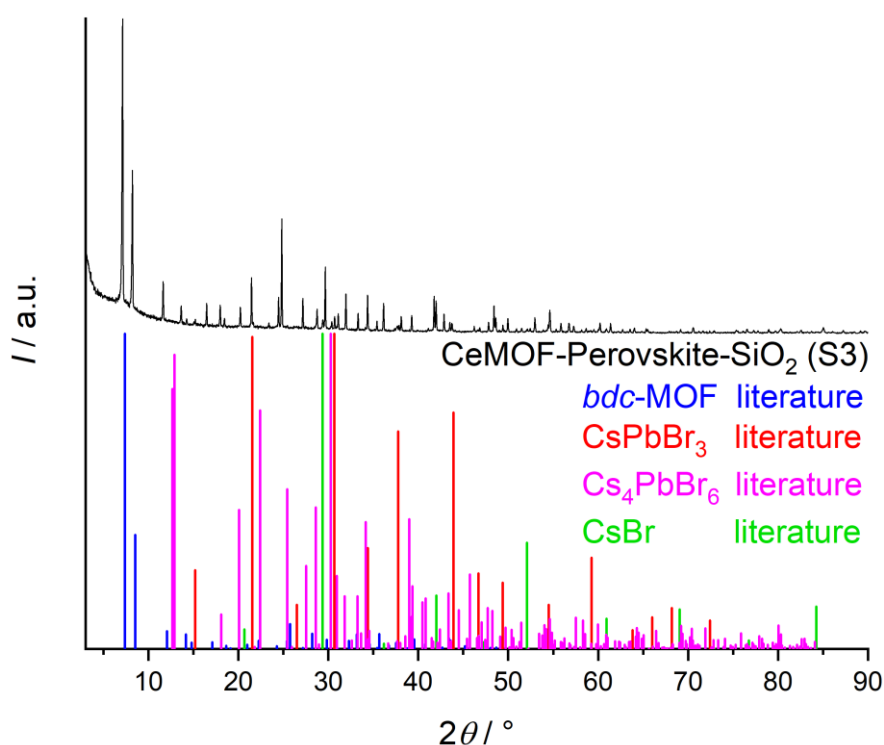


Figure 34: Diffractogram of the obtained hybrid material – modified synthesis.^[29,181]

As labelled in Figure 34, this sample will be referred to as sample S3.

5.5 Characterization of Perovskite-MOF materials

The performance of the above described materials was evaluated with regard to the photoluminescence quantum yield (short: PLQY) and stability under specific circumstances. All materials were tested as films (section 4.3.5).

5.5.1 High flux testing

Both materials sample S1 and sample S3 were exposed to blue light irradiation of 460 nm with high flux of $240 \text{ mW}\cdot\text{cm}^{-2}$ to test their stability. Figure 35 displays the PLQY spectra of sample S1 after irradiation with high flux blue light for several hours.

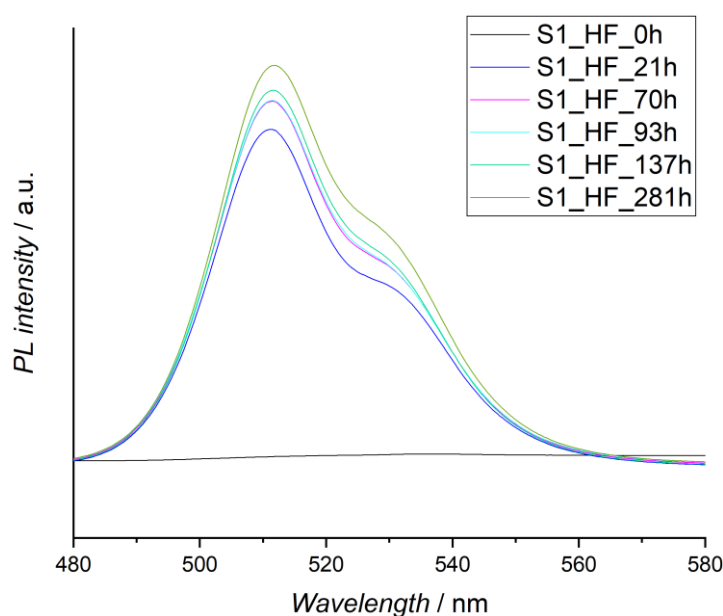


Figure 35: PLQY spectra of S1 after irradiation under blue, high flux light with varying time.

Since the shape of the curve consists of a main peak accompanied by a shoulder one, the spectra indicates the presence of two phases. Phase one exhibits a maximum emission at 511 nm, whereas the second, smaller peak appears around 530 nm. Since the peak observed by Ren et al.^[29] for confined pure-phased CsPbBr_3 was reported at 519 nm, the measured peak at 511 nm can be ascribed to the CsPbBr_3 perovskite phase. The second, less intense peak at higher wavelength can therefore be ascribed to the Cs_4PbBr_6 phase as identified by XRD analysis (Figure 32).

Values for Cs_4PbBr_6 emission peaks in literature are reported around 523 nm^[189], which is close to the observed 530 nm shoulder peak. The difference between the measured peak positions to the literature ones for CsPbBr_3 and Cs_4PbBr_6 perovskite phases can be caused by different particle sizes^[190,191] and slightly different excitation wavelengths.

The PLQY emission spectra for sample S3 are displayed in Figure 36.

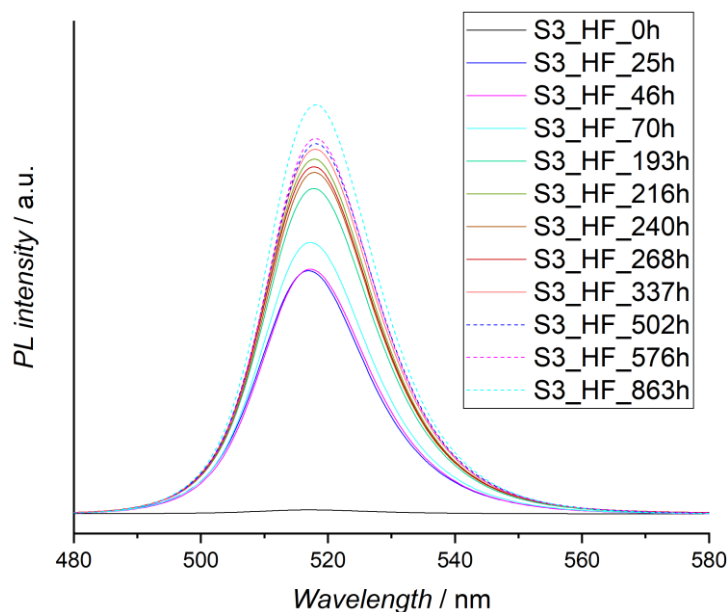


Figure 36: PLQY spectra of S3 after irradiation under blue, high flux light with varying time.

Compared to the data shown in Figure 35 sample S3 exhibits only one peak at around 518 nm. This peak is very close to the one reported in literature (519 nm)^[29] and clearly indicates the sole presence of CsPbBr_3 as the dominating perovskite phase. In contrast to Figure 35 no second peak could be identified in the measured wavelength range. Therefore, it can be assumed, that no or no significant amounts of the Cs_4PbBr_6 are present in sample S3. Furthermore, no changes in the perovskite phase composition of the emitting part of the samples are detectable via PLQY emission spectra data over the course of the high flux testing.

Apart from the recorded emission spectra, the PLQY values were calculated. Their change over time is displayed in Figure 37 for both sample S1 and sample S3 undergoing high flux stress testing.

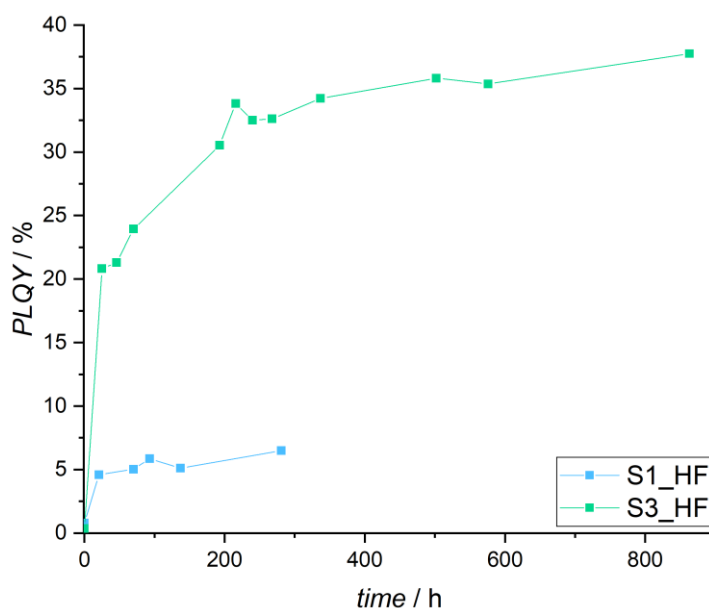


Figure 37: Calculated PLQY for films exposed to high flux stability testing conditions over time. It is clear, that both samples increase their PLQY performance over time. Usually, films that undergo stability testing show a PLQY-decrease as can be seen in Figure 38.^[29]

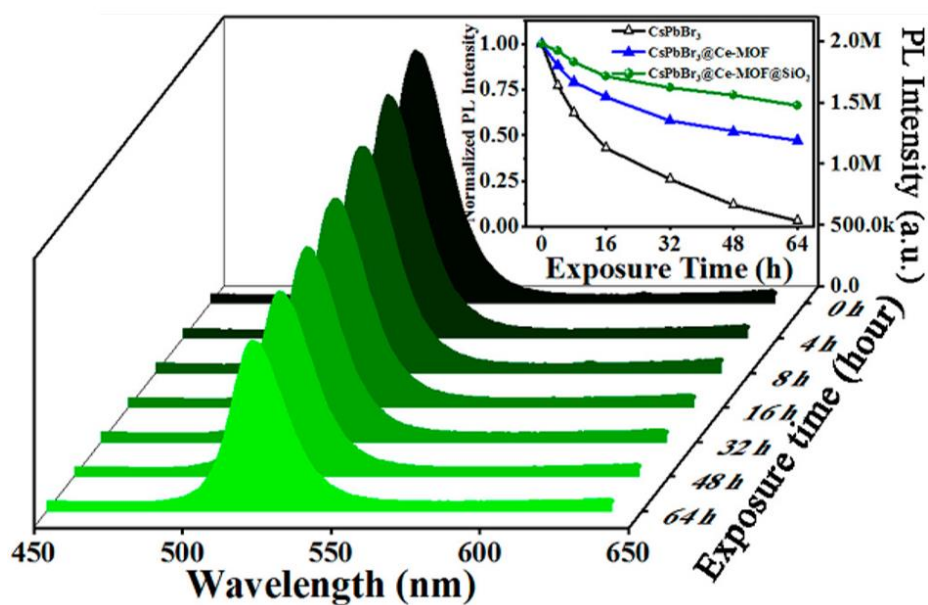


Figure 38: Time-dependent PLQY spectra and data of CsPbBr₃@Ce-MOF@SiO₂ material undergoing photostability stress testing, as reported by Ren et al.^[29]

The observed, unusual PLQY increase in Figure 37 is most likely caused by favourable effects due to the illumination. However, we were unable to exactly identify the occurring phenomena. Our main assumption is that under irradiation, surface defects of the perovskite particles were most likely healed which then leads to a PLQY increase.

Small amounts of added CsBr can induce beneficial effects. CsBr-CsPbBr₃ composites or CsBr treated perovskites are reportedly able to induce a high-level defect passivation.^[192] Nevertheless, this effect was only observed for small amounts of CsBr. Since CsBr itself has no significant luminous properties, large amounts of added CsBr will very likely decrease the overall performance of the LED material.

Still a hundred-times increase of PLQY, as it was measured for sample S3, is very unusual. In addition, sample S3 outperforms the obtained PLQY values from sample S1. As already mentioned above, this is most likely due to the high CsBr impurities of sample S1, since CsBr itself does not emit light. Furthermore, sample S3 contains a higher amount of CsPbBr₃ perovskite particles, as can be seen from XRD measurements, which results in an expected, higher PLQY performance. Cs₄PbBr₆ is known to be a major efficiency-limiting factor among perovskite synthesis, as a result the performance of sample S1 decreases.^[192]

5.5.2 60-90 testing

In order to test the materials stability against heat and moisture, sample S1 and sample S3 were exposed to 90 % humidity and 60 °C (60-90 test). Their emission spectra and PLQY values were determined after different exposure times.

Figure 39 displays the emission spectra of sample S1 during the 60-90 testing. As already observed and discussed in section 5.5.1, the shape of the spectra indicates the presence of two perovskite phases. The first peak at around 513 nm can be assigned to the CsPbBr₃ phase. The second peak at around 530 nm is caused by the Cs₄PbBr₆ phase.

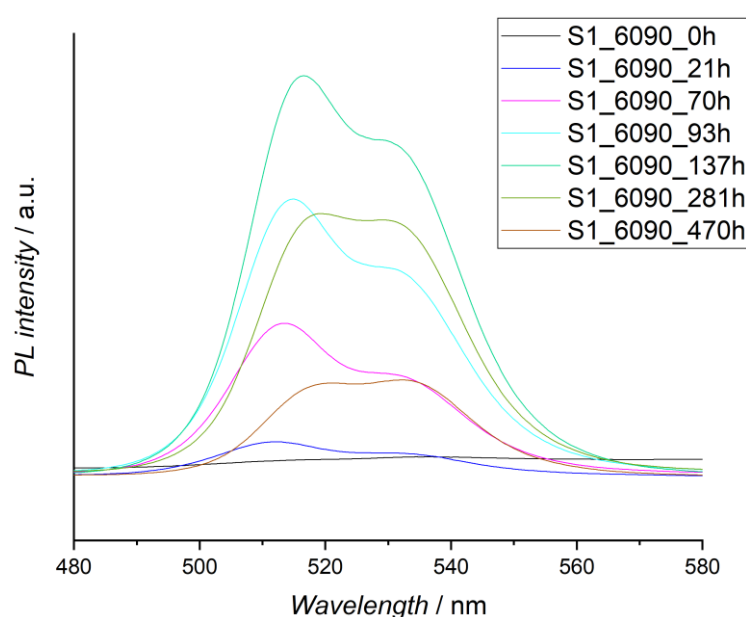
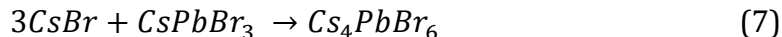


Figure 39: PLQY spectra of S1 after exposition to 60 °C at 90 % humidity with varying time.

Unlike the observed behaviour under high flux testing, the ratio of the peak intensities does vary for the 60-90 testing. This indicates that during these testing conditions, the perovskite phase composition changes. Over time a considerable increase of the second peak, which corresponds to the Cs₄PbBr₆ phase, is measured. After 470 hours, the highest intensity peak is no longer caused by the CsPbBr₃ phase but by the Cs₄PbBr₆ phase (Figure 39).

The high humidity leads to an overall increase of the water content of the film, resulting in a Cs⁺ and Br⁻ rich environment through dissolvment of the residual CsBr.^[193] The enriched environment then causes the formation of the Cs₄PbBr₆ phase via the reaction as follows.^[194]



In addition, the water molecules coordinate to the surface of the CsPbBr₃ phase inducing small structural changes of the outer layer. Especially, the increased effective radius of the incorporated Cs⁺ ions enables an easier formation of the Cs₄PbBr₆ phase later on.^[194]

The PLQY emission spectra for sample S3 are displayed in Figure 40. Just like the emission spectra obtained for high flux tests of sample S3 (Figure 36) the material exhibits only one peak at around 518 nm. This peak is as already mentioned very close to the reported literature one^[29] and clearly indicates the presence of CsPbBr₃.

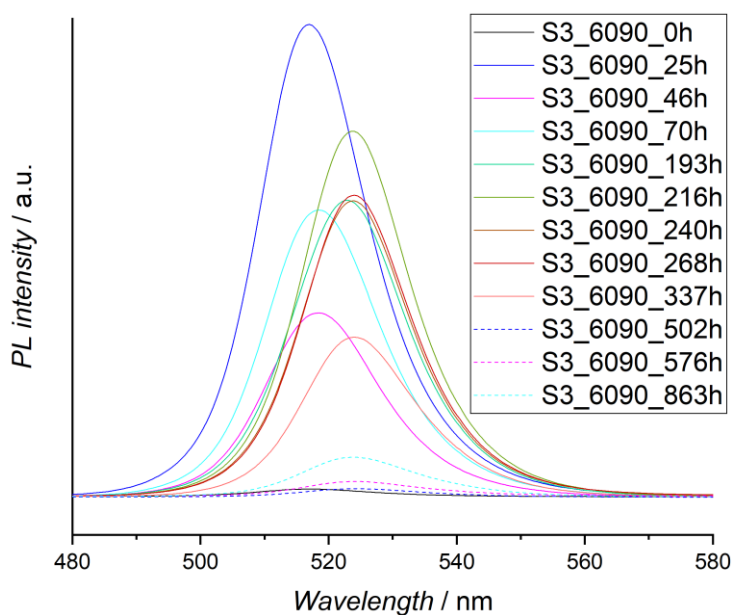


Figure 40: PLQY spectra of S3 after exposure to 60 °C at 90 % humidity with varying time.

However, for the measured emission spectra of the 60-90 testing, a peak-shift from 518 to 524 nm occurred over the course of several hundred hours. The shift could be caused by multiple phenomena like ageing^[195] or particle size increase^[190,191].

Apart from the recorded emission spectra, the exhibited PLQY values were calculated. Their change over time for both sample S1 and sample S3 undergoing 60-90 stress testing is displayed in Figure 42.

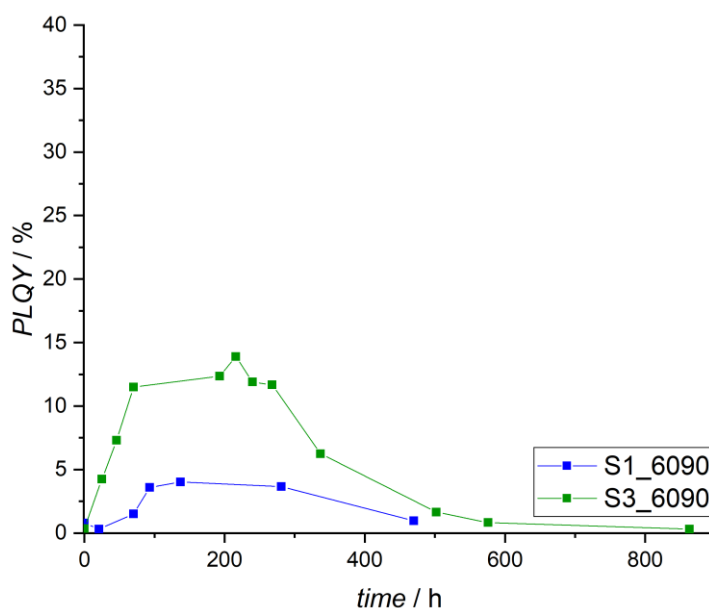


Figure 41: Calculated PLQY for films exposed to 60-90 stability testing conditions over time.

Both curves show a PLQY-increase over the first 200 hours, which is then followed by a decrease back to the initial PLQY.

Similar observed behaviour was also reported by Girolamo et al. First, the performance of CsPbBr₃ particles exposed to humidity increases due to improvement of the crystal structure, induced by particle growth and defect healing. If the humidity exposure exceeds a certain timeframe, it has a negative performance impact. Prolonged exposure to humidity causes the conversion of the CsPbBr₃ phase into possibly CsPb₂Br₅ and/or Cs₄PbBr₆·H₂O resulting in a lowered light-emitting performance.^[196] This confirms the observed increase of Cs₄PbBr₆ determined from Figure 39.

An explanation for the increased stability can also be found in the protecting MOF matrix and silica layer. Both exhibit insulating properties and prevent heat propagation between the perovskites and the heating source.^[197] These insulating effects counter the usual, thermally induced PLQY performance loss. Moreover, the formed perovskite nanocrystals are most likely well dispersed within the MOF host matrix. This inhibits heat-induced aggregation and furthermore decreases the thermal damage.^[198]

6 Conclusion and Outlook

In this work, large single crystals of various metal-organic framework compounds could be synthesized and characterized. Among other things, the composition was varied with regard to the use of differently substituted organic linker molecules and different metal ions. In particular, the chosen method for refractive index (short: RI) measurements is suitable for the determination of anisotropic RIs. The possibilities of the applicability of the immersion method were further established and verified in this work. In addition to the optical characterization, experiments were carried out towards optical application of the materials. For this purpose, MOF-perovskite materials were synthesized and investigated regarding their performance and stability.

In order to obtain a variety of different, large MOF single crystals a lot of effort was put into the search to find suitable syntheses. All in all, 22 different and measurable large and transparent to lightly-coloured single crystals could be synthesized, not including the post-synthetically modified ones. These single crystals were then measured with the immersion method at the University of Bremen. The obtained, RIs are listed below in Table 17. Since the immersion method is suitable to determine anisotropic RIs, up to three RIs were measured per single crystal. The number of RIs is determined by the specific crystal system. The general trend of results depending on metal ion and/or organic linker group variation in most cases also complies with literature known calculation systems for minerals^[49] and organic compounds^[50,51,53].

Further investigations concerning the usability of the immersion method for RI measurement of MOF single crystals was carried out. The results showed, that the immersion method cannot be applied to MOF structures with large pore sizes, since the immersion liquid is able to enter the framework affecting its inherent refractive properties. Also, a hydrophilic pore system is beneficial to prevent the hydrophobic immersion liquids from entering. Nevertheless, the evaluation could only be carried out for known immersion liquid substances. Substances, that were not named due to trade secret could not be investigated. As a result, the immersion method can be viewed as a first, novel step towards precise anisotropic RI measurements of MOFs. The immersion

method is able to precisely determine orientations for successful measurements. Unfortunately, due to the absorbance of immersion liquids into some MOFs the search for a more sufficient measurement method continues. Apart from the search of a new measurement method, next steps could be the creation of an increment system to predict the RIs of MOFs. However, in order to prove such a system more RI data is needed. A further step would also be the creation of an optical device that makes use of the directional dependence of the refractive index in certain MOF structures.

Table 17: Immersion method RI measurements of synthesized MOF single crystals at 589 nm. Information given in grey lettering shows the RIs of MOF measured with immersion liquids inside of the framework.

MOF	RI _{immersion method} \pm 0.0032		
<i>Al-pydc</i>	n_x : 1.7025	n_y : 1.446	n_z : 1.684
<i>Cd-bzpd</i>	n_x : 1.524	n_y : >1.8	n_z : 1.7575
<i>Zn-bzpd</i>	n_x : 1.760	n_y : 1.640	n_z : 1.602
<i>Hf-bzpd</i> ^[70]	n_x : 1.658	n_y : 1.578	n_z : 1.590
<i>Zr-bzpd</i> ^[70]	n_x : 1.680	n_y : 1.580	n_z : 1.604
UiO-66 ^[70]		1.574	
UiO-66-NO ₂ ^[70]		1.594	
UTSA-74	n_e : 1.651		n_o : 1.542
Cs- γ -CD MOF		1.525	
K- γ -CD MOF		1.518	
Li- γ -CD MOF		1.515	
Rb- γ -CD MOF		1.520	
Na- γ -CD MOF	n_x : 1.510	n_y : 1.515	n_z : 1.514
ZIF-7	n_x : 1.628	n_y : 1.639	n_z : 1.654
ZIF-8		1.533	
ZIF-68	n_e : 1.544		n_o : 1.551
ZIF-69	n_e : 1.547		n_o : 1.524
ZIF-70	n_e : 1.624		n_o : 1.598
ZIF-78	n_e : 1.587		n_o : 1.616
ZIF-81	n_e : 1.603		n_o : 1.569
ZIF-82	n_e : 1.536		n_o : 1.546
ZIF-90		1.588	

Concerning optical applications, a Ce(IV)-MOF with a mesopore system was synthesized. Perovskite nanocrystals were then formed in-situ and confined within the mesoporous channel. Afterwards the MOF-perovskite hybrid materials were coated with a thin silica shell. In comparison to the literature, the already known synthesis route was refined with washing steps during the MOF synthesis and a second perovskite confinement method was tested. Despite these efforts the reported photoluminescence quantum yield (PLQY) of 78 %^[29] could not be reached. However, during the stability testing the initially very low PLQY drastically increased. The observed increase was highly interesting, since it did not match the decrease observed in literature (s. Figure 42).

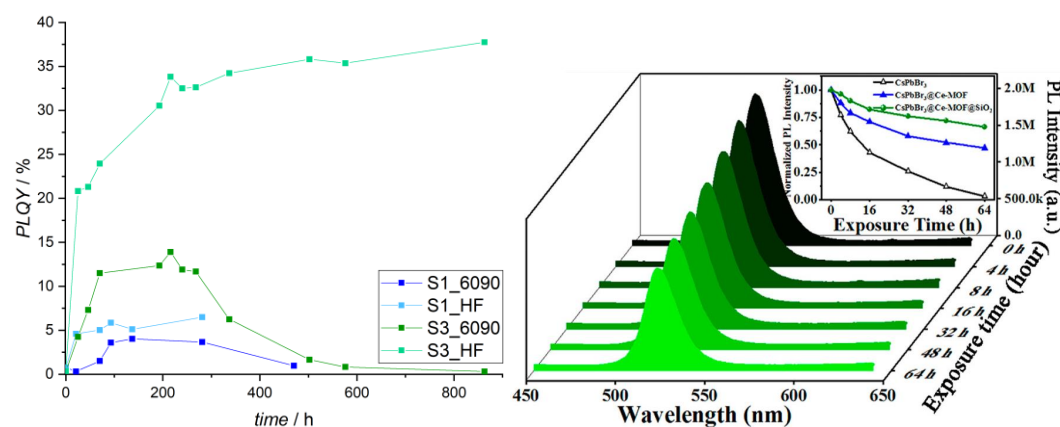


Figure 42: Left) PLQY values of S1 and S3 under different conditions and over time; Right) photostability test of CsPbBr₃@Ce-MOF@SiO₂ reported by Ren et al.^[29]

The starting low PLQYs combined with the drastic initial increase is most likely caused by surface defects of the synthesized perovskite nanoparticles, which are then healed by exposure to humidity or high flux blue light irradiation.^[196] Overall sample S3, which was synthesized using an alternative perovskite confining method that contains additional washing steps, clearly outperforms sample S1, which was synthesized according to literature. This is due to the fact that during the synthesis of sample S1 apart from CsPbBr₃ also Cs₄PbBr₆ was formed. Since Cs₄PbBr₆ is known to be a major efficiency-limiting factor compared to pure-phased CsPbBr₃, the performance thereby decreases.^[192] Despite the observed and very interesting phenomena, the performance is not at a sufficient level. Apart from further investigation of the occurring PLQY increase, the search for a highly stable and sufficient MOF-perovskite material continues. One opportunity could lie in perovskite confinement within highly

light-emitting MOF structures with PLQYs close to 100 %.^[199] These MOF structures possess complex, light emitting linker molecules but oftentimes suffer from a slight decrease in stability compared to other MOF structures. However, with the addition of an outer silica layer on top of the MOF-perovskite material, it could still show a great stability increase combined with a tremendous PLQY increase. Next steps would be the in-depth investigation of the observed efficiency and structural changes with frequent analysis steps within the stress testing process. For example, tracking the structural change with frequent XRD measurements. In addition, the effects of the used polymer for the film formation need to be determined. Therefore, a comparison between pure powder and film could provide useful information. For pure powder, changes of the overall perovskite particle size might be resolved with TEM imaging.

7 References

- [1] S. Bauer, N. Stock, *Chem. Unserer Zeit* **2008**, *42*, 12.
- [2] H. Li, M. Eddaoudi, M. O'Keeffe, O. M. Yaghi, *Nature* **1999**, *402*, 276.
- [3] M. Schröder, *Functional Metal-Organic Frameworks*, Springer Berlin / Heidelberg, Berlin, Heidelberg, **2010**.
- [4] A. Dhakshinamoorthy, Z. Li, H. Garcia, *Chemical Society reviews* **2018**, *47*, 8134.
- [5] M. Schulz, A. Gehl, J. Schlenkrich, H. A. Schulze, S. Zimmermann, A. Schaate, *Angewandte Chemie (International ed. in English)* **2018**, *57*, 12961.
- [6] S. S. Dhankhar, N. Sharma, C. M. Nagaraja, *Inorg. Chem. Front.* **2019**, *6*, 1058.
- [7] H. Wang, W. Yang, Z.-M. Sun, *Chemistry, an Asian journal* **2013**, *8*, 982.
- [8] X.-F. Wang, X.-Z. Song, K.-M. Sun, L. Cheng, W. Ma, *Polyhedron* **2018**, *152*, 155.
- [9] S. Ma, H.-C. Zhou, *Chem. Commun.* **2010**, *46*, 44.
- [10] H. Li, K. Wang, Y. Sun, C. T. Lollar, J. Li, H.-C. Zhou, *Materials Today* **2018**, *21*, 108.
- [11] B. Li, H.-M. Wen, W. Zhou, B. Chen, *The journal of physical chemistry letters* **2014**, *5*, 3468.
- [12] B. van de Voorde, B. Bueken, J. Denayer, D. de Vos, *Chemical Society reviews* **2014**, *43*, 5766.
- [13] Y. He, R. Krishna, B. Chen, *Energy Environ. Sci.* **2012**, *5*, 9107.
- [14] P. Horcajada, T. Chalati, C. Serre, B. Gillet, C. Sebrie, T. Baati, J. F. Eubank, D. Heurtaux, P. Clayette, C. Kreuz et al., *Nature materials* **2010**, *9*, 172.
- [15] P. Horcajada, R. Gref, T. Baati, P. K. Allan, G. Maurin, P. Couvreur, G. Férey, R. E. Morris, C. Serre, *Chemical reviews* **2012**, *112*, 1232.
- [16] O. K. Farha, I. Eryazici, N. C. Jeong, B. G. Hauser, C. E. Wilmer, A. A. Sarjeant, R. Q. Snurr, S. T. Nguyen, A. Ö. Yazaydın, J. T. Hupp, *Journal of the American Chemical Society* **2012**, *134*, 15016.
- [17] Z. Chen, M. C. Wasson, R. J. Drout, L. Robison, K. B. Idrees, J. G. Knapp, F. A. Son, X. Zhang, W. Hierse, C. Kühn et al., *Faraday discussions* **2021**, *225*, 9.
- [18] K.-J. Kim, P. Lu, J. T. Culp, P. R. Ohodnicki, *ACS sensors* **2018**, *3*, 386.
- [19] J. Hromadka, B. Tokay, S. James, R. P. Tatam, S. Korposh, *Sensors and Actuators B: Chemical* **2015**, *221*, 891.
- [20] A. Morozan, F. Jaouen, *Energy Environ. Sci.* **2012**, *5*, 9269.
- [21] W. Liu, X.-B. Yin, *TrAC Trends in Analytical Chemistry* **2016**, *75*, 86.
- [22] Y. Huang, C.-A. Tao, R. Chen, L. Sheng, J. Wang, *Nanomaterials (Basel, Switzerland)* **2018**, *8*.
- [23] a) Chester B. Slawson, A. B. Peck, *American Mineralogist* **1936**, *21*, 523; b) T. Danhara, T. Yamashita, H. Iwano, M. Kasuya, *Quaternary International* **1992**, *13-14*, 89; c) D. A. Robinson, *Vadose Zone Journal* **2004**, *3*, 705.
- [24] F. D. Bloss, *The spindle stage. Principles and practice*, Cambridge Univ. Press, Cambridge, **(1981)**.

- [25] A. G. Zavyalova, D. V. Kladko, I. Y. Chernyshov, V. V. Vinogradov, *J. Mater. Chem. A* **2021**, *9*, 25258.
- [26] S. Huang, Z. Li, B. Wang, N. Zhu, C. Zhang, L. Kong, Q. Zhang, A. Shan, L. Li, *ACS applied materials & interfaces* **2017**, *9*, 7249.
- [27] Y. Wang, H.-M. Meng, Z. Li, *Nanoscale* **2021**, *13*, 8751.
- [28] J. Ren, X. Zhou, Y. Wang, *Chemical Engineering Journal* **2020**, *391*, 123622.
- [29] J. Ren, A. Meijerink, X. Zhou, J. Wu, G. Zhang, Y. Wang, *ACS applied materials & interfaces* **2022**, *14*, 3176.
- [30] O. M. Yaghi, H. Li, *J. Am. Chem. Soc.* **1995**, *117*, 10401.
- [31] P. Roy, A. Schaate, P. Behrens, A. Godt, *Chemistry (Weinheim an der Bergstrasse, Germany)* **2012**, *18*, 6979.
- [32] X.-C. Huang, Y.-Y. Lin, J.-P. Zhang, X.-M. Chen, *Angewandte Chemie (International ed. in English)* **2006**, *45*, 1557.
- [33] K. S. Park, Z. Ni, A. P. Côté, J. Y. Choi, R. Huang, F. J. Uribe-Romo, H. K. Chae, M. O'Keeffe, O. M. Yaghi, *Proceedings of the National Academy of Sciences of the United States of America* **2006**, *103*, 10186.
- [34] W. Xu, O. M. Yaghi, *ACS central science* **2020**, *6*, 1348.
- [35] Josephine Nakhla, Stephen Caskey, Ph.D, "Metal Organic Frameworks (MOFs)", can be found under <https://www.sigmaaldrich.com/DE/de/technical-documents/technical-article/materials-science-and-engineering/photovoltaics-and-solar-cells/metal-organic-frameworks>, **2023**.
- [36] E. Hecht, *Optik*, Oldenbourg, München, Wien, **2005**.
- [37] D. A. Skoog, J. J. Leary, *Instrumentelle Analytik. Grundlagen - Geräte - Anwendungen*, Springer, Berlin, Heidelberg, **1996**.
- [38] Lecture note of Dr. Hiroshi Yamamoto, "<https://www.pirika.com/ENG/TCPE/RI-Theory.html>. Estimation of Refractive Index.", **2019**.
- [39] E. Redel, Z. Wang, S. Walheim, J. Liu, H. Gliemann, C. Wöll, *Appl. Phys. Lett.* **2013**, *103*, 91903.
- [40] N. C. Keppler, K. D. J. Hindricks, P. Behrens, *RSC Adv.* **2022**, *12*, 5807.
- [41] A. García Márquez, A. Demessence, A. E. Platero-Prats, D. Heurtaux, P. Horcajada, C. Serre, J.-S. Chang, G. Férey, V. A. de La Peña-O'Shea, C. Boissière et al., *European Journal of Inorganic Chemistry* **2012**, *2012*, 5165.
- [42] G. Lu, J. T. Hupp, *Journal of the American Chemical Society* **2010**, *132*, 7832.
- [43] Z. Li, J. Liu, X. Yi, W. Wu, F. Li, Z. Zhu, H. Li, J. Shi, Y. Xu, F. Zhou et al., *Advanced Functional Materials* **2022**, *32*, 2109541.
- [44] P. Horcajada, C. Serre, D. Grosso, C. Boissière, S. Perruchas, C. Sanchez, G. Férey, *Adv. Mater.* **2009**, *21*, 1931.
- [45] W. Yin, C.-A. Tao, F. Wang, J. Huang, T. Qu, J. Wang, *Sci. China Mater.* **2018**, *61*, 391.
- [46] W. Yin, C.-A. Tao, X. Zou, F. Wang, T. Qu, J. Wang, *Nanomaterials* **2017**, *7*, 242.

- [47] A. V. Vinogradov, V. A. Milichko, H. Zaake-Hertling, A. Aleksovskaja, S. Gruschinski, S. Schmorl, B. Kersting, E. M. Zolnhofer, J. Sutter, K. Meyer et al., *Dalton Trans.* **2016**, 45, 7244.
- [48] H.-L. Jiang, T. A. Makal, H.-C. Zhou, *Coordination Chemistry Reviews* **2013**, 257, 2232.
- [49] R. D. Shannon, R. X. Fischer, *American Mineralogist* **2016**, 101, 2288.
- [50] F. Eisenlohr, *Z. physik. Chem.* **1911**, 585.
- [51] A. Vogel, *J. Chem. Soc.* **1948**, 1833.
- [52] S. S. Batsanov, *Refractometry and Chemical Structure*. Authorized Translation from the Russian by Paul Porter Sutton, Consultants Bureau, New York, **1961**.
- [53] F. Eisenlohr, *Z. physik. Chem.* **1912**, 129.
- [54] Olaf Medenbach, "Atlas der Kristalloptik", can be found under <https://homepage.rub.de/olaf.medenbach/index.html>, **2007**.
- [55] M. E. Gunter, *American Mineralogist* **2005**, 90, 1648.
- [56] Chui, Lo Charmant, Orpen, Williams, *Science (New York, N.Y.)* **1999**, 283, 1148.
- [57] S. Han, Y. Wei, C. Valente, I. Lagzi, J. J. Gassensmith, A. Coskun, J. F. Stoddart, B. A. Grzybowski, *Journal of the American Chemical Society* **2010**, 132, 16358.
- [58] S. Diring, S. Furukawa, Y. Takashima, T. Tsuruoka, S. Kitagawa, *Chem. Mater.* **2010**, 22, 4531.
- [59] A. Schaate, P. Roy, A. Godt, J. Lippke, F. Waltz, M. Wiebcke, P. Behrens, *Chemistry (Weinheim an der Bergstrasse, Germany)* **2011**, 17, 6643.
- [60] F. J. Carmona, C. R. Maldonado, S. Ikemura, C. C. Romão, Z. Huang, H. Xu, X. Zou, S. Kitagawa, S. Furukawa, E. Barea, *ACS applied materials & interfaces* **2018**, 10, 31158.
- [61] T. Tsuruoka, S. Furukawa, Y. Takashima, K. Yoshida, S. Isoda, S. Kitagawa, *Angewandte Chemie (International ed. in English)* **2009**, 48, 4739.
- [62] C. A. Trickett, K. J. Gagnon, S. Lee, F. Gándara, H.-B. Bürgi, O. M. Yaghi, *Angewandte Chemie (International ed. in English)* **2015**, 54, 11162.
- [63] G. C. Shearer, S. Chavan, S. Bordiga, S. Svelle, U. Olsbye, K. P. Lillerud, *Chem. Mater.* **2016**, 28, 3749.
- [64] N. Kim, J. H. Park, J. Paczesny, B. A. Grzybowski, *CrystEngComm* **2019**, 21, 1867.
- [65] H. Bux, C. Chmelik, R. Krishna, J. Caro, *Journal of Membrane Science* **2011**, 369, 284.
- [66] S. Yuan, Y.-K. Deng, Di Sun, *Chemistry – A European Journal* **2014**, 20, 10093.
- [67] S. Liu, Y. Zhang, Y. Meng, F. Gao, S. Jiao, Y. Ke, *Crystal Growth & Design* **2013**, 13, 2697.
- [68] M. T. Wharmby, N. Stock, *Z. anorg. allg. Chem.* **2018**, 644, 1816.
- [69] L. Qin, L. Yu, X.-Z. Yan, W.-N. Zhao, L. Han, *Inorganica Chimica Acta* **2014**, 409, 233.
- [70] Anna-Lena Erika Renate Deutsch, *Master Thesis*, Gottfried Wilhelm Leibniz University, Hanover, **2019**.
- [71] A. Mohmeyer, A. Schaate, B. Brechtken, J. C. Rode, D. P. Warwas, G. Zahn, R. J. Haug, P. Behrens, *Chemistry (Weinheim an der Bergstrasse, Germany)* **2018**, 24, 12848.
- [72] A. Mohmeyer, M. Schäfer, A. Schaate, S. Locmelis, A. M. Schneider, P. Behrens, *Chemistry (Weinheim an der Bergstrasse, Germany)* **2020**, 26, 2222.

- [73] C. Atzori, K. A. Lomachenko, S. Øien-Ødegaard, C. Lamberti, N. Stock, C. Barolo, F. Bonino, *Crystal Growth & Design* **2019**, *19*, 787.
- [74] Z. Chen, S. Xiang, H. D. Arman, P. Li, D. Zhao, B. Chen, *Eur. J. Inorg. Chem.* **2011**, *2011*, 2227.
- [75] M. C. Das, H. Xu, S. Xiang, Z. Zhang, H. D. Arman, G. Qian, B. Chen, *Chemistry (Weinheim an der Bergstrasse, Germany)* **2011**, *17*, 7817.
- [76] M. C. Das, H. Xu, Z. Wang, G. Srinivas, W. Zhou, Y.-F. Yue, V. N. Nesterov, G. Qian, B. Chen, *Chem. Commun.* **2011**, *47*, 11715.
- [77] B. Bueken, H. Reinsch, N. Heidenreich, A. Vandekerkhove, F. Vermoortele, C. E. A. Kirschhock, N. Stock, D. de Vos, R. Ameloot, *CrystEngComm* **2017**, *19*, 4152.
- [78] M. Krüger, M. Albat, A. K. Inge, N. Stock, *CrystEngComm* **2017**, *19*, 4622.
- [79] J. Sha, X. Yang, L. Sun, X. Zhang, S. Li, J. Li, N. Sheng, *Polyhedron* **2017**, *127*, 396.
- [80] K. Benner, J. Ihringer, P. Klüfers, D. Marinov, *Angewandte Chemie (International ed. in English)* **2006**, *45*, 5818.
- [81] H. Lu, X. Yang, S. Li, Y. Zhang, J. Sha, C. Li, J. Sun, *Inorganic Chemistry Communications* **2015**, *61*, 48.
- [82] R. S. Forgan, R. A. Smaldone, J. J. Gassensmith, H. Furukawa, D. B. Cordes, Q. Li, C. E. Wilmer, Y. Y. Botros, R. Q. Snurr, A. M. Z. Slawin et al., *Journal of the American Chemical Society* **2012**, *134*, 406.
- [83] M. Ptak, B. Zarychta, D. Stefańska, A. Ciupa, W. Paraguassu, *Dalton Trans.* **2018**, *48*, 242.
- [84] W. Liang, R. Babarao, M. J. Murphy, D. M. D'Alessandro, *Dalton transactions (Cambridge, England : 2003)* **2015**, *44*, 1516.
- [85] H. Furukawa, F. Gándara, Y.-B. Zhang, J. Jiang, W. L. Queen, M. R. Hudson, O. M. Yaghi, *Journal of the American Chemical Society* **2014**, *136*, 4369.
- [86] J. M. Garcia Garfido, j. Enriquez, I. Chi-Duran, I. Jara, L. Vivas, F. J. Hernandez, F. Herrera, D. P. Singh, *Millimeter-Sized Metal-Organic Framework Single Crystals without Inversion Symmetry: Controlled Growth and Self-Assembly Mechanism*, **2020**.
- [87] Y. Liu, V. C. Kravtsov, R. Larsen, M. Eddaoudi, *Chemical communications (Cambridge, England)* **2006**, 1488.
- [88] R. Banerjee, A. Phan, B. Wang, C. Knobler, H. Furukawa, M. O'Keeffe, O. M. Yaghi, *Science* **2008**, *319*, 939.
- [89] Y.-R. Lee, M.-S. Jang, H.-Y. Cho, H.-J. Kwon, S. Kim, W.-S. Ahn, *Chemical Engineering Journal* **2015**, *271*, 276.
- [90] R. Banerjee, H. Furukawa, D. Britt, C. Knobler, M. O'Keeffe, O. M. Yaghi, *Journal of the American Chemical Society* **2009**, *131*, 3875.
- [91] W. Morris, C. J. Doonan, H. Furukawa, R. Banerjee, O. M. Yaghi, *Journal of the American Chemical Society* **2008**, *130*, 12626.
- [92] F. Wang, H.-R. Fu, Y. Kang, J. Zhang, *Chem. Commun.* **2014**, *50*, 12065.

- [93] A. Mohmeyer, *Synthesis, characterization and postsynthetic modification of a novel two-dimensional Zr-based metal-organic framework*, Hannover : Institutionelles Repositorium der Leibniz Universität Hannover, **2019**.
- [94] A. Mohmeyer, A. Schaate, B. Hoppe, H. A. Schulze, T. Heinemeyer, P. Behrens, *Chemical communications (Cambridge, England)* **2019**, *55*, 3367.
- [95] J. H. Cavka, S. Jakobsen, U. Olsbye, N. Guillou, C. Lamberti, S. Bordiga, K. P. Lillerud, *Journal of the American Chemical Society* **2008**, *130*, 13850.
- [96] V. Bon, I. Senkovska, M. S. Weiss, S. Kaskel, *CrystEngComm* **2013**, *15*, 9572.
- [97] L. Valenzano, B. Civalieri, S. Chavan, S. Bordiga, M. H. Nilsen, S. Jakobsen, K. P. Lillerud, C. Lamberti, *Chem. Mater.* **2011**, *23*, 1700.
- [98] Q. Yang, A. D. Wiersum, H. Jobic, V. Guillerm, C. Serre, P. L. Llewellyn, G. Maurin, *J. Phys. Chem. C* **2011**, *115*, 13768.
- [99] F. Luo, C. Yan, L. Dang, R. Krishna, W. Zhou, H. Wu, X. Dong, Y. Han, T.-L. Hu, M. O'Keeffe et al., *Journal of the American Chemical Society* **2016**, *138*, 5678.
- [100] H. Hayashi, A. P. Côté, H. Furukawa, M. O'Keeffe, O. M. Yaghi, *Nature materials* **2007**, *6*, 501.
- [101] A. Phan, C. J. Doonan, F. J. Uribe-Romo, C. B. Knobler, M. O'Keeffe, O. M. Yaghi, *Accounts of chemical research* **2010**, *43*, 58.
- [102] W. Morris, C. J. Stevens, R. E. Taylor, C. Dybowski, O. M. Yaghi, M. A. Garcia-Garibay, *J. Phys. Chem. C* **2012**, *116*, 13307.
- [103] Y. Liu, E. Hu, E. A. Khan, Z. Lai, *Journal of Membrane Science* **2010**, *353*, 36.
- [104] R. E. Cohen, *Nature* **1992**, *358*, 136.
- [105] D. D. Fong, G. B. Stephenson, S. K. Streiffer, J. A. Eastman, O. Auciello, P. H. Fuoss, C. Thompson, *Science* **2004**, *304*, 1650.
- [106] L. Balcells, J. Fontcuberta, B. Martínez, X. Obradors, *Physical review. B, Condensed matter* **1998**, *58*, R14697-R14700.
- [107] Hwang, Palstra, Cheong, Batlogg, *Physical review. B, Condensed matter* **1995**, *52*, 15046.
- [108] J. G. Bednorz, K. A. Müller, *Rev. Mod. Phys.* **1988**, *60*, 585.
- [109] T. He, Q. Huang, A. P. Ramirez, Y. Wang, K. A. Regan, N. Rogado, M. A. Hayward, M. K. Haas, J. S. Slusky, K. Inumara et al., *Nature* **2001**, *411*, 54.
- [110] a) A. Pisanu, A. Mahata, E. Mosconi, M. Patrini, P. Quadrelli, C. Milanese, F. de Angelis, L. Malavasi, *ACS Energy Lett.* **2018**, *3*, 1353; b) Y. Shi, Y. Zhou, Z. Ma, G. Xiao, K. Wang, B. Zou, *J. Mater. Chem. C* **2020**, *8*, 12755.
- [111] a) W. Fu, H. Chen, A.-Y. Jen, *Materials Today Nano* **2021**, *14*, 100117; b) F. Zhang, H. Lu, J. Tong, J. J. Berry, M. C. Beard, K. Zhu, *Energy Environ. Sci.* **2020**, *13*, 1154.
- [112] a) T. Qiu, Y. Hu, F. Xu, Z. Yan, F. Bai, G. Jia, S. Zhang, *Nanoscale* **2018**, *10*, 20963; b) P. M. Rørvik, T. Grande, M.-A. Einarsrud, *Adv. Mater.* **2011**, *23*, 4007.
- [113] J. Almutlaq, J. Yin, O. F. Mohammed, O. M. Bakr, *The journal of physical chemistry letters* **2018**, *9*, 4131.

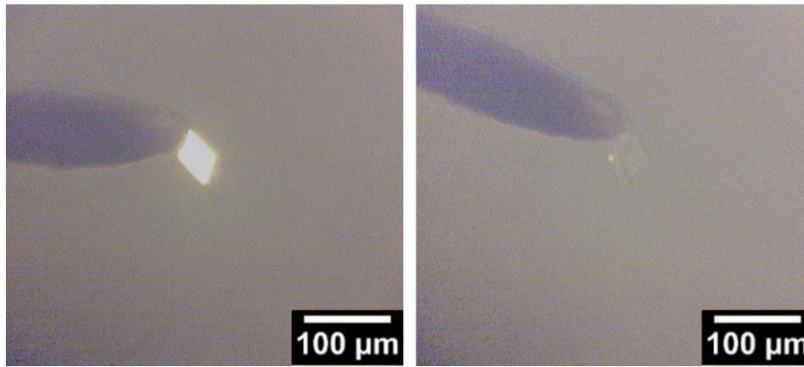
- [114] Y. Zhang, M. I. Saidaminov, I. Dursun, H. Yang, B. Murali, E. Alarousu, E. Yengel, B. A. Alshankiti, O. M. Bakr, O. F. Mohammed, *The journal of physical chemistry letters* **2017**, *8*, 961.
- [115] L. N. Quan, B. P. Rand, R. H. Friend, S. G. Mhaisalkar, T.-W. Lee, E. H. Sargent, *Chemical reviews* **2019**, *119*, 7444.
- [116] A. F. Holleman, N. Wiberg, E. Wiberg, *Lehrbuch der anorganischen Chemie*, De Gruyter, Berlin, **2007**.
- [117] U. Müller, *Anorganische Strukturchemie*, Vieweg + Teubner, Wiesbaden, **2009**.
- [118] L. Rao, X. Ding, X. Du, G. Liang, Y. Tang, K. Tang, J. Z. Zhang, *Beilstein J. Nanotechnol.* **2019**, *10*, 666.
- [119] X.-K. Liu, W. Xu, S. Bai, Y. Jin, J. Wang, R. H. Friend, F. Gao, *Nature materials* **2021**, *20*, 10.
- [120] Y. Liu, Z. Yu, S. Chen, J. H. Park, E. D. Jung, S. Lee, K. Kang, S.-J. Ko, J. Lim, M. H. Song et al., *Nano Energy* **2021**, *80*, 105511.
- [121] S. A. Veldhuis, P. P. Boix, N. Yantara, M. Li, T. C. Sum, N. Mathews, S. G. Mhaisalkar, *Adv. Mater.* **2016**, *28*, 6804.
- [122] Q. Ma, S. Huang, S. Chen, M. Zhang, C. F. J. Lau, M. N. Lockrey, H. K. Mulmudi, Y. Shan, J. Yao, J. Zheng et al., *J. Phys. Chem. C* **2017**, *121*, 19642.
- [123] C. Liu, Q. Zeng, B. Yang, *Adv. Mater. Interfaces* **2019**, *6*, 1901136.
- [124] X. Sheng, Y. Liu, Y. Wang, Y. Li, X. Wang, X. Wang, Z. Dai, J. Bao, X. Xu, *Adv. Mater.* **2017**, *29*, 1700150.
- [125] Q. Chen, J. Wu, X. Ou, B. Huang, J. Almutlaq, A. A. Zhumekenov, X. Guan, S. Han, L. Liang, Z. Yi et al., *Nature* **2018**, *561*, 88.
- [126] S. A. Kulkarni, S. G. Mhaisalkar, N. Mathews, P. P. Boix, *Small Methods* **2019**, *3*, 1800231.
- [127] X. Li, F. Cao, D. Yu, J. Chen, Z. Sun, Y. Shen, Y. Zhu, L. Wang, Y. Wei, Y. Wu et al., *Small (Weinheim an der Bergstrasse, Germany)* **2017**, *13*.
- [128] A. Swarnkar, R. Chulliyil, V. K. Ravi, M. Irfanullah, A. Chowdhury, A. Nag, *Angewandte Chemie (International ed. in English)* **2015**, *54*, 15424.
- [129] D. N. Dirin, L. Protesescu, D. Trummer, I. V. Kochetygov, S. Yakunin, F. Krumeich, N. P. Stadie, M. V. Kovalenko, *Nano letters* **2016**, *16*, 5866.
- [130] Z. Li, L. Kong, S. Huang, L. Li, *Angew. Chem.* **2017**, *129*, 8246.
- [131] A. Loiudice, M. Strach, S. Saris, D. Chernyshov, R. Buonsanti, *Journal of the American Chemical Society* **2019**, *141*, 8254.
- [132] C. Sun, Y. Zhang, C. Ruan, C. Yin, X. Wang, Y. Wang, W. W. Yu, *Adv. Mater.* **2016**, *28*, 10088.
- [133] J.-Y. Sun, F. T. Rabouw, X.-F. Yang, X.-Y. Huang, X.-P. Jing, S. Ye, Q.-Y. Zhang, *Adv. Funct. Mater.* **2017**, *27*, 1704371.
- [134] H.-C. Wang, S.-Y. Lin, A.-C. Tang, B. P. Singh, H.-C. Tong, C.-Y. Chen, Y.-C. Lee, T.-L. Tsai, R.-S. Liu, *Angew. Chem.* **2016**, *128*, 8056.

- [135] Y. Wei, X. Deng, Z. Xie, X. Cai, S. Liang, P. Ma, Z. Hou, Z. Cheng, J. Lin, *Adv. Funct. Mater.* **2017**, *27*, 1703535.
- [136] J. Aguilera-Sigalat, D. Bradshaw, *Coordination Chemistry Reviews* **2016**, *307*, 267.
- [137] L. Chen, R. Luque, Y. Li, *Chemical Society reviews* **2017**, *46*, 4614.
- [138] X. Lin, G. Gao, L. Zheng, Y. Chi, G. Chen, *Analytical chemistry* **2014**, *86*, 1223.
- [139] G. Lu, S. Li, Z. Guo, O. K. Farha, B. G. Hauser, X. Qi, Y. Wang, X. Wang, S. Han, X. Liu et al., *Nature chemistry* **2012**, *4*, 310.
- [140] C. Rösler, R. A. Fischer, *CrystEngComm* **2015**, *17*, 199.
- [141] C.-Y. Sun, X.-L. Wang, X. Zhang, C. Qin, P. Li, Z.-M. Su, D.-X. Zhu, G.-G. Shan, K.-Z. Shao, H. Wu et al., *Nature communications* **2013**, *4*, 2717.
- [142] J. Yu, C. Mu, B. Yan, X. Qin, C. Shen, H. Xue, H. Pang, *Mater. Horiz.* **2017**, *4*, 557.
- [143] L. Shi, J. Wang, L. Zhou, Y. Chen, J. Yan, C. Dai, *Journal of Solid State Chemistry* **2020**, *282*, 121062.
- [144] C. Zhang, B. Wang, W. Li, S. Huang, L. Kong, Z. Li, L. Li, *Nature communications* **2017**, *8*, 1138.
- [145] D. Zhang, W. Zhou, Q. Liu, Z. Xia, *ACS applied materials & interfaces* **2018**, *10*, 27875.
- [146] L.-Y. Wu, Y.-F. Mu, X.-X. Guo, W. Zhang, Z.-M. Zhang, M. Zhang, T.-B. Lu, *Angew. Chem.* **2019**, *131*, 9591.
- [147] Z.-C. Kong, J.-F. Liao, Y.-J. Dong, Y.-F. Xu, H.-Y. Chen, D.-B. Kuang, C.-Y. Su, *ACS Energy Lett.* **2018**, *3*, 2656.
- [148] a) S. Mollick, T. N. Mandal, A. Jana, S. Fajal, A. V. Desai, S. K. Ghosh, *ACS Appl. Nano Mater.* **2019**, *2*, 1333; b) Y.-F. Xu, M.-Z. Yang, B.-X. Chen, X.-D. Wang, H.-Y. Chen, D.-B. Kuang, C.-Y. Su, *Journal of the American Chemical Society* **2017**, *139*, 5660; c) L. Zhou, Y.-F. Xu, B.-X. Chen, D.-B. Kuang, C.-Y. Su, *Small (Weinheim an der Bergstrasse, Germany)* **2018**, *14*, e1703762.
- [149] D. Zhang, Y. Xu, Q. Liu, Z. Xia, *Inorganic chemistry* **2018**, *57*, 4613.
- [150] J. Liu, Y. Zhao, X. Li, J. Wu, Y. Han, X. Zhang, Y. Xu, *Crystal Growth & Design* **2020**, *20*, 454.
- [151] Y. Cui, R. Song, J. Yu, M. Liu, Z. Wang, C. Wu, Y. Yang, Z. Wang, B. Chen, G. Qian, *Adv. Mater.* **2015**, *27*, 1420.
- [152] Y. Cui, H. Xu, Y. Yue, Z. Guo, J. Yu, Z. Chen, J. Gao, Y. Yang, G. Qian, B. Chen, *Journal of the American Chemical Society* **2012**, *134*, 3979.
- [153] J. Rocha, C. D. S. Brites, L. D. Carlos, *Chemistry – A European Journal* **2016**, *22*, 14782.
- [154] F. Vetrone, R. Naccache, A. Zamarrón, A. La Juarranz de Fuente, F. Sanz-Rodríguez, L. Martínez Maestro, E. Martín Rodríguez, D. Jaque, J. García Solé, J. A. Capobianco, *ACS nano* **2010**, *4*, 3254.
- [155] S. Yakunin, B. M. Benin, Y. Shynkarenko, O. Nazarenko, M. I. Bodnarchuk, D. N. Dirin, C. Hofer, S. Cattaneo, M. V. Kovalenko, *Nature materials* **2019**, *18*, 846.
- [156] S. Zhou, K. Deng, X. Wei, G. Jiang, C. Duan, Y. Chen, M. Yin, *Optics Communications* **2013**, *291*, 138.

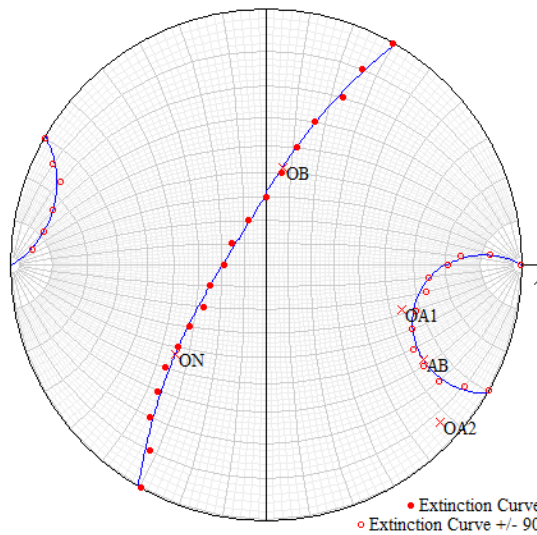
- [157] C. Zhang, W. Li, L. Li, *Angew. Chem.* **2021**, *133*, 7564.
- [158] J. Ren, T. Li, X. Zhou, X. Dong, A. V. Shorokhov, M. B. Semenov, V. D. Krevchik, Y. Wang, *Chemical Engineering Journal* **2019**, *358*, 30.
- [159] S. Bhattacharyya, D. Rambabu, T. K. Maji, *J. Mater. Chem. A* **2019**, *7*, 21106.
- [160] D. Zhang, J. Zhao, Q. Liu, Z. Xia, *Inorganic chemistry* **2019**, *58*, 1690.
- [161] J.-H. Cha, K. Noh, W. Yin, Y. Lee, Y. Park, T. K. Ahn, A. Mayoral, J. Kim, D.-Y. Jung, O. Terasaki, *The journal of physical chemistry letters* **2019**, *10*, 2270.
- [162] Z. Chen, Z.-G. Gu, W.-Q. Fu, F. Wang, J. Zhang, *ACS applied materials & interfaces* **2016**, *8*, 28737.
- [163] H. He, Y. Cui, B. Li, B. Wang, C. Jin, J. Yu, L. Yao, Y. Yang, B. Chen, G. Qian, *Advanced materials (Deerfield Beach, Fla.)* **2019**, *31*, e1806897.
- [164] H. Tsai, S. Shrestha, R. A. Vilá, W. Huang, C. Liu, C.-H. Hou, H.-H. Huang, X. Wen, M. Li, G. Wiederrecht et al., *Nat. Photonics* **2021**, *15*, 843.
- [165] C. Ardila-Suárez, D. R. Molina V, H. Alem, V. G. Baldovino-Medrano, G. E. Ramírez-Caballero, *Physical chemistry chemical physics : PCCP* **2020**, *22*, 12591.
- [166] D. Feng, Z.-Y. Gu, J.-R. Li, H.-L. Jiang, Z. Wei, H.-C. Zhou, *Angew. Chem.* **2012**, *124*, 10453.
- [167] J. Ma, A. P. Kalenak, A. G. Wong-Foy, A. J. Matzger, *Angew. Chem.* **2017**, *129*, 14810.
- [168] C. Zhang, B. Wang, W. Zheng, S. Huang, L. Kong, Z. Li, G. He, L. Li, *Nano Energy* **2018**, *51*, 358.
- [169] J. W. Oh, H. Han, H. H. Kim, H. Lee, D. Kim, J. Lee, J. Kim, W. K. Choi, C. Park, *Advanced Functional Materials* **2022**, *32*, 2111894.
- [170] J. Hou, P. Chen, A. Shukla, A. Krajnc, T. Wang, X. Li, R. Doasa, L. H. G. Tizei, B. Chan, D. N. Johnstone et al., *Science* **2021**, *374*, 621.
- [171] L. E. Kreno, K. Leong, O. K. Farha, M. Allendorf, R. P. van Duyne, J. T. Hupp, *Chemical reviews* **2012**, *112*, 1105.
- [172] J.-R. Li, R. J. Kuppler, H.-C. Zhou, *Chem. Soc. Rev.* **2009**, *38*, 1477.
- [173] a) Y. Liu, Z. U. Wang, H.-C. Zhou, *Greenhouse Gas Sci Technol* **2012**, *2*, 239; b) S. R. Miller, D. Heurtaux, T. Baati, P. Horcajada, J.-M. Grenèche, C. Serre, *Chemical communications (Cambridge, England)* **2010**, *46*, 4526.
- [174] a) F.-Y. Yi, D. Chen, M.-K. Wu, L. Han, H.-L. Jiang, *ChemPlusChem* **2016**, *81*, 675; b) H. Tan, F. Che, M. Wei, Y. Zhao, M. I. Saidaminov, P. Todorović, D. Broberg, G. Walters, F. Tan, T. Zhuang et al., *Nature communications* **2018**, *9*, 3100.
- [175] L. L. da Luz, R. Milani, J. F. Felix, I. R. B. Ribeiro, M. Talhavini, B. A. D. Neto, J. Chojnacki, M. O. Rodrigues, S. A. Júnior, *ACS applied materials & interfaces* **2015**, *7*, 27115.
- [176] H. Zhang, X. Shan, Z. Ma, L. Zhou, M. Zhang, P. Lin, S. Hu, E. Ma, R. Li, S. Du, *J. Mater. Chem. C* **2014**, *2*, 1367.
- [177] a) V. BOLDYREV, *Solid State Ionics* **1993**, *63-65*, 537; b) D. E. Crawford, J. Casaban, *Advanced materials (Deerfield Beach, Fla.)* **2016**, *28*, 5747.

- [178] *Kristallstrukturbestimmung*, **2007**.
- [179] K. P. C. Vollhardt, N. E. Schore, H. Butenschön, K.-M. Roy (Eds.) *Organische Chemie*, Wiley-VCH, Weinheim, **2011**.
- [180] K. Niederauer, W. Schäfer, *Phys. Unserer Zeit* **1985**, *16*, 180.
- [181] H. Wu, L. Yao, W. Cao, Y. Yang, Y. Cui, D. Yang, G. Qian, *J. Mater. Chem. C* **2022**, *10*, 5550.
- [182] S. B. Peh, Y. Cheng, J. Zhang, Y. Wang, G. H. Chan, J. Wang, D. Zhao, *Dalton Trans.* **2019**, *48*, 7069.
- [183] C.-Y. Sun, X.-X. Li, S.-F. Wang, W.-J. Li, X.-J. Zheng, *Z. anorg. allg. Chem.* **2008**, *634*, 950.
- [184] R. Hardian, S. Dissegna, A. Ullrich, P. L. Llewellyn, M.-V. Coulet, R. A. Fischer, *Chemistry – A European Journal* **2021**, *27*, 6804.
- [185] Emil Agocs, *Report v1.1. MOF single crystal ellipsometry measurements*, **2021**.
- [186] S. S. Batsanov, *Refractometry and chemical structure. Authorized transl. from the Russ. by Paul Porter Sutton*, Consultants Bureau, New York, **1961**.
- [187] a) S. Eslava, L. Zhang, S. Esconjauregui, J. Yang, K. Vanstreels, M. R. Baklanov, E. Saiz, *Chem. Mater.* **2013**, *25*, 27; b) F. Tian, A. M. Cerro, A. M. Mosier, H. K. Wayment-Steele, R. S. Shine, A. Park, E. R. Webster, L. E. Johnson, M. S. Johal, L. Benz, *J. Phys. Chem. C* **2014**, *118*, 14449.
- [188] T. C. Nader Amin, University of Oxford, Oxford, **2017**.
- [189] H. Zhao, R. Sun, Z. Wang, K. Fu, X. Hu, Y. Zhang, *Advanced Functional Materials* **2019**, *29*, 1902262.
- [190] V. K. Ravi, A. Swarnkar, R. Chakraborty, A. Nag, *Nanotechnology* **2016**, *27*, 325708.
- [191] Z. Shi, X. Li, C. Shan in *Quantum-dot Based Light-emitting Diodes* (Ed.: M. S. Ghamsari), IntechOpen, Erscheinungsort nicht ermittelbar, **2017**.
- [192] J. Feng, X. Han, H. Huang, Q. Meng, Z. Zhu, T. Yu, Z. Li, Z. Zou, *Science Bulletin* **2020**, *65*, 726.
- [193] H. L. Clever, F. J. Johnston, *Journal of Physical and Chemical Reference Data* **1980**, *9*, 751.
- [194] Xiaomei Chen, Feng Zhang, Yong Ge, Lifu Shi, Sheng Huang, Jialun Tang, Zhao Lv, Li Zhang, Bingsuo Zou, Haizheng Zhong, *Advanced Functional Materials* **2018**, *28*, 1706567.
- [195] F. Chen, M. Imran, L. Pasquale, M. Salerno, M. Prato, *Materials Research Bulletin* **2021**, *134*, 111107.
- [196] D. Di Girolamo, M. I. Dar, D. Dini, L. Gontrani, R. Caminiti, A. Mattoni, M. Graetzel, S. Meloni, *J. Mater. Chem. A* **2019**, *7*, 12292.
- [197] Y. Wei, Z. Cheng, J. Lin, *Chemical Society reviews* **2019**, *48*, 310.
- [198] W. Lv, L. Li, M. Xu, J. Hong, X. Tang, L. Xu, Y. Wu, R. Zhu, R. Chen, W. Huang, *Adv. Mater.* **2019**, *31*, e1900682.
- [199] Z. Wei, Z.-Y. Gu, R. K. Arvapally, Y.-P. Chen, R. N. McDougald, J. F. Ivy, A. A. Yakovenko, D. Feng, M. A. Omary, H.-C. Zhou, *Journal of the American Chemical Society* **2014**, *136*, 8269.

8 Appendix

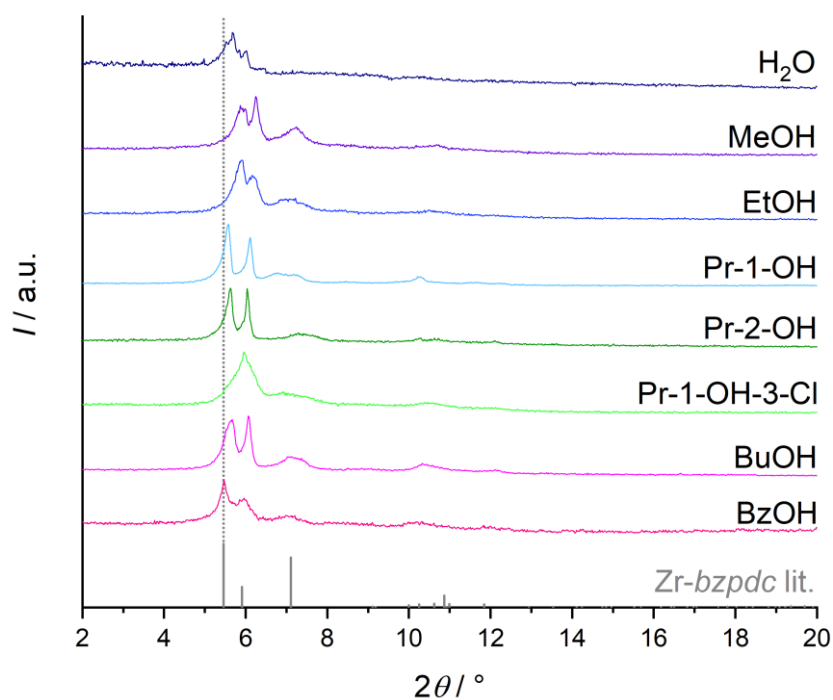


Appendix Figure 1: View during the determination of the extinction curve; Left: View during measurement, Right: Point of extinction.



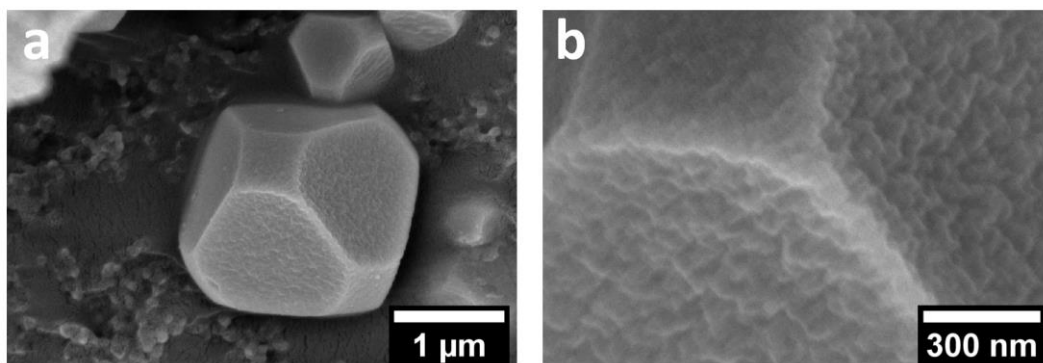
Appendix Figure 2: Graphical output plotted by excalibrw, obtained from the extinction data of a MOF single crystal (AB = acute bisectrix, OB = obtuse bisectrix, ON = optical normal, OA1 & OA2 = optical axes 1 and 2).

8.1 Powder X-ray diffraction spectra



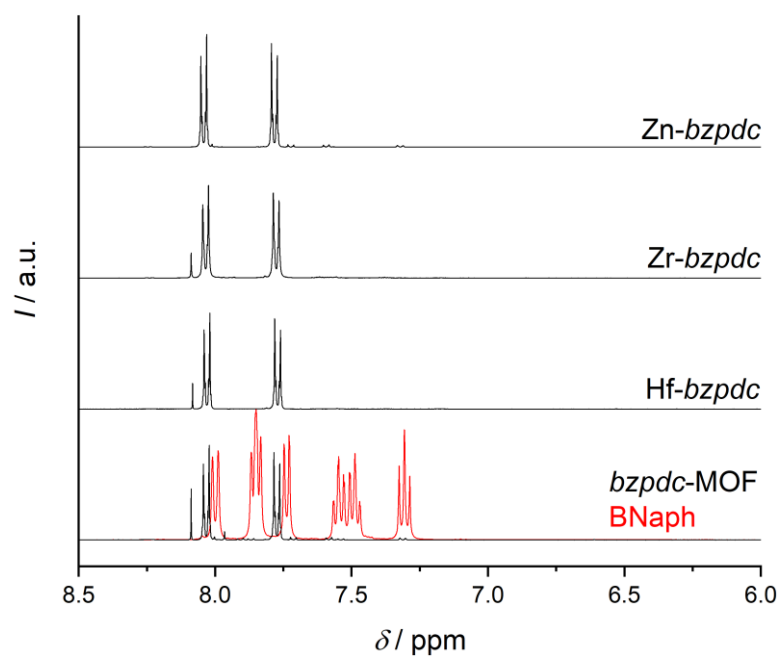
Appendix Figure 3: Diffractograms of post-synthetically modified Zr-*bzpdC* single crystals (the modification reagents are displayed within the diagram).

8.2 Scanning electron microscopy images

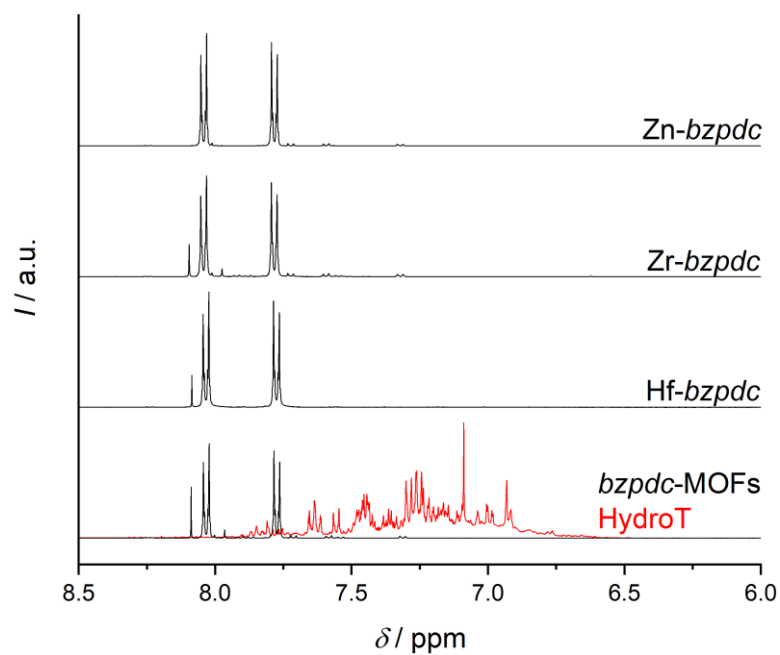


Appendix Figure 4: SEM images of the Ce(IV)-*bdC*-MOF with different magnifications.

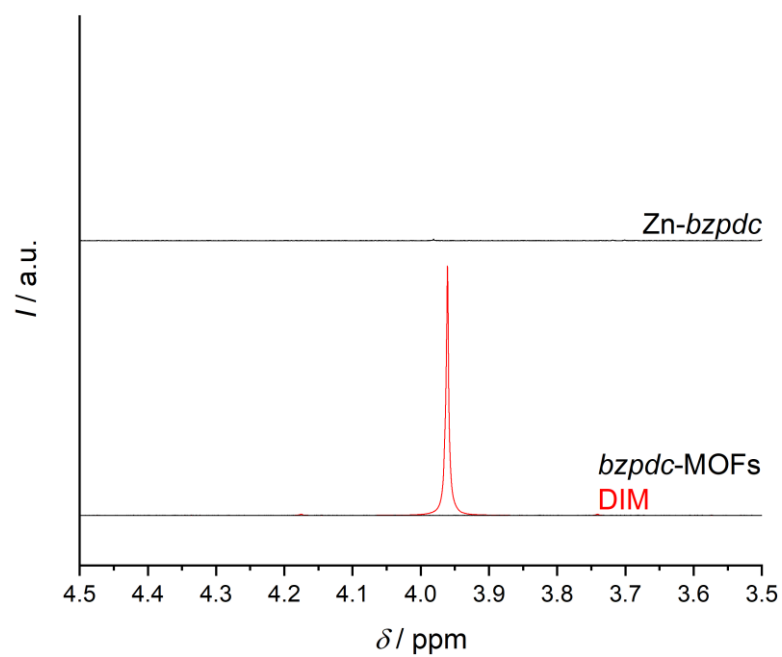
8.3 $^1\text{H-NMR}$ measurements



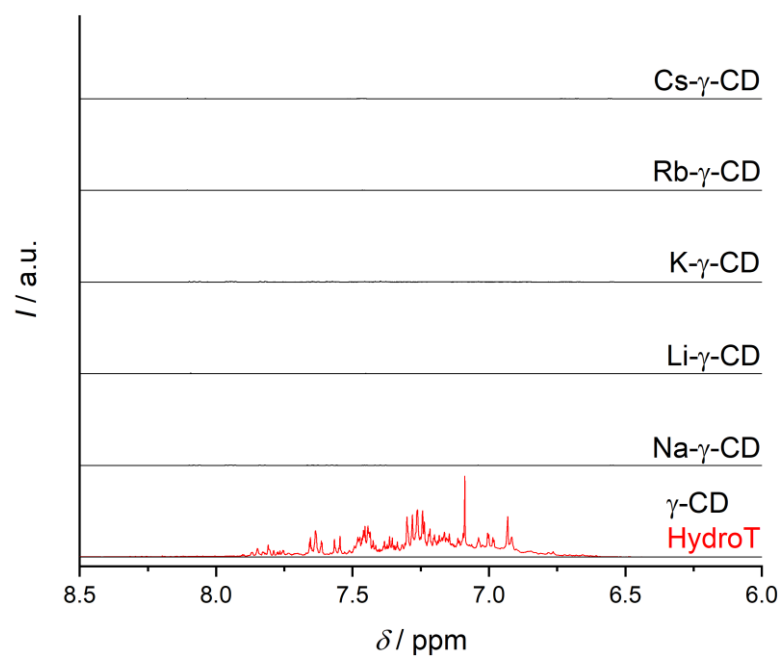
Appendix Figure 5: $^1\text{H-NMR}$ 1-bromonaphthalene measurements for *bzpdC*-MOF single crystals.



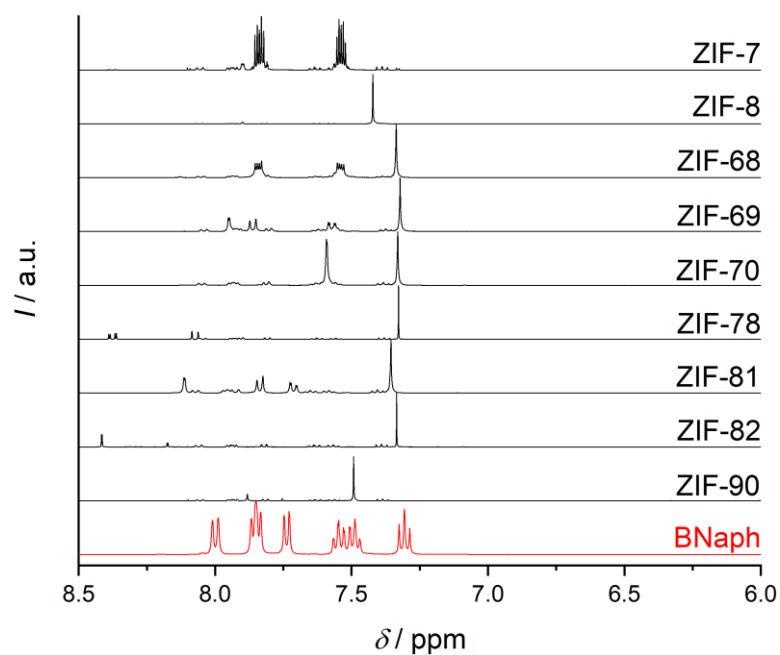
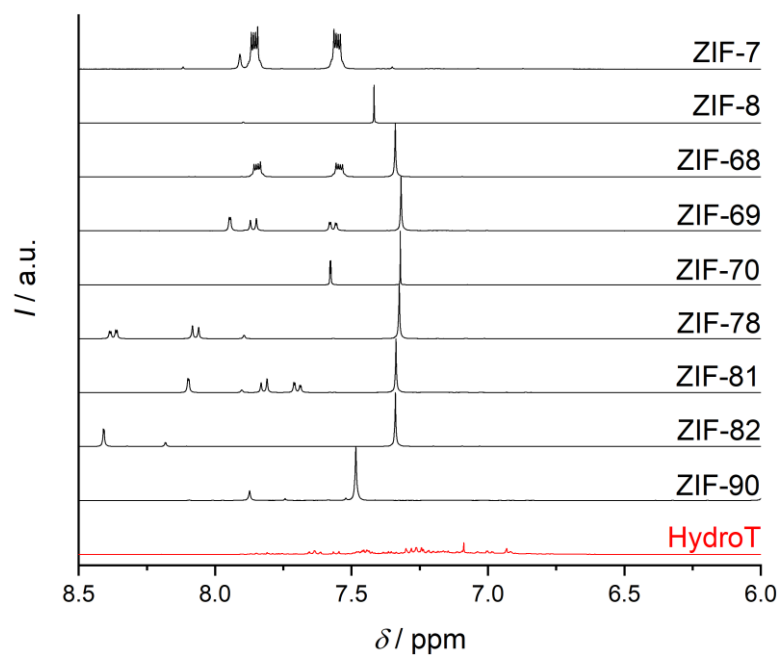
Appendix Figure 6: $^1\text{H-NMR}$ hydrogenated terphenyl measurements for *bzpdC*-MOF crystals.

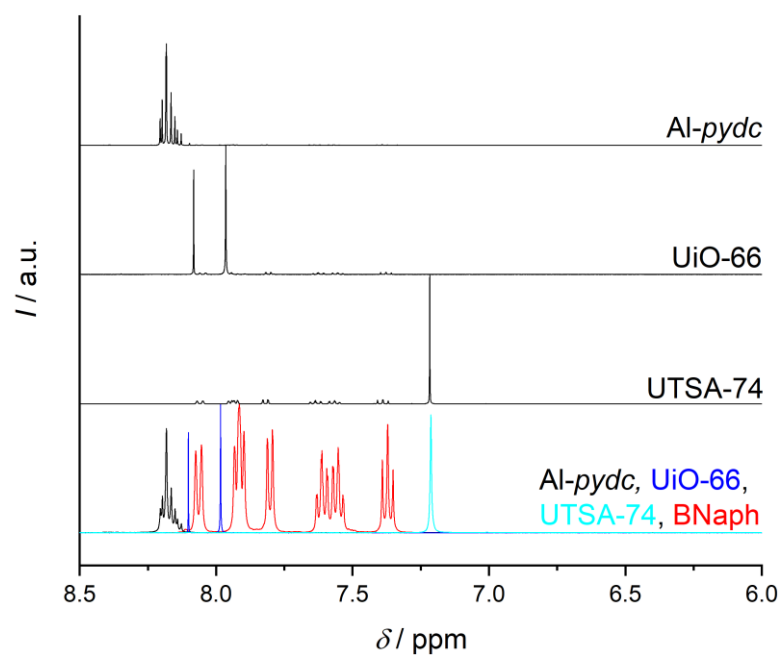


Appendix Figure 7: $^1\text{H-NMR}$ diiodomethane measurement for *Zn-bzpdC* MOF single crystals.

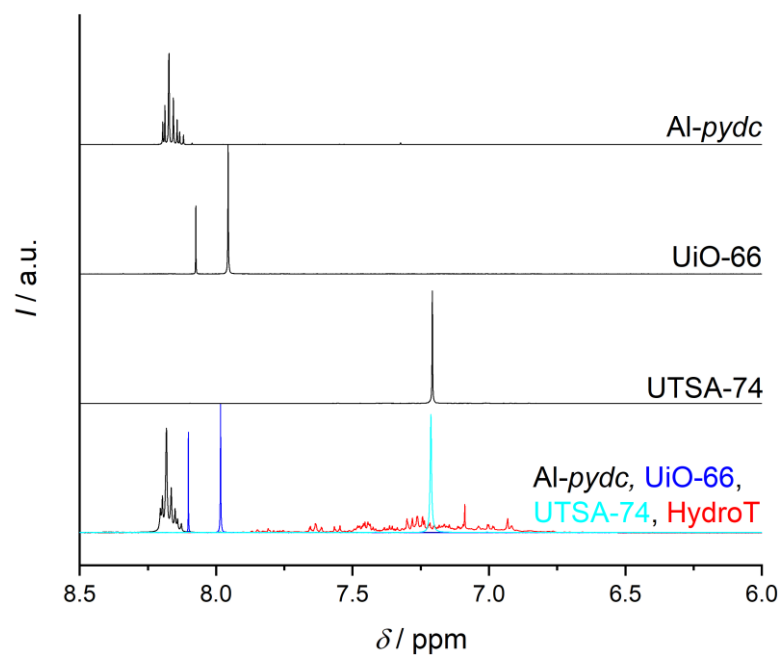


Appendix Figure 8: $^1\text{H-NMR}$ hydrogenated terphenyl measurements for $\gamma\text{-CD}$ single crystals.

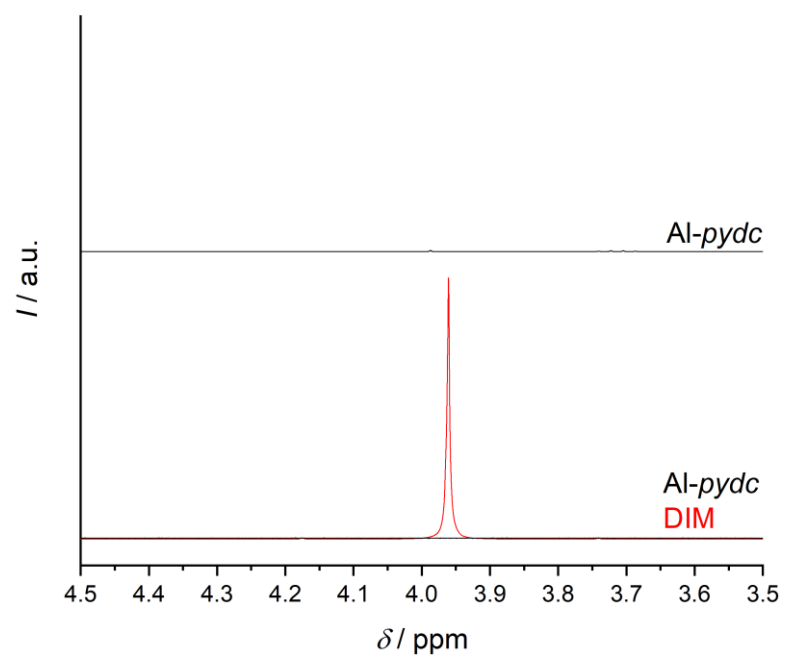
Appendix Figure 9: $^1\text{H-NMR}$ 1-bromonaphthalene measurement for ZIF single crystals.Appendix Figure 10: $^1\text{H-NMR}$ hydrogenated terphenyl measurement for ZIF single crystals.



Appendix Figure 11: $^1\text{H-NMR}$ 1-bromonaphthalene measurement for different MOF single crystals.



Appendix Figure 12: $^1\text{H-NMR}$ hydrogenated terphenyl measurement for different MOF single crystals.



Appendix Figure 13: $^1\text{H-NMR}$ diiodomethane measurement for Al-*pydc* MOF single crystals.

8.4 Ellipsometry Measurements^[185]

Results:

Table. Optical properties of grains at 589 nm and the measured square errors(MSE) using Cauchy based model and BSpline based model:

Sample	Cauchy based model		BSpline based model	
	RI (refractive index)	MSE	RI	MSE
RbY (S1)	1,48603	25	1,48626	25
RbY (S3b)	1,49959	27	1,49910	27
NaY (S4)	1,48380	11,4	1,48393	11,3
NaY (S5)	1,48405	23	1,48365	23
CsY (S6)	1,51154	25	1,51461	24

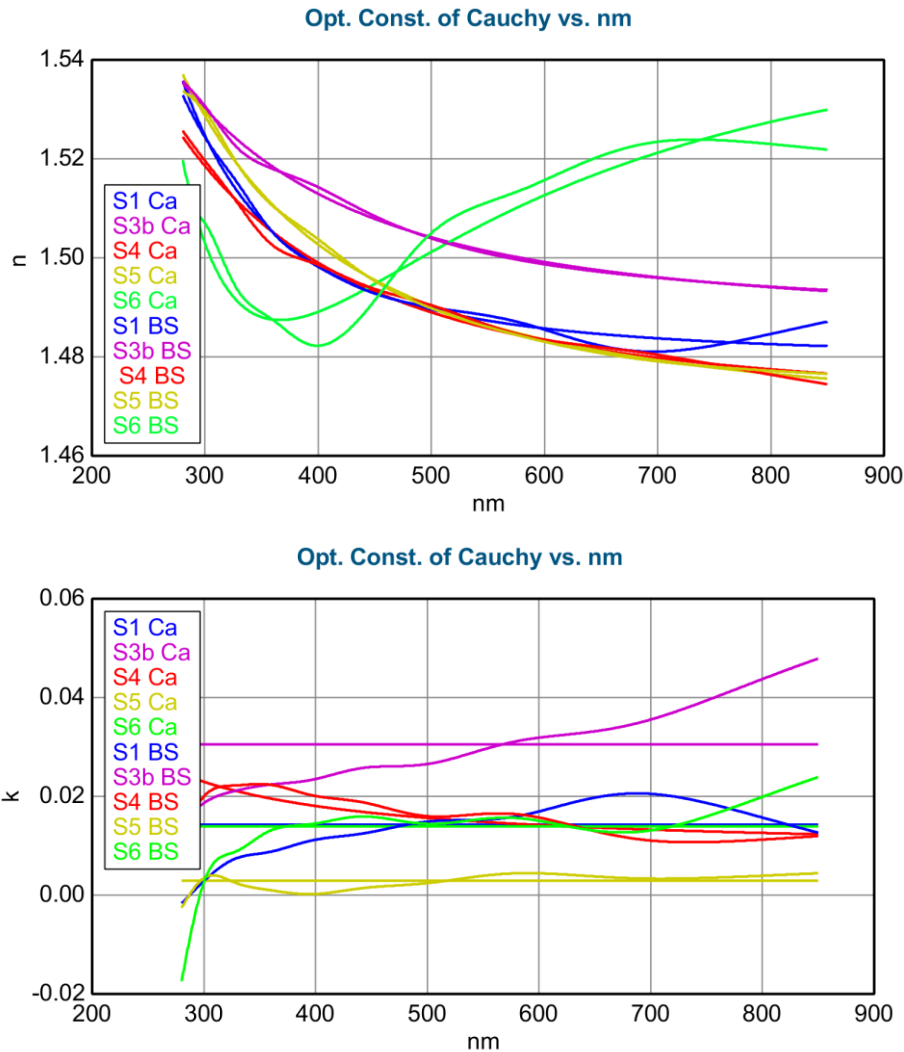


Fig.: Refractive index (left) and extinction coefficient(right) of grains depend on wavelength (Ca- from Cauchy model; SB- BSpline model)

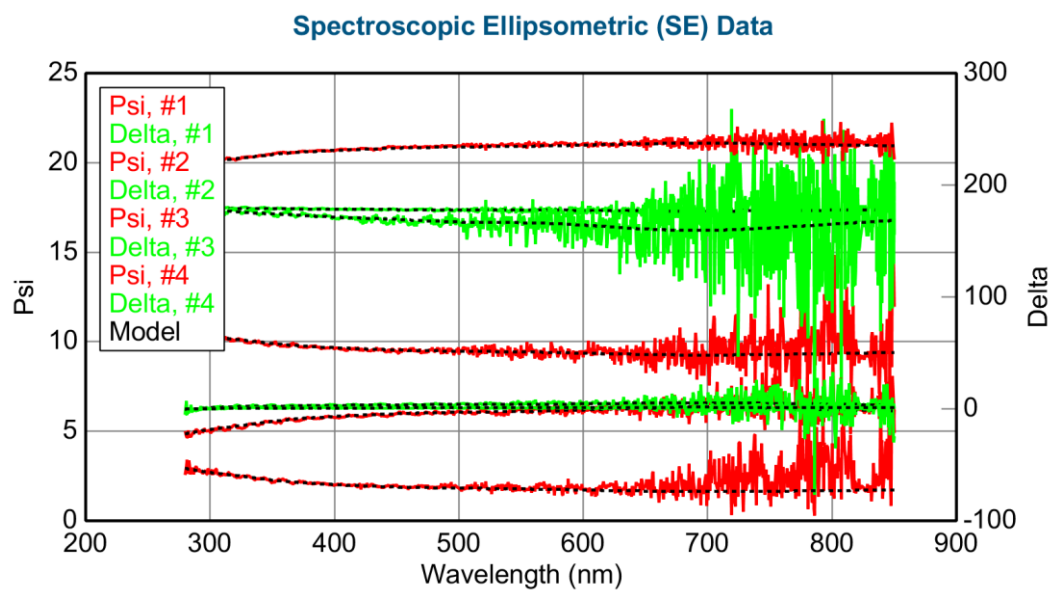
Optical model:

Substrate = Cauchy A = 1.479 (fit) B = 0.00166 (fit) C = 0.00021713 (fit) k Amplitude = 0.01428 (fit) Exponent = 0.00 (fit) Band Edge = 400.0 nm	Substrate = B-Spline Init. values: n = 1.500 k = 0.00 Starting Mat = RbY_s1_nk Resolution (eV) = 0.300 10 Pts. (1.459-4.427 eV) Draw Node Graph Fit Opt. Const. = ON Use KK Mode = OFF Query remote system for Opt. Const. = OFF Show Advanced Options = OFF
$n(\lambda) = A + \frac{B}{\lambda^2} + \frac{C}{\lambda^4}$ $k = kamp \cdot e^{\exp(E - \text{Bandedge})}$ <p>Cauchy model</p>	<p>BSpline model</p>

In case of BSpline mode the optical properties of grains were described using B-Spline function with 0.3 eV resolution. The KK Mode and the E2 force to be positive were OFF.

Spectra:

Typical measured spectra and fitted spectra



9 Curriculum Vitae

Name	Anna-Lena Erika Renate Deutsch
Date of birth	27 th December 1995
Place of birth	Landshut
Nationality	German
02/2022–07/2022	Visiting Ph.D. Student at the department of Materials Science and Engineering, Seoul National University, Seoul, Korea (Advisor: Prof. Tae-Woo Lee) Research: Perovskites and Metal-organic frameworks for LEDs
Since 11/2019	Ph.D. Student at the department of Inorganic Chemistry, Gottfried-Wilhelm Leibniz University, Hanover, Germany (Advisor: Prof. Peter Behrens) Member of PhoenixD (Cluster of Excellence) Research: Metal-organic frameworks and their Refractive Index
09/2018–12/2018	Exchange Student at the department of Chemistry and Materials Science, Aalto University, Espoo, Finland (Advisor: Prof. Tanja Kallio) Research: Bifunctional oxygen electrocatalysts
10/2017–09/2019	M.S. Student Course of study in chemistry – M.S., Gottfried-Wilhelm Leibniz University, Hanover, Germany (Thesis Advisor: Prof. Peter Behrens)
10/2014–09/2017	B.S. Student Course of study in chemistry – B.S., Gottfried-Wilhelm Leibniz University, Hanover, Germany (Thesis Advisor: Prof. Peter Behrens)
06/2014	Abitur (A-Levels) at the Matthias-Claudius Gymnasium in Gehrden

10 List of Publications

Articles

Title: 'Application and Analysis of a Salt Bridge Reference Electrode Setup for PEM Water Electrolysis: Towards an Extended Voltage Loss Break Down'

L. V. Böhre, S. Bullerdiek, P. Trinke, B. Bensmann, A.-L. E. R. Deutsch, P. Behrens, R. Hanke-Rauschenbach, *J. Electrochem. Soc.* **2022**, *169*, 124513.

Poster presentations

2nd Retreat of the Cluster of Excellence PhoenixD (Photonics, Optics, Engineering – Innovation Across Disciplines), Schneverdingen, Germany, September 2020

'Syntheses and refractive index measurements of MOF single crystals'

A.-L. E. R. Deutsch, T. Heinemeyer, R. X. Fischer, P. Behrens

3rd Retreat of the Cluster of Excellence PhoenixD, Schneverdingen, Germany, September 2021

'Syntheses and refractive index measurements of MOF single crystals'

A.-L. E. R. Deutsch, R. X. Fischer, P. Behrens

4th European Conference on Metal Organic Frameworks and Porous Polymers, online, September 2021

'Refractive index measurements of MOF single crystals using the immersion method'

A.-L. E. R. Deutsch, T. Heinemeyer, R. X. Fischer, P. Behrens

8th International Conference on Metal-Organic Frameworks and Open Framework Compounds, Dresden, Germany, September 2022

'Syntheses and refractive index measurements of MOF single crystals'

A.-L. E. R. Deutsch, E. Agócs, R. X. Fischer, P. Behrens